Report for the Arbuckle-Simpson Hydrology Study:

Electrical Resistivity Imaging of the Arbuckle-Simpson Aquifer

OKLAHOMA STATE UNIVERSITY
Boone Pickens School of Geology
105 Noble Research Center
Stillwater, OK 74078-3031
405.744.6358, FAX 405.744.7841

Electrical Resistivity Imaging of the Arbuckle-Simpson Aquifer

FINAL REPORT

by:

Todd Halihan
Jim Puckette
Michael Sample
and Mathew Riley

Oklahoma State University
Boone Pickens School of Geology
105 Noble Research Center
Stillwater, Oklahoma 74078

October 7, 2009
Stillwater, Oklahoma

Submitted to:

Oklahoma Water Resources Board
3800 North Classen Blvd.
Oklahoma City, OK 73118

Cover: ERI line deployed for data collection at the Arbuckle-Simpson Ranch site

Table of Contents

List of Figures

List of Tables

1.0 Executive Summary

Electrical Resistivity Imaging (ERI) has been made possible by advancements in both instrumentation and software developed over the past 15 years. Electrical resistivity is one of the oldest methods utilized by geophysicists, but ERI is a modification made possible by advanced in equipment and software. ERI surveys rapidly collect thousands of measurements to allow for use as a subsurface imaging tool. This tool is similar to seismic surveys for the oil industry in allowing an “electrical picture” of the subsurface.

The work progressed to evaluate four major objectives for ERI data in the Arbuckle-Simpson aquifer. First, the background properties of the major lithologies were assessed using quarries and outcrops. Second, the properties of the epikarst zone of the aquifer were evaluated. Third, the fault orientations in the aquifer were measured for several major faults. Finally, a borehole technique was evaluated with the technique.

This report presents the methods and equipment used to conduct these experiments followed by conditions at the field areas used for this study. Next the results of the imaging are presented for each major objective. This is followed by a discussion of the implications of these results and conclusions for the aquifer.

Using quarries and soil-free outcrops where possible, the lithologies of the Arbuckle-Simpson aquifer system were evaluated to determine the electrical properties of the native unfractured formations. This was performed for three formations on exposed bedrock, and one additional formation with soil cover. Other formations were imaged with the technique (See Chapter 4), but they are generally adjacent to fault zones, so interpreting the properties of the lithology absent of tectonic influences and alterations is not possible. The evaluation indicates that the lithologies of the aquifer system have a wide range of resistivities that makes the technique useful for electrical mapping in the aquifer.

Three sites were intensively investigated to evaluate the thickness, conductivity, and storage properties of the mantled epikarst of the Arbuckle-Simpson aquifer. The results indicate that the soil thicknesses available from the MIADS database correlate with the thicknesses derived from direct push depth of refusal. The results also indicate that the epikarst zone is approximately 9 times larger than the soil zone. The hydraulic conductivity of these areas is similar to the expected value for the materials present, but the analysis used resulted in values

that were smaller than larger field scale measurements. Finally, the storage potential of the mantled epikarst region appears to be the same order of magnitude as storage in the aquifer. This may influence recharge and contaminant transport on the site scale in the Arbuckle-Simpson aquifer.

For the Arbuckle-Simpson aquifer, faults are readily apparent in ERI images above and below the water table. The faults tend to be near vertical with a fault zone width that extends 5-10 meters. Springs in the aquifer that occur along faults may not necessary coincide with the most conductive regions regionally, but do correspond to conductive regions of an individual image. The fault zones tend to be uniform with depth. However, interpretation is limited to the depth that good quality data can be collected. The presence of clay zones in the images indicates that each conductive area in ERI images may not correspond to high flow zones for the aquifer.

The borehole method that was tested has proven difficult to apply to the aquifer due to a lack of suitable borehole locations to test. Few deep boreholes exist and those that do exist have problems accommodating even a small diameter cable. Surface surveys work well in the aquifer, but are limited to how deep they can easily image. A 1500 ft (460 m) borehole electrical resistivity imaging (BERI) cable was constructed and installed on a trailer with a reel to allow for deep borehole imaging. The borehole system was tested in three wells in the aquifer. The resulting field data are of good quality, but the available processing methods could provide a stable solution given the complex grid geometry of the array.

Overall, ERI is a suitable technique to assist with characterizing the Arbuckle-Simpson aquifer. The aquifer has a range of conductivities that are suitable for imaging and the images have illustrated features that would be difficult to characterize using other available techniques.

2.0 Introduction

The characterization of fractured and karstic aquifers has been attempted for many years, but our capabilities to adequately characterize these complex aquifers have not increased significantly. Much of our understanding of the flow in these aquifers has been generated from field experiments using well data or exposed rock, either in the surface or subsurface. The lack of characterization data generally comes from the cost involved in drilling, completing, maintaining and sampling wells. This cost is higher in fracture and karstic aquifers due to the higher drilling costs and the heterogeneous flow fields typically require more data than are available from discrete sampling techniques which provide only limited 2- or 3-dimensional data.

To resolve these difficulties, data are required that allow areas or volumes of the subsurface to be examined, instead of solely relying on discrete sampling data. Most importantly, methods employed need to be economical when compared to alternative techniques.

2.1 Existing techniques

Existing methods of characterizing these aquifers have relied on two detection and monitoring strategies. The first strategy involves discrete point sampling of fluids using wells, springs or multilevel piezometers whose data are integrated and interpreted. The second strategy uses indirect measurements through surface or borehole geophysical techniques.

The difficulty with point sampling techniques is that sufficient sampling can be expensive because of drilling costs, sampling time, sample analysis and data integration and interpretation time. Additionally, determining whether fractures or karst features exist between sampling locations using piezometers can be difficult to impossible to determine. This point sampling method can miss conduits not sampled by wells, or barriers to flow like vertical faults that are not sampled with a traditional piezometer monitoring grid.

2.2 Electrical Resistivity Imaging

A solution to some of these sampling problems in the vadose and phreatic zones is the utilization of electrical resistivity imaging (ERI) to provide more complete site data coverage. A temporary surface system for site evaluation can be used as an evaluation of a 2-D or 3-D portion of subsurface or cable can be installed in boreholes to image to deeper depths with higher resolution. Cables can be permanently installed in shallow trenches or in boreholes for long-term monitoring applications.

Electrical resistivity measurements have been used since the 1830's to interpret the geology of the earth (Van Nostrand and Cook, 1966). The technique introduces current into the ground and the potential field is measured. ERT (Electrical Resistance Tomography) is a method of obtaining resistivity measurements that determines the electrical conductivity of the ground using subsurface electrodes (Daily et al., 2004). In contrast, a multielectrode array uses electrodes only on the surface. Electrical Resistivity Imaging (ERI) is a general term used to indicate that a high resolution electrical resistivity technique is being used without naming each electrode configuration differently.

An electrical resistivity image is an inverted model of hundreds to thousands of four electrode resistivity measurements. A single electrical measurement does not yield significant information, similar to a single pixel on a digital photo. However, hundreds of measurements of a site can produce a 2-D or 3-D electrical image of the subsurface. This technique is occasionally used for site characterization, but it can be inefficient, expensive, or worse, ambiguous (Ramirez et al., 1993).

Common geophysical techniques are limited by several factors as outlined by Stollar and Roux (Stollar and Roux, 1975). They noted a concurrent loss in signal quality and resolution as the depth to the top of contaminated ground water increases and that there must be a significant contrast between the contaminated and uncontaminated ground water for earth resistivity surveys to be effective tools. Although the costs of earth resistivity techniques may be lower than point monitoring methods (i.e. wells) for long-term projects, the results are often difficult to correlate with objectives and still require traditional ground water sampling techniques. These problems are exacerbated by a lack of integration between geophysicists and hydrogeologists. A major problem with the application of electrical techniques to fractured rock or karstic aquifers is that most of the lithologies of these areas are strong electrical insulators. ERI work best for

identifying conductors, and therefore must “see in the dark” to be able to image these relatively high resistivity materials.

In general, flow features (such as faults that conduct fluids) and higher porosity lithologies are indicated by low resistivity anomalies. Additionally, the hydraulic parameters of the formation may be estimated using electrical methods (Purvance and Andricevic, 2000a, b). The electrical data produced from this type of study may help characterize heterogeneity, fractures, and aquifer parameters (Herwanger et al., 2004; Niwas and de Lima, 2003).

2.3 ERI for the Arbuckle-Simpson Hydrology Study

As ERI capabilities progress due to increases in field data acquisition capabilities and computing speed, the question arises as to whether ERI techniques can be employed effectively as a method to assist with the development of conceptual models for fractured rock or karstic aquifers. Can ERI provide data that would not otherwise be available using standard techniques? Can ERI be utilized in a deep borehole configuration to provide high resolution data at depth? And finally, does the Arbuckle-Simpson aquifer have sufficient conductivity to allow ERI to be performed?

The research summarized in this report addresses the above questions and is part of the larger Arbuckle-Simpson Hydrology Project. During the electrical resistivity imaging work, three features of the resulting images generated interest among the scientists evaluating the aquifer. First, the technique indicated that a consistent 30 foot (10 m) zone of conductive media exists near the surface. This is likely a zone of epikarst that would be able to store significant amounts of water. Secondly, the images have also shown significant vertical conductivity zones. The zones are not highly linear in most cases. These features are interpreted as fracture zones which can transmit water to depth in the aquifer. These features extend more than 100 ft (30 m) into the subsurface in some of the images. Finally, the method has been shown to be effective at imaging faults in the area.

The work progressed to evaluate four major objectives for ERI data in the Arbuckle-Simpson aquifer. First, the background properties of the major lithologies was assessed using quarries and outcrops. Second, the properties of the epikarst zone of the aquifer were evaluated. Third, the fault orientations in the aquifer were measured for several major faults. Finally, a borehole technique was evaluated with the technique.

This report presents the methods and equipment used to conduct these experiments followed by conditions at the field areas used for this study. Next the results of the imaging are presented for each major objective. This is followed by a discussion of the implications of these results and conclusions for the aquifer.

3.0 General Methods and Equipment

ERI is based on the measurement of electrical resistivity. The method requires precision electrical measurements to be made repeatedly. Once a sufficient number of high quality measurements have been obtained, a solution to the electrical properties of the subsurface can be obtained through inversion. A range of acquisition and processing methods were to image the subsurface of the Arbuckle-Simpson aquifer.

3.1 Resistivity

Resistance [ohms] is a fundamental property of a volume of material and is defined as the material's opposition to the flow of electrical current (Reynolds, 1997). Given a uniform cubic volume with length (L) and cross-sectional area (A), the resistance of the material will be proportional to the potential drop of an applied current (V/I). Resistivity [ohm-m] is related to this property and is expressed as a resistance through a distance, which makes it independent of material geometry. Resistance (R) and resistivity (ρ) can be expressed by the following equations (Reynolds, 1997):

$$R = V/I \quad (\text{ohms} - \Omega) \text{ (Ohm's Law)}$$

$$\rho = V/I * A/L \text{ (ohm-meters} - \Omega\text{-m)}.$$

Electrical resistivity is most commonly measured by applying a known direct or low frequency alternating current through two electrodes and measuring the potential field with another pair of electrodes. Modern technology allows this process to be controlled by automated systems with command files directing which combinations of source and potential electrodes are used and when (Ramirez et al., 1993). Automated systems are often capable of collecting hundreds to thousands of data points within an hour. Previously, hand collection systems would only acquire approximately 80 measurements per day. Additionally, advancements in inversion software allow field data to be quickly inverted and interpreted (Loke and Barker, 1996).

Resistivity can be considered to be a function of the rock porosity, volumetric fraction of saturated pores, and the resistivity of the pore water (Archie, 1942). In many cases, it is the pore fluids that contribute more to the overall resistivity signature than the host rock. Thus, for this study, one would expect that conductive anomalies are associated with larger water contents or more damaged lithologies. The signal strength in resistivity is the collected data value of voltage/current (V/I). Commonly measurements are taken twice to observe a repeatability error for each measurement.

3.2 Data Collection Instrumentation

Data were collected for this study using an Advanced Geosciences, Inc. SuperSting 8-channel resistivity instrument (Figure 1).

Figure 1. SuperSting 8-channel resistivity instrument and switchbox.

A 36-electrode and 56-electrode surface cable were used to collect surface data. The 36-electrode cable used "smart electrodes" which performed switching at the electrodes (Figure 2). The 56-electrode system performed switching with a switchbox (Figure 1).

A 28-electrode borehole electrical resistivity imaging cable (BERI) was used in the borehole surveys. The BERI cable is a new cable design and was constructed specifically for this study and mounted to a trailer (Figure 3). The BERI cable has electrodes spaced at 1.0 m (3.3 ft) spacing for the lowest 15 meters (49.2 ft) of the cable, and then the additional electrodes are placed at increments such that the total electrode bearing portion of the cable is 80 meters (262.5 ft) long. The BERI cable is capable of taking measurements to a depth of ~ 450 m (1476

ft). Surface surveys were conducted using only the SuperSting and the 36-electrode cable. Subsurface surveys utilized a switchbox to communicate to the borehole cable (Figure 1).

Figure 2. Surface electrodes used to collect resistivity data.

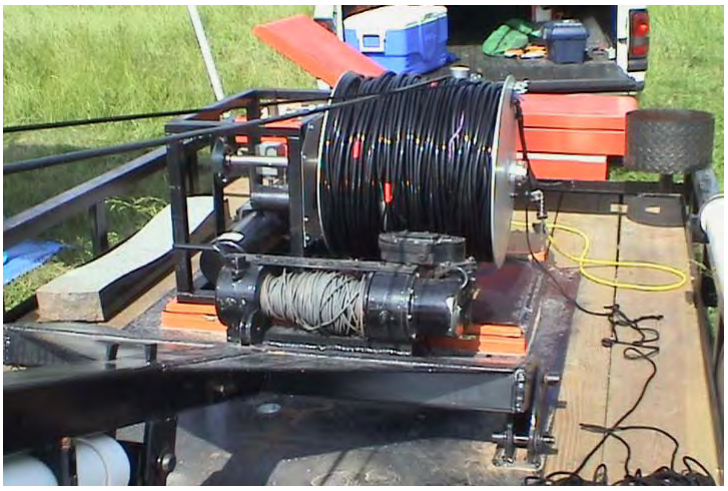

Figure 3. BERI cable used for borehole surveys on trailer at site Wingard 2.

Data inversion was performed using AGI EarthImager software and proprietary software owned by Oklahoma State University. These software were used for both surface surveys and borehole surveys.

3.3 Data Collection

At each site a series of surface ERI surveys were conducted at 14 sites across the area (Figure 4; Table 1). Each survey was collected using a line of 36 or 56 electrodes with spacing ranging from 1.25 – 10.00 meters. The electrode spacing depended on the space available at the site, the desired imaging depth, and the desired image resolution. Wider spacing of the electrodes allows greater imaging depth but at a lower resolution. An OSU proprietary method (the Halihan-Fenstemaker method) was used to collect and process the data for the surveys (Halihan et al., 2005). This method was developed for contaminant imaging investigations and provides a significant increase in image resolution when compared to common resistivity methods.

In addition to the surface lines, the BERI cable was temporarily installed vertically into the subsurface in three locations by lowering it down into existing water wells. Prior to installation of the BERI a weight, attached to a 500 m (1640 ft) rope, is lowered into the well to probe for obstructions. After the vertical installation, horizontal surface lines were rotated about the vertical cable to generate wedge shaped electrical resistivity images of the subsurface.

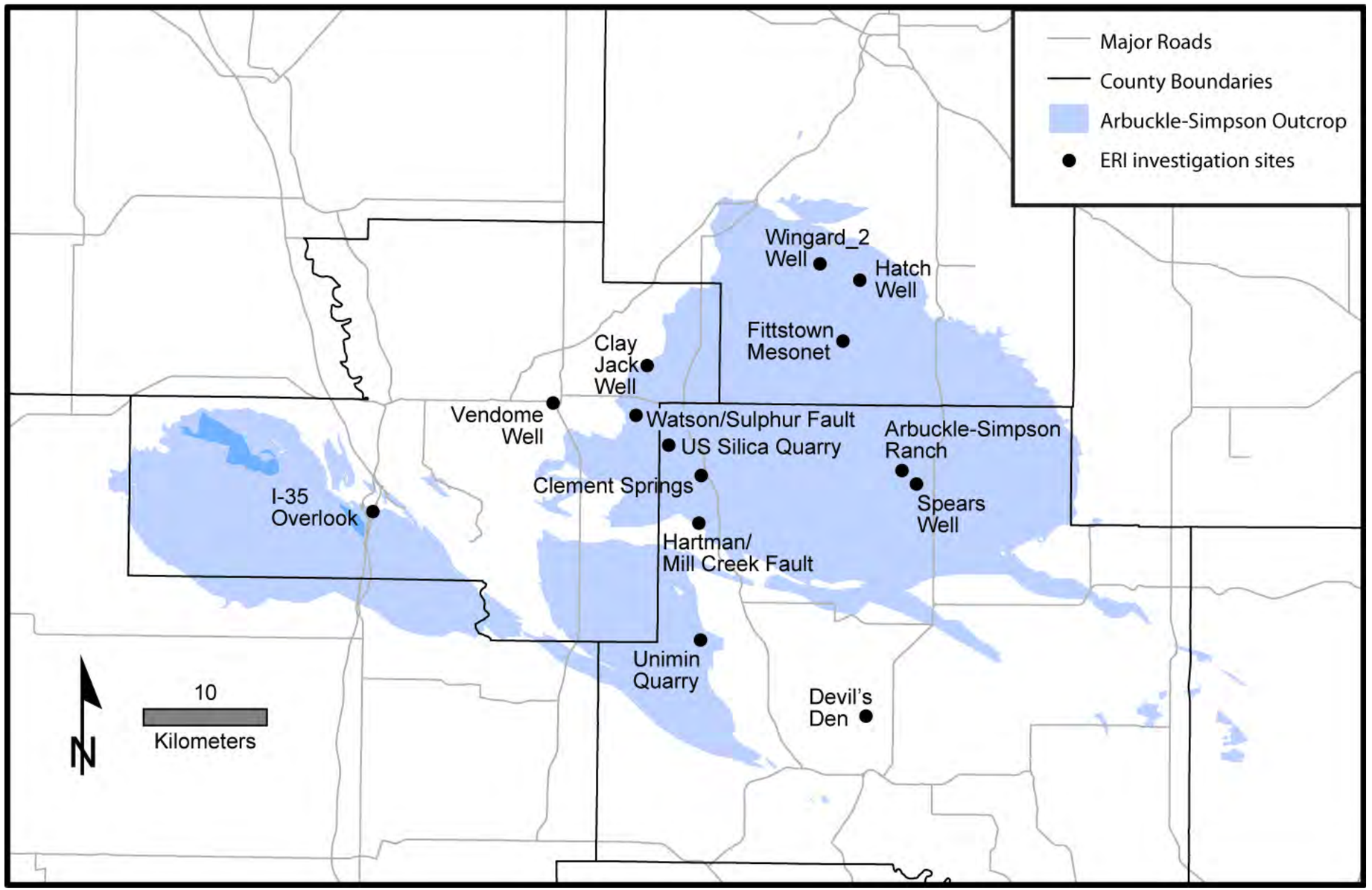

Figure 4. Map of field sites investigated using electrical resistivity imaging over the Arbuckle-Simpson aquifer area.

Table 1. OSU Electrical Resistivity Imaging Data Summary - Arbuckle-Simpson Aquifer

Site Name	File Number	Line Name	Collection Date	Electrode spacing	Total Line Length	Number of Electrodes	First Electrode Location		Last Electrode Location		Thesis/Report	Datum
				meters	meters	#	LAT	LONG	LAT	LONG		
Arbuckle-Simpson Ranch	1	AS1.25C1	26-Jul-07	1.25	68.75	56	N 34° 27' 31.500"	W -96° 39' 52.488"	N 34° 27' 33.312"	W -96° 39' 54.042"	Sample 2008	WGS 84
	2	ASR5.00B	29-Feb-08	5	275	56	N 34° 27' 28.532"	W -96° 39' 50.171"	N 34° 27' 35.874"	W -96° 39' 56.274"	Sample 2008	WGS 84
	3	QTZSG01	18-Nov-07	9	495	56	N 34° 27' 30.251”	W -96° 39' 50.495”	N 34° 27’ 18.235”	W -96° 40’ 3.363”	Cemen et al 2008	WGS 84
	4	AS2.5B1	26-Jul-07	2.5	137.5	56	N 34° 27' 29.922"	W -96° 40' 6.178"	N 34° 27' 34.302"	W -96° 40' 6.714"	Cemen et al 2008	WGS 84
	5	ASRWE01A	29-Feb-08	5	275	56	N 34° 27' 36.120"	W -96° 40' 3.358"	N 34° 27' 34.503"	W -96° 39' 52.771"	Cemen et al 2008	WGS 84
Clement Springs	6	CMT01	01-Jun-06	10	550	56	*N 34° 27' 14.9"	*W -96° 50' 36.4"	*N 34° 27' 32.8"	*W -96° 50' 36.4"	Riley 2007	WGS 84
	7	CMT02	02-Jun-06	4	220	56	*N 34° 27' 17.7"	*W -96° 50' 40.7"	*N 34° 27' 22.4"	*W -96° 50' 34.0"	Riley 2007	WGS 84
Devil's Den	8	DEV01	17-Nov-07	2	66	34	N 34° 16' 49.287"	W -96° 41' 41.724"	N 34° 16' 50.020"	W -96° 41' 39.300"	Cemen et al 2008	WGS 84
	9	DEV02	17-Nov-07	2	66	34	N 34° 16' 49.287"	W -96° 41' 41.724"	N 34° 16' 50.020"	W -96° 41' 39.300"	Cemen et al 2008	WGS 84
	10	DEV03	17-Nov-07	1.5	82.5	56	N 34° 16' 47.373"	W -96° 41' 39.016"	N 34° 16' 47.462"	W -96° 41' 35.799"	Cemen et al 2008	WGS 84
Fittstown Mesonet	11	FM00001A	10-May-06	1.25	68.75	56	N 34° 33' 8.210"	W -96° 43' 4.794"	*N 34° 33' 5.89"	*W -96° 43' 4.70"	This report	NAD83
	12	FM00002A	10-May-06	2.5	137.5	56	N 34° 33' 9.289"	W -96° 43' 4.831"	*N 34° 33' 4.81"	*W -96° 43' 4.66"	This report	NAD83
	13	FM04501A	10-May-06	1.25	68.75	56	N 34° 33' 7.885"	W -96° 43' 3.796"	*N 34° 33' 6.22"	*W -96° 43' 5.70"	This report	NAD83
	14	FM04502A	11-May-06	2.5	137.5	56	N 34° 33' 8.466"	W -96° 43' 2.837"	*N 34° 33' 5.64"	*W -96° 43' 6.66"	This report	NAD83
	15	FM09001A	11-May-06	1.25	68.75	56	N 34° 33' 7.096"	W -96° 43' 3.367"	*N 34° 33' 7.01"	*W -96° 43' 6.13"	This report	NAD83
	16	FM09002A	11-May-06	2.5	137.5	56	N 34° 33' 6.990"	W -96° 43' 2.122"	*N 34° 33' 7.11"	*W -96° 43' 7.37"	This report	NAD83
	17	FM13501B	12-May-06	1.25	68.75	56	N 34° 33' 6.389"	W -96° 43' 3.766"	*N 34° 33' 7.71"	*W -96° 43' 5.73"	This report	NAD83
	18	FM13502A	12-May-06	2.5	137.5	56	N 34° 33' 5.579"	W -96° 43' 2.889"	*N 34° 33' 8.52"	*W -96° 43' 6.61"	This report	NAD83
Hartman/Mill Creek Fault	19	HRTMN1	04-Aug-04	9	315	36	N 34° 25' 09.7"	W -96° 50' 41.7"	*N 34° 24' 59.4"	*W -96° 50' 41.7"	Halihan et al 2004	NAD83
	20	HRTMN2	04-Aug-04	3	105	36	*N 34° 25' 02.8"	*W -96° 50' 41.7"	*N 34° 24' 59.4"	*W -96° 50' 41.7"	Halihan et al 2004	NAD83
	21	HRTMN3	04-Aug-04	9	315	36	*N 34° 25' 00.6"	*W -96° 50' 41.7"	*N 34° 24' 50.4"	*W -96° 50' 41.7"	Halihan et al 2004	NAD83
	22	HRTMN4	04-Aug-04	3	105	36	*N 34° 25' 00.5"	*W -96° 50' 41.7"	*N 34° 24' 57.1"	*W -96° 50' 41.7"	Halihan et al 2004	NAD83
	23	HRTMN5	04-Aug-04	3	105	36	*N 34° 24' 57.6"	*W -96° 50' 41.7"	*N 34° 24' 54.2"	*W -96° 50' 41.7"	Halihan et al 2004	NAD83
	24	DH01PERP	14-Mar-06	5, 9 and 10	526	64	*N 34° 25' 6.6"	*W -96° 50' 33.0"	*N 34° 24' 49.7"	*W -96° 50' 43.8"	Riley 2007	NAD83
	25	DH02N30W	16-Mar-06	9 and 10	594	64	*N 34° 25' 3.9"	*W -96° 50' 44.0"	*N 34° 24' 47.0"	*W -96° 50' 32.8"	Riley 2007	NAD83
	26	DH02PARA	16-Mar-06	5	175	36	*N 34° 24' 53.4"	*W -96° 50' 38.7"	*N 34° 24' 50.4"	*W -96° 50' 32.8"	Riley 2007	NAD83
Hatch Well Site	27	HHSU000	16-Jul-04	1.5	52.5	36	N 34° 35' 47.6"	W -96° 42' 12.2"	*N 34° 35' 49.2"	*W -96° 42' 12.2"	Halihan et al 2004	NAD83
	28	HHSU050	16-Jul-04	1.5	48	33	N 34° 35' 47.6"	W -96° 42' 12.2"	*N 34° 35' 48.5"	*W -96° 42' 10.7"	Halihan et al 2004	NAD83
	29	HHSU100	16-Jul-04	1.5	52.5	36	N 34° 35' 47.6"	W -96° 42' 12.2"	*N 34° 35' 47.2"	*W -96° 42' 10.2"	Halihan et al 2004	NAD83
	30	HHSU150	16-Jul-04	1.5	52.5	36	N 34° 35' 47.6"	W -96° 42' 12.2"	*N 34° 35' 46.0"	*W -96° 42' 11.2"	Halihan et al 2004	NAD83
	31	HWNO1MA1	02-Sep-06	1.25	68.75	56	*N 34° 35' 44.7"	*W -96° 42' 10.37"	*N 34° 35' 42.5"	*W -96° 42' 10.37"	Sample 2008	NAD83

Table 1. OSU Electrical Resistivity Imaging Data Summary - Arbuckle-Simpson Aquifer

Site Name	File Number	Line Name	Collection Date	Electrode spacing	Total Line Length	Number of Electrodes	First Electrode Location		Last Electrode Location		Thesis/Report	Datum
				meters	meters	#	LAT	LONG	LAT	LONG		
	32	HWNO1MB1	02-Sep-06	1.25	68.75	56	*N 34° 35' 45.8"	*W -96° 42' 10.37"	*N 34° 35' 43.6"	*W -96° 42' 10.37"	Sample 2008	NAD83
	33	HWNO1MC1	03-Sep-06	1.25	68.75	56	*N 34° 35' 43.6"	*W -96° 42' 10.37"	*N 34° 35' 41.4"	*W -96° 42' 10.37"	Sample 2008	NAD83
	34	HWNO2MA1	02-Sep-06	2.5	137.5	56	*N 34° 35' 45.8"	*W -96° 42' 10.37"	*N 34° 35' 41.4"	*W -96° 42' 10.37"	Sample 2008	NAD83
	35	HWN02MA2	19-Mar-07	2.5	137.5	56	*N 34° 35' 45.8"	*W -96° 42' 10.37"	*N 34° 35' 41.4"	*W -96° 42' 10.37"	Sample 2008	NAD83
	36	HWNO5MA1	02-Sep-06	5	275	56	N 34° 35' 48.1"	W -96° 42' 10.37"	*N 34° 35' 39.1"	*W -96° 42' 10.37"	Sample 2008	NAD83
I-35 Overlook	37	I35	30-May-06	2.5	137.5	56	*N 34° 25' 31.7"	*W -97° 8' 6.6"	*N 34° 25' 35.9"	*W -97° 8' 4.4"	Riley 2007	WGS 84
	38	SW1.25A1	11-Jun-07	1.25	33.75	28	*N 34° 26' 56.5"	*W -96° 39' 5.3"	*N 34° 26' 57.2"	*W -96° 39' 6.2"	Sample 2008	NAD83
	39	SW1.25A2	11-Jun-07	1.25	33.75	28	*N 34° 26' 57.2"	*W -96° 39' 6.2"	*N 34° 26' 58.0"	*W -96° 39' 7.2"	Sample 2008	NAD83
	40	SW1.25B1	12-Jun-07	1.25	68.75	56	*N 34° 26' 57.2"	*W -96° 39' 6.2"	*N 34° 26' 58.8"	*W -96° 39' 8.1"	Sample 2008	NAD83
Spears Well Site	41	SW1.25C1	12-Jun-07	1.25	68.75	56	*N 34° 26' 58.0"	*W -96° 39' 7.2"	*N 34° 26' 59.6"	*W -96° 39' 9.2"	Sample 2008	NAD83
	42	SW2.5A1	12-Jun-07	2.5	137.5	56	*N 34° 26' 56.5"	*W -96° 39' 5.3"	*N 34° 26' 59.6"	*W -96° 39' 9.2"	Sample 2008	NAD83
	43	WSWSN15W	13-Jul-05	6	210	36	N 34° 27' 3.1"	W -96° 39' 12.0"	*N 34° 26' 56.5"	*W -96° 39' 10.1"	This report	NAD83
	44	WS11N75E	14-Jul-05	3	105	36	N 34° 27' 0.6"	W -96° 39' 13.6"	*N 34° 27' 1.4"	*W -96° 39' 9.6"	This report	NAD83
	45	WS21N75E	14-Jul-05	3	105	36	N 34° 26' 59.2"	W -96° 39' 11.8"	*N 34° 26' 00.0"	*W -96° 39' 7.8"	This report	NAD83
Unimin Quarry	46	UNIMINEW	04-Mar-05	1	35	36	N 34° 20' 4.6"	W -96° 50' 33.3"	N 34° 20' 4.5"	W -96° 50' 34.5"	This report	NAD83
	47	UNIMINNS	04-Mar-05	2	70	36	N 34° 20' 5.4"	W -96° 50' 34.2"	N 34° 20' 3.5"	W -96° 50' 33.7"	This report	NAD83
	48	USN30E2	07-Jul-05	2	70	36	N 34° 28' 32.4"	W -96° 52' 20.4"	*N 34° 28' 30.3"	*W -96° 52' 19.1"	This report	NAD83
US Silica Quarry	49	USP09	08-Jul-05	1	35	36	N 34° 28' 32.2"	W -96° 52' 19.8"	*N 34° 28' 32.7"	*W -96° 52' 18.6"	This report	NAD83
	50	USP18	09-Jul-05	1	35	36	N 34° 28' 31.7"	W -96° 52' 19.4"	*N 34° 28' 32.1"	*W -96° 52' 18.2"	This report	NAD83
	51	USP23	10-Jul-05	1	35	36	N 34° 28' 31.3"	W -96° 52' 19.2"	*N 34° 28' 31.8"	*W -96° 52' 18.0"	This report	NAD83
Vendome Well	52	VENDOM01	14-Nov-04	6 and 9	486	64	*N 34° 30' 20.5"	*W -96° 58' 33.7"	*N 34° 30' 20.4"	*W -96° 58' 14.47"	This report	NAD83
	53	WATSON01	10-Aug-05	9	315	36	N 34° 29' 49.70"	W -96° 54' 7.02"	*N 34° 29' 39.42"	*W -96° 54' 7.02"	This report	NAD83
Watson/ Sulphur Fault	54	WATSON02	10-Aug-05	3	105	36	*N 34° 29' 47.6"	*W -96° 54' 7.02"	*N 34° 29' 44.19"	*W -96° 54' 7.02"	This report	NAD84
	55	WATSON03	11-Aug-05	3	105	36	N 34° 29' 45.85"	*W -96° 54' 7.02"	*N 34° 29' 42.4"	*W -96° 54' 7.02"	This report	NAD85
Clay Jack Well	56	CLAYJACK	5/31-6/2/2005	varies	vertical	varies	N 34° 32' 0.5644"	W -96° 53' 32.15"	N 34° 32' 0.5644"	W -96° 53' 32.15"	This report	From Completion Report
Wingard 2 Well	57	W2S45DEG	15-Jul-04	5	175	36	N 34° 36' 30.1"	W -96° 44' 19.9"	*N 34° 36' 36.1"	*W -96° 44' 15.9"	Halihan et al 2004	NAD83
	58	WNGD006	12-May-04	5	160	33	N 34° 36' 30.1"	W -96° 44' 19.9"	*N 34° 36' 35.2"	*W -96° 44' 20.0"	Halihan et al 2004	NAD83

* indicates that the location is approximated, not measured with GPS instrument

Table 1. OSU Electrical Resistivity Imaging Data Summary - Arbuckle-Simpson Aquifer

4.0 Site Descriptions

Fourteen sites were surveyed between 2004-2008 (Figure 4). The criteria for the well sites varied based on the range of objectives that they were collected. The criteria for each objective is discussed further in each chapter. Several potential ERI sites were identified but not visited due to time constraints or the absence of permission from land owners. Each site is described in sequence from Table 1.

4.1 Arbuckle-Simpson Ranch

The Arbuckle-Simpson Ranch site is located approximately 1.8 miles WNW of Connerville in Johnston County, Oklahoma (Figure 4). The Arbuckle-Simpson Ranch site is underlain by the rocks of the West Spring Creek formation. The topography at the site is gently rolling to essentially flat lying. Soil cover is continuous in the flat lying area of investigation. Rocks were observed exposed at the surface to the west of the area of investigation and to the east on hill slopes. The site has a history of use as rangeland for cattle. A spring fed pond is located on the site and numerous springs have been identified on the property that contributes of the flow to the Blue River. An inferred fault is identified in the literature as crossing the site from the south west to the north east (Fairchild et al., 1990). Five ERI lines were collected on the site to investigate epikarst development and groundwater/surface water interactions (Figure 5). Two of the lines were cored with direct push for epikarst evaluation (Figure 6).

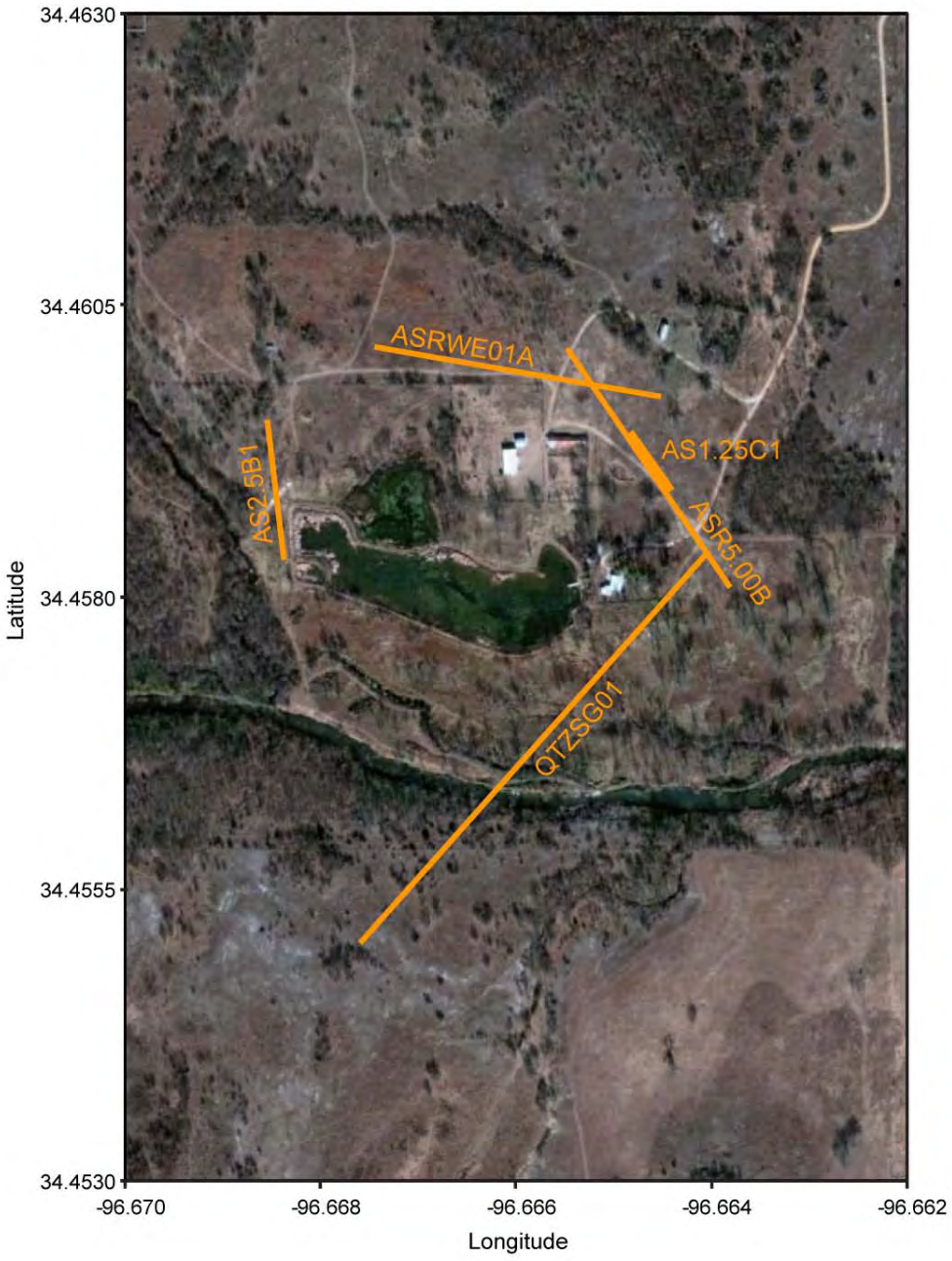

Figure 5. Arbuckle-Simpson Ranch site showing location of ERI lines. Aerial photo courtesy of Google Earth.

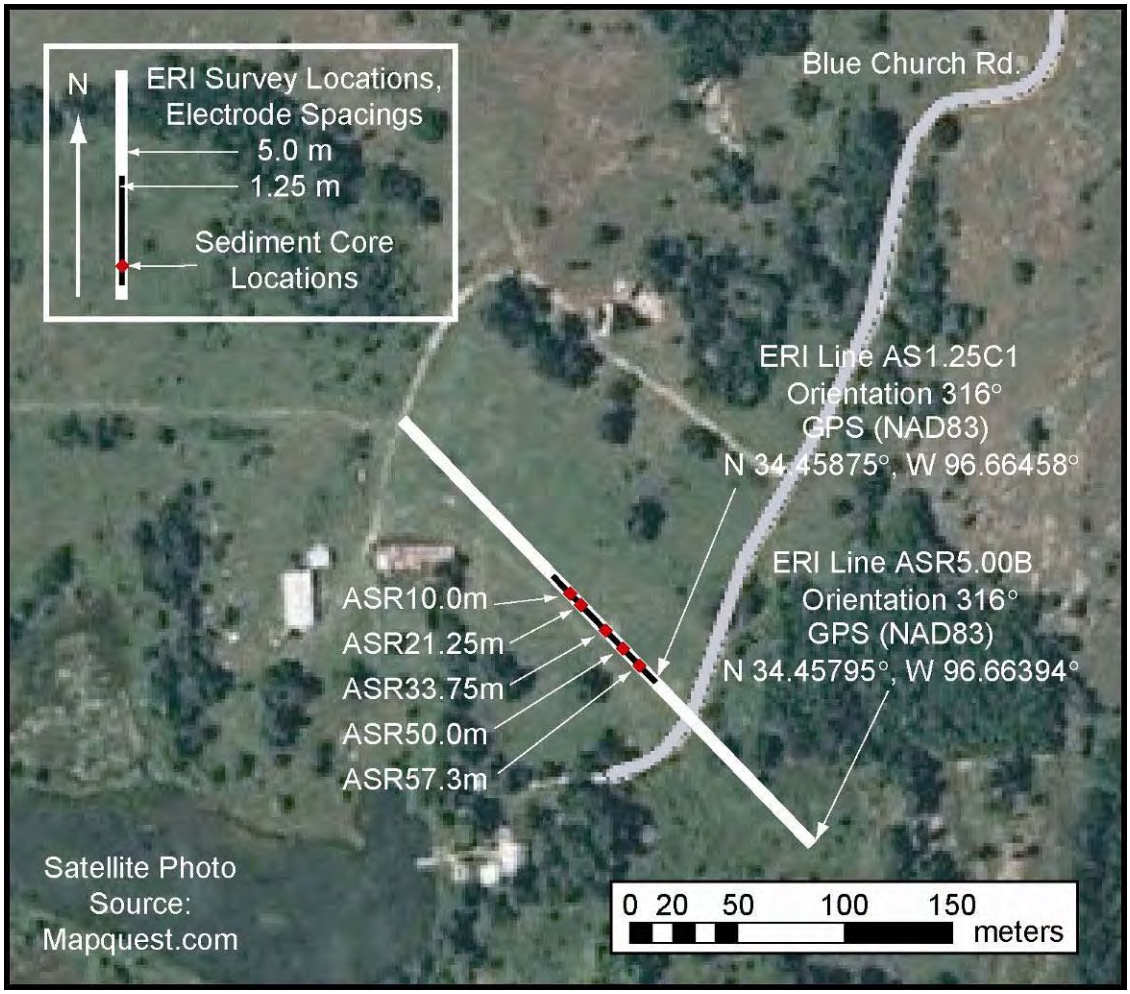

Figure 6. Arbuckle-Simpson Ranch site map with surface electrical resistivity and direct push locations (from Sample, 2008). Aerial photo courtesy of Mapquest.

4.2 Clement Springs

The second field site in this study is Clement Spring along the South Sulphur Fault. This property is located approximately 4 miles to the north of Mill Creek, OK. The primary land use is for cattle production. The property is approximately one half section in size.

The terrain at the site is rough to the south with dolomite exposed at the surface, which forms a small hill with the main axis of the hill trending E-W. The dolomite exposure ends about 1/5 of a mile north of the south property line. North of the dolomite exposure is a change in rock type to a loose sandstone. This formation is weathered and provides gradual sloping hills. The southern edge of this formation is where a house is located. Just north of the house is an erosional gully, formed by a small ephemeral creek. Clement Spring is located toward the west end of the property along this creek. North of the creek bed is a gradually sloping hill that rises approximately 20 feet in elevation. This hill slopes back down to the north end of the site. Roads pass along the east and west side of the site. At the southern edge of the site is the Martin-Marietta quarry. The site is lightly forested along the creek bed and contains a large amount of poison ivy. The dolomite exposure is mostly populated by succulents, hardy grasses, and bushes. The sandstone areas are covered with prairie grasses.

Two surveys were completed at this site (Figure 7). The first survey was a 56 electrode survey starting at the southern edge of the site and extending to the north. The electrodes were spaced at a distance of 10 meters apart giving a total line length of 550 meters and providing a depth of investigation of ~110 meters. The second line on the site was a 56 electrode survey starting SW of the fault and trending to the NE. An electrode spacing of 4 meters was used giving a total line length of 220 meters and providing a depth of investigation of ~44 meters.

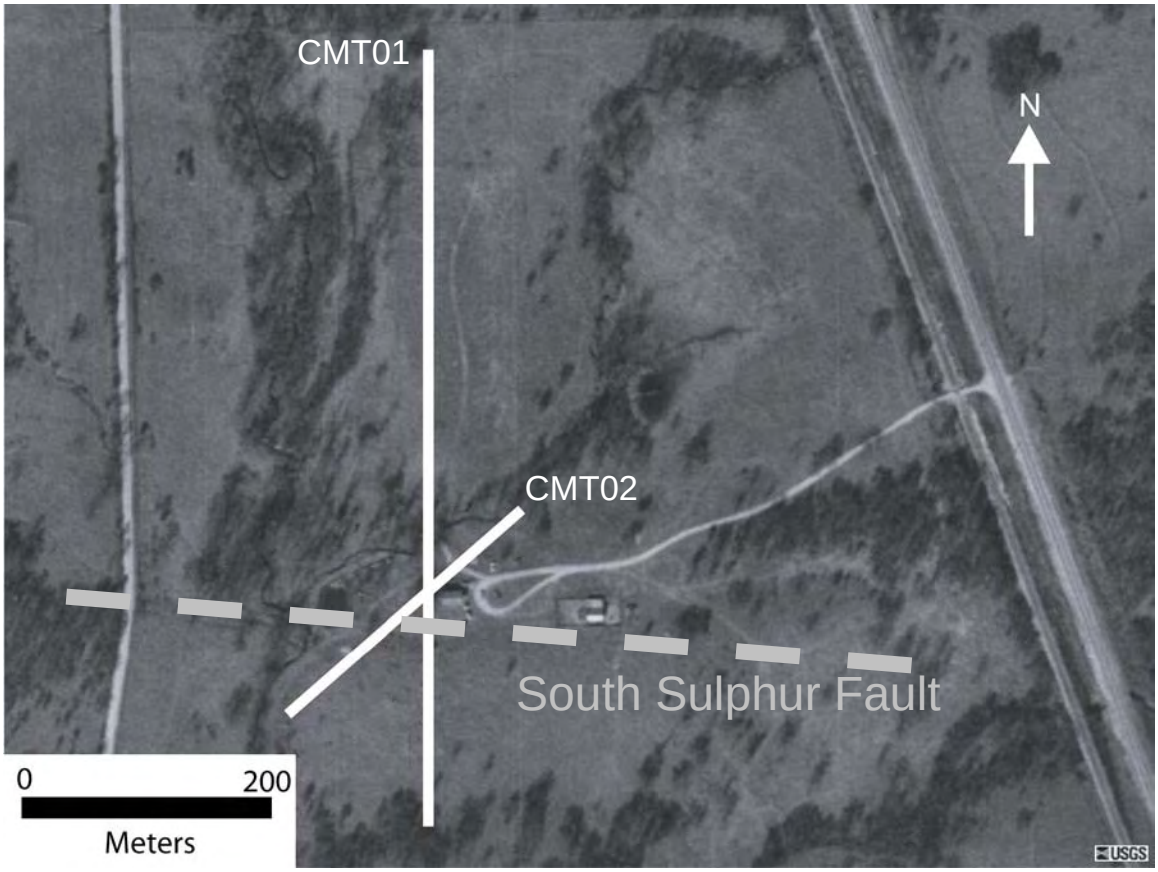

Figure 7. Clement Springs site location map showing electrode line locations (from Riley, 2007). Aerial photo courtesy of USGS.

4.3 Devil's Den

The third site is in the Devil's Den area of Tishomingo, Oklahoma where Precambrian age Tishomingo granite is exposed at the surface. These granites are about 1.35 to 1.4 billion years old and form much of what geologists call the "basement" of southern Oklahoma (Suneson, 1997). The granite is highly fractured in places and is an excellent site for our work because of the clean exposure of rock in the area. The granitic environment does present a challenge for drilling holes to plant electrodes in the ground for electrical resistivity work.

Two ERI lines were collected with a repeated file resulting in three files of data. The first two lines (DEV01 and DEV02) were collected using metal plates attached to the outcrop with water based conductive medical gel. The second line (DEV03) was collected normally with resistivity stakes inserted into soil.

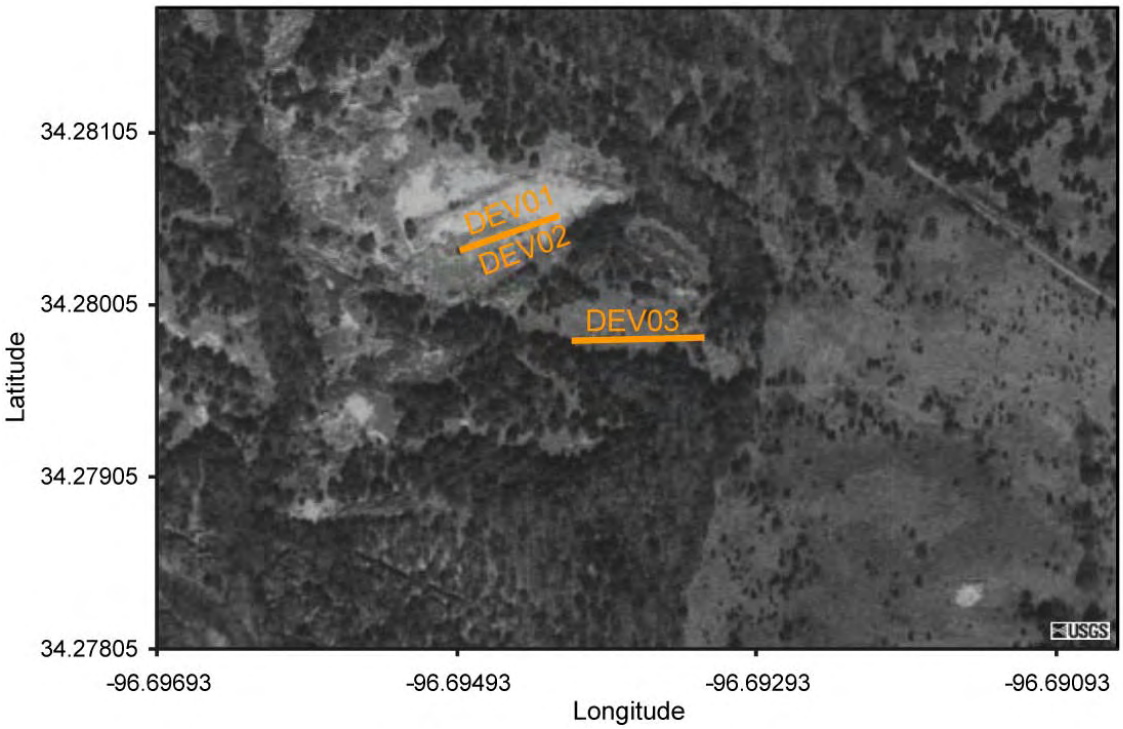

Figure 8. Devil's Den site location map showing electrode line locations. Aerial photo courtesy of USGS.

4.4 Fittstown Mesonet

Rotational ERI data was collected at the Fittstown Mesonet site. The site is located over the West Spring Creek dolomite and provides the home for the Mesonet station located in the area. A set of eight ERI dataset were collected at the site for epikarst evaluation, but wet weather prevented drilling from occurring on the site, so no correlation data for epikarst analysis is available.

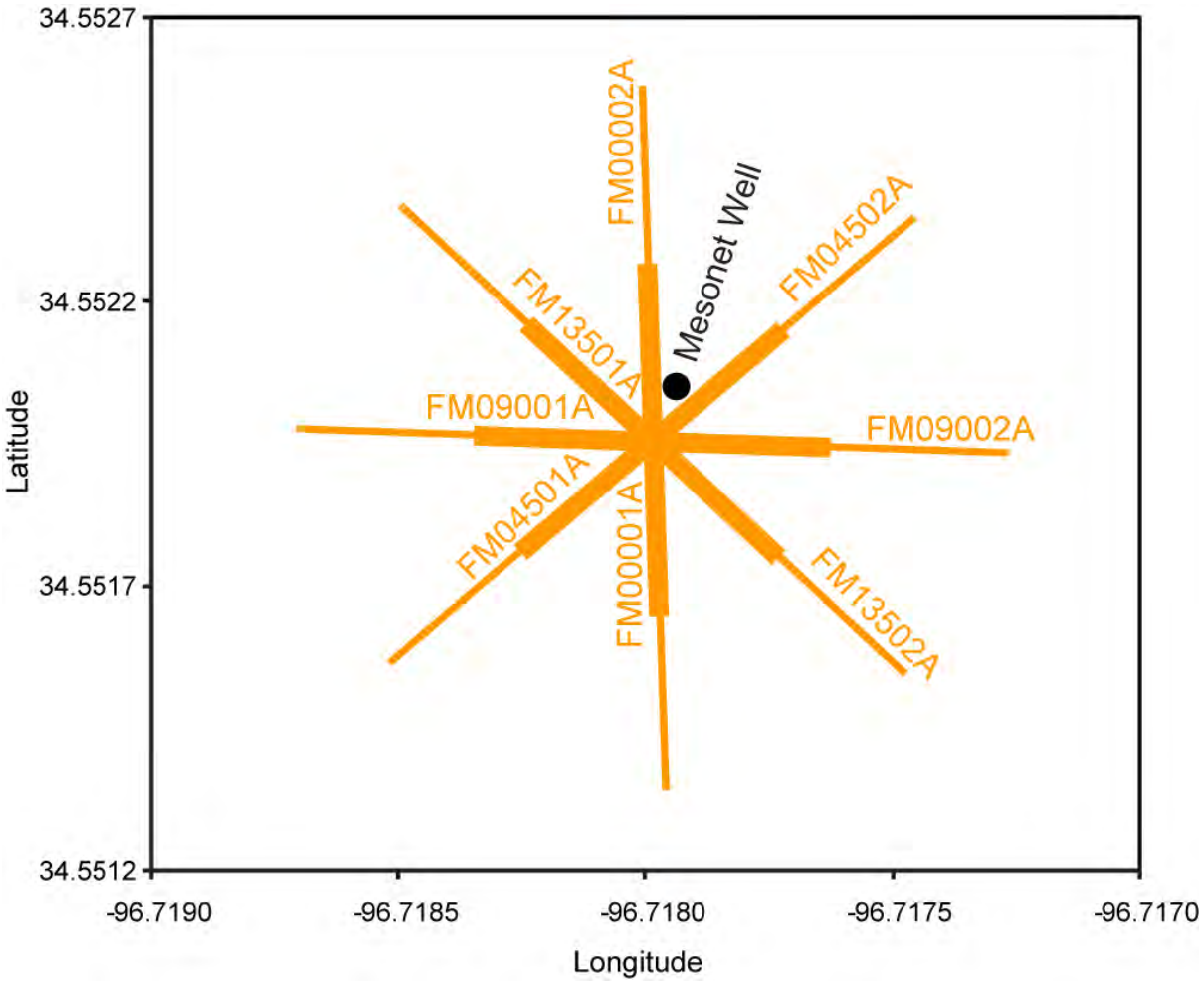

Figure 9. Fittstown mesonet site location map showing electrode line locations.

4.5 Hartman/Mill Creek Fault

The Hartman "Mill Creek Fault" site was located ~ 1.5 miles NW of Mill Creek, Oklahoma, SE of the corner of Colvert (E1790 Rd.) and Frisco (N3460 Rd.) Roads. The legal location was NW ¼, Section 1, Township 2S, Range 4E of the Indian Meridian. The northern boundary of the site was parallel to and coincident with the end of Colvert Rd. The terrain on the site was gently rolling at the north end. The upper part of a hill was in the north-west corner of the site with slopes to the east and south of this corner. The hill peaked just to the NW corner of the property. A sinkhole was identified approximately 60 feet south of the northern boundary and approximately 160 feet east of the survey line Hartman_1. The surface expression of the sinkhole was a 16 ft diameter depression that is approximately 15 ft deep. The sinkhole was steep sided and free of standing water although moisture was present at the bottom, which supported the growth of moss. The site was free of any significant obstructions other than a couple of small groves of trees. The fence along the western edge of the site was a wire fence with wood posts that were not expected to present any 3-D effects in our ERI images. There was also a recently constructed power line that abuts the western edge of the site; however it was not anticipated to cause any problems. The site was used as grazing range for cattle by the landowner. The Kindblade Group was on the north side of the fault while the Deese group was on the south side of the fault.

The line perpendicular to the fault (DH01Perp) started in a small valley and went uphill as it traversed to the south-west. The terrain slowly roses until it reached a total height 6 meters above the valley at around 414 m along the line. Over this rise there was a gradual drop off of about 4 meters to the end of the total line length of 526 meters. The south-west end of this line abutted the fence on the west side of the site. Line DH02N30W trended N30W. This line started in the NW corner of the site about 30 meters south of the north-west corner of the fence. The line started on the top of a hill and trended downhill for the entire run of the line at a rate of about .02 meters/meter or 2%. DH03Para ran parallel to the fault. There was not much elevation change along this line.

During two separate trips to the Hartman "Mill Creek Fault" site a total of 5 surface ERI surveys along a North-South line and 3 surveys rotating around the fault were collected (Table 1). Two of the measurements, ERI lines Hartman_1 and Hartman_3, were taken at 9.0-m (29.5 ft) electrode spacing and had an overlap of five electrodes. This configuration yielded a total of 67 electrodes along a line that acquired data over a length of 594 m (1949 ft), and a depth of 75 m (250 ft) (Figure 6). ERI lines Hartman_2 and Hartman_4 had a twelve electrode overlap and

ERI lines Hartman_4 and Hartman_5 had a six electrode overlap (Table 1). This configuration yielded a total of 90 electrodes along a line that acquired data over a length of 267 m (875 ft), and to a depth of approximately 23 m (75 ft) (Figure 6). The 3.0-m (9.8 ft) dataset was taken near the center of the 9.0-m (29.5 ft) dataset. The sets of data were linked together by overlapping common electrodes (Table 1).

DH01Perp was taken perpendicular to the fault. The first 28 electrodes were at 10.0-m spacing, 101-118 were at a 9.0-meter spacing, and 119-136 were at a 5.0-meter spacing due to space constraints of the roadway. This provided for a 54 electrode line with a total line length of 526 meters and imaging to a depth of approximately 65 m. DH02N30W was the longest line at 594 meters while still using a 54 electrode setup. Electrodes 1-28 were at a spacing of 10.0-m while 101-136 were at 9.0-m spacing. This line at 594 meters provided for an image to a depth of approximately 75 m. DH03Para was parallel to the fault surface. An electrode spacing of 5 m was used and the 36 smart electrodes were the only electrodes used in this survey. The total line length for this line was 175 m and provided image resolution down to approximately 22 m (Table 1).

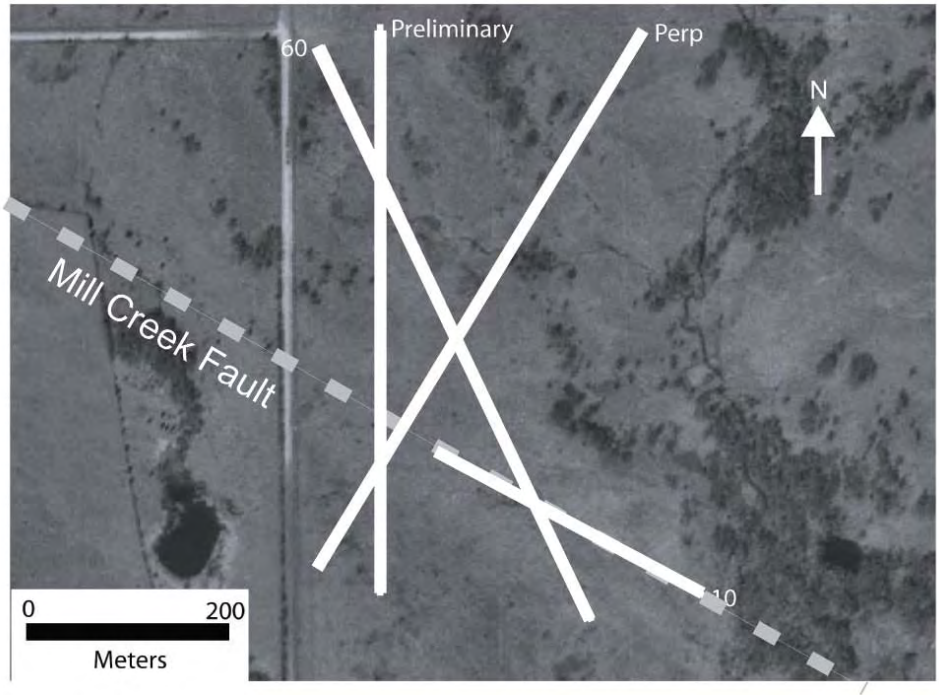

Figure 10. Hartman/Mill Creek Fault site location map with electrode line locations (from Riley, 2007). Aerial photo courtesy of USGS.

4.6 Hatch Well Site

The Hatch Well site is located approximately four miles WSW of Fittstown, Oklahoma, 0.4 miles north of E1670 Rd. on N3540 Rd. The legal location for the site is 02N-06E-32 CBA and is designated as USGS Site # 343558096420401. The gate to the property is on the east side of N3540 Rd. The well is located ~250 ft north of the gate and 5.6 m (18 ft) east of the fence line paralleling the road. The well is being used as a long term water level recording site by the OWRB. A long cinder block and concrete building runs along a NW-SE trend 50.3 m (165 ft) NE of the well. The site is relatively level and otherwise free of obstructions for ~ 200 ft in an arc from 0° to 160° from north. Several trees dot the site (Figure 11).

A set of four ERI lines were collected as part of an experiment with the BERI cable (Table 1). The depth of the well is logged as 201 feet total depth but was found to be obstructed below the depth of 145 feet. The depth to water was measured at 88 feet (26.75 m) from the top of casing (TOC). The BERI cable was temporarily installed in the well. The well held 23 out of 28 of the BERI cable's electrodes. Electrode 23 was 13 feet (4 m) below TOC. Only the lowest 16 electrodes of the BERI cable were in water and were used in ERI surveys at this site. The electrode spacing for the horizontal surface line was 1.5 m (4.9 ft). The horizontal surface line was rotated about the vertical cable at 0°, 50°, 100°, and 150° (Figure 11). Due to the proximity of the building, the line acquired at 50° was only 49.5 m (162 ft) long and utilized only 34 electrodes. Four pairs of surface and borehole ERI surveys were collected at the well. The west side of the well could not be surveyed due to a fence and a gravel road. One borehole image (due north) and the four surface images were inverted.

A second set of six surface ERI lines were collected as part of the epikarst evaluation. These north-south lines were collected south of the well on the site (Figure 12).

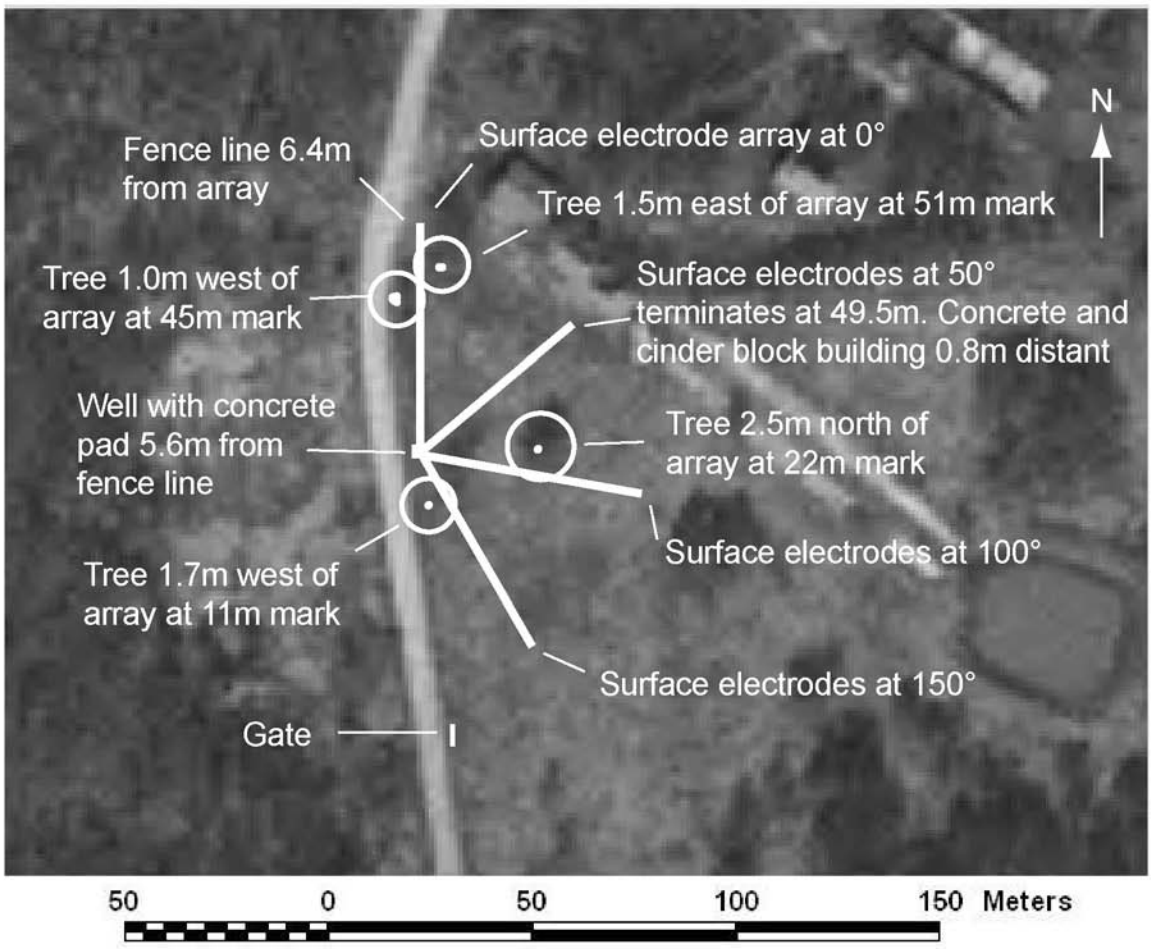

Figure 11. Hatch Well Site with location of surface electrode placement and other line features noted (from Halihan et al, 2004). Aerial photo courtesy of USGS.

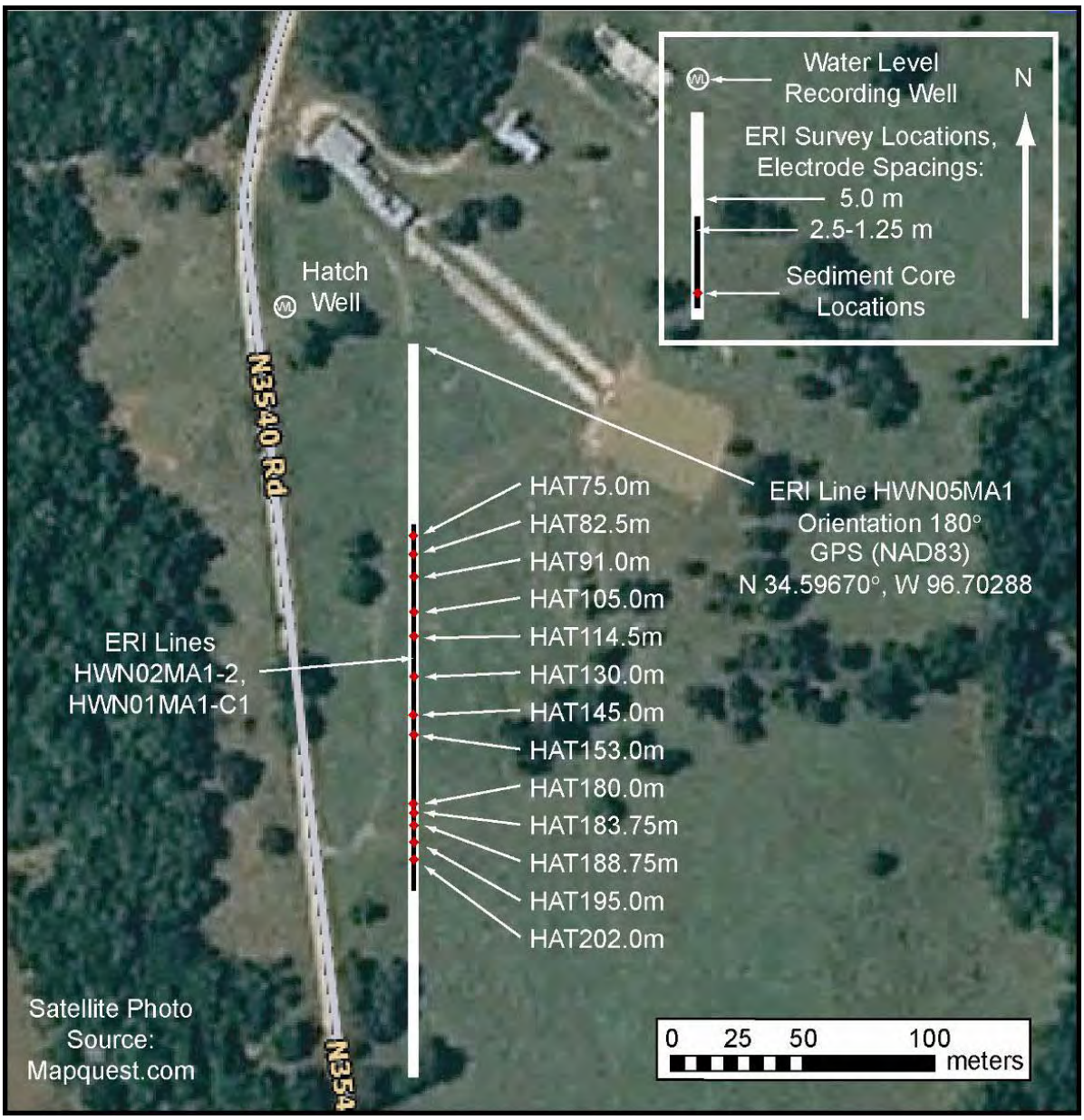

Figure 12. Hatch site map with surface electrical resistivity, direct push, and well locations (from Sample, 2008). Aerial photo courtesy of Mapquest.

4.7 I-35 Overlook

This field site is on interstate 35 (I-35) at the scenic turnout, mile marker 49. This turnout is a road cut for I-35 that provides a good exposure of the Collings Ranch Conglomerate. This is an area where the conglomerate has been thrust over the surrounding rocks and provides an exposed fault that can be used to correlate to ERI data. The site is on the limb of an anticline–syncline pair; however, the exposure itself is a hill. A metal post and metal mesh fence runs along the top of the hill to protect people from falling off of the exposed cliff face. The posts for this fence were set in concrete. Along the top of the hill is a mixed variety of evergreen trees and a little bit of grasses. A portion of the hill has been paved to provide a parking area for people that turn off into the turnout. Along the base of the hill is some gravel along with grasses and a few small trees.

One line was collected at this field site. It is an approximately south to north 56 electrode line. An electrode spacing of 2.5 meters was used giving a total line length of 137.5 meters and a depth of investigation of approximately 27.5 meters. This site was difficult due to the traffic and required drilling to obtain contact with the electrodes.

Figure 13. I-35 Mile Marker 49 site location showing the electrode line location (from Riley, 2007). Aerial photo courtesy of USGS.

4.8 Spears Well Site

The Spears Ranch site is located approximately one mile west of Connerville in Johnston County, Oklahoma (Figure 1). The Spears Ranch site is underlain by the rocks of the West Spring Creek formation.

The area of investigation was just south of the Blue River. The topography at the site is gently rolling and slopes towards the Blue River. The slope of the terrain is greatest close to the Blue River. Soil cover appears essentially continuous in relatively flat lying areas and spotty to completely absent in areas with any slope. The site is currently in use as rangeland for cattle (Figure 14). Two wells are located on the site were installed by the United States Geological Survey for hydrologic research in connection with the Arbuckle-Simpson Hydrology Study (Figure 15).

Eight ERI datasets were collected at the site (Table 1). Three were collected to assist with finding a location for the research wells on the site (Figure 14) and five were collected to assist in characterizing the epikarst at the site (Figure 15).

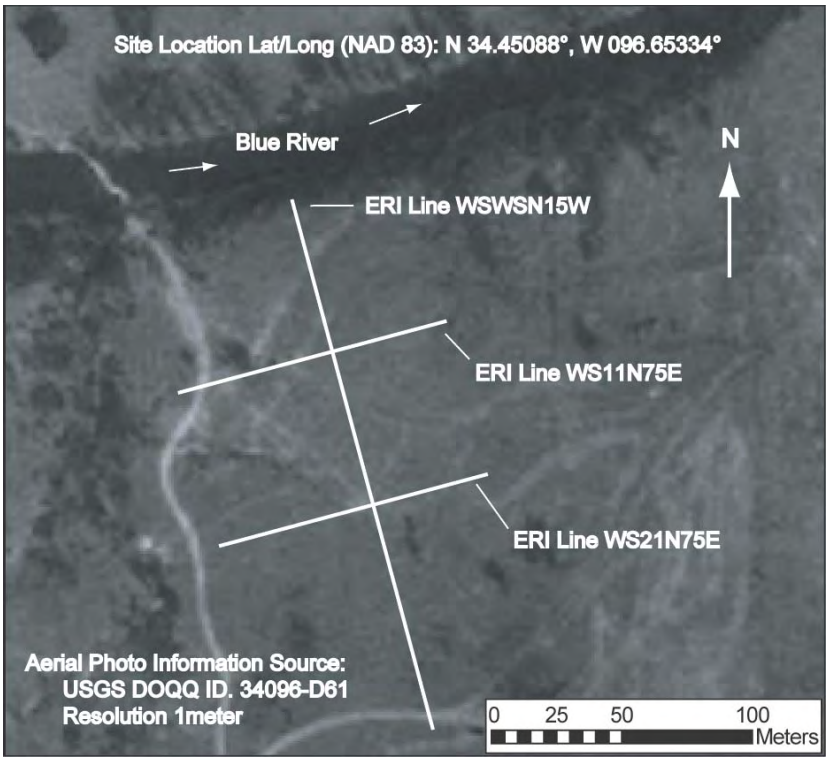

Figure 14. Spears Ranch site map with surface electrical resistivity locations. Aerial photo courtesy of USGS.

Figure 15. Spears Ranch site map with surface electrical resistivity and direct push locations and well locations (from Sample, 2008). Aerial photo courtesy of Mapquest.

4.9 Unimin Quarry

The Unimin Quarry is located three miles west of Troy, Oklahoma. The quarry mines the Butterly and Royer Dolomite in the area of investigation. The investigation was performed to evaluate the lithological response of the dolomite using the ERI technique. The site was the quarry floor at the time of the study. Two ERI lines were collected on the site (Table 1). Both were difficult to collect as the dolomite was dry and needed to be drilled to accommodate electrodes.

Figure 16. Unimin Quarry Site with location of surface electrode placement. Aerial photo courtesy of USGS.

4.10 US Silica Quarry

The US Silica Quarry is located five miles north of Mill Creek, Oklahoma. The quarry mines the Oil Creek and Joins formation of the Simpson. The investigation at this site was performed to evaluate the electrical properties of the Simpson in the area. The site was the quarry floor at the time of the investigation. Four ERI lines were collected as part of the investigation (Table 1). The site was not as difficult to work in as most bedrock sites due to the moisture content and friability of the sandstone.

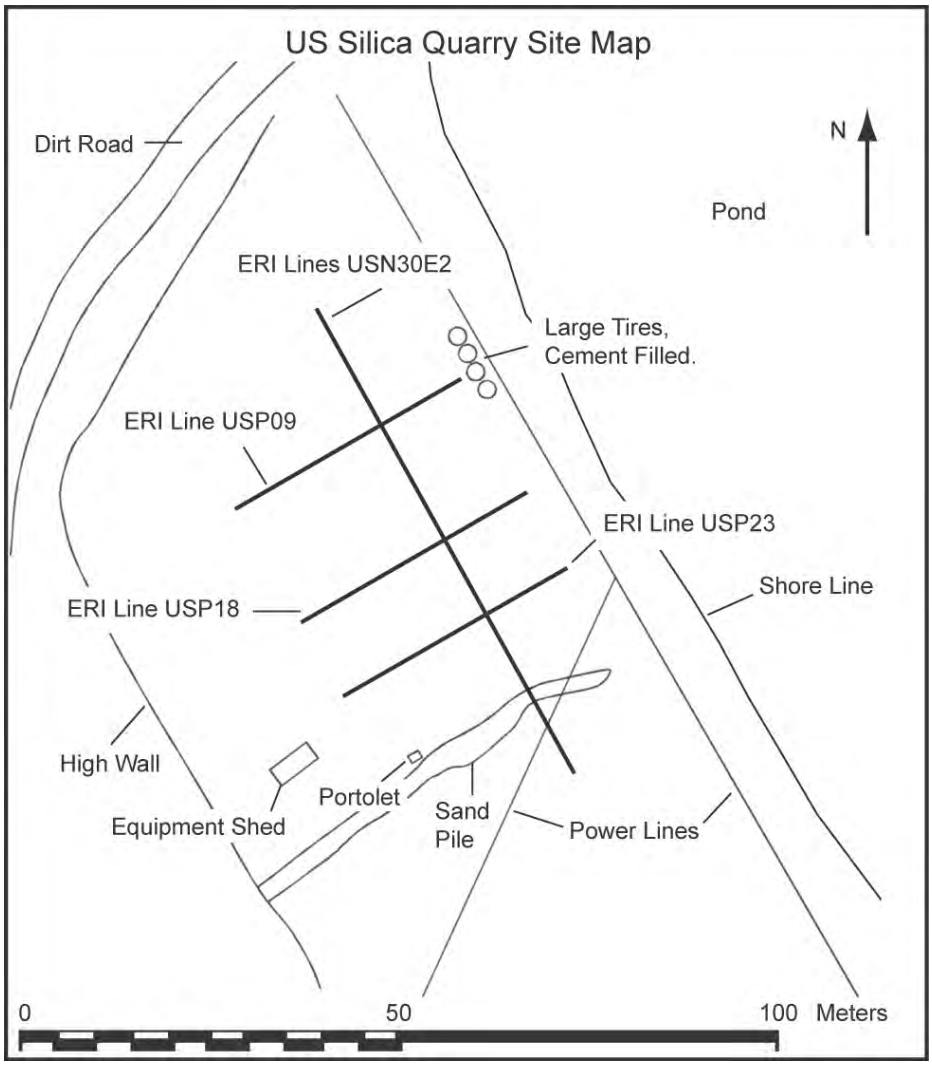

Figure 17. U.S. Silica Quarry Site with location of surface electrode placement.

4.11 Vendome Well

Vendome well is located in the center of the town of Sulphur, Oklahoma. The site is actually the location of two wells, the original which sat in the area where a pool and discharge pipe are located and a new well located immediately to the west. The site overlies the conglomerate of the Vanoss Group. A single ERI line was collected on the site heading from Rock Creek with the well located near the center of the line. Significant details on the geology and construction of Vendome well are provided in Nord (Nord, 1996).

Figure 18. Vendome Well Site with location of surface electrode placement and wells. Aerial photo courtesy of USGS.

4.12 Watson/Sulphur Fault

The Watson/Sulphur Fault site is located 4 miles east of Sulphur, OK. The site is located over the Sulphur Fault and has West Spring Creek rocks of the Arbuckle Group north of the fault and Bromide Formation of the Simpson Group south of the fault. A single ERI line was collected on the site (Table 1).

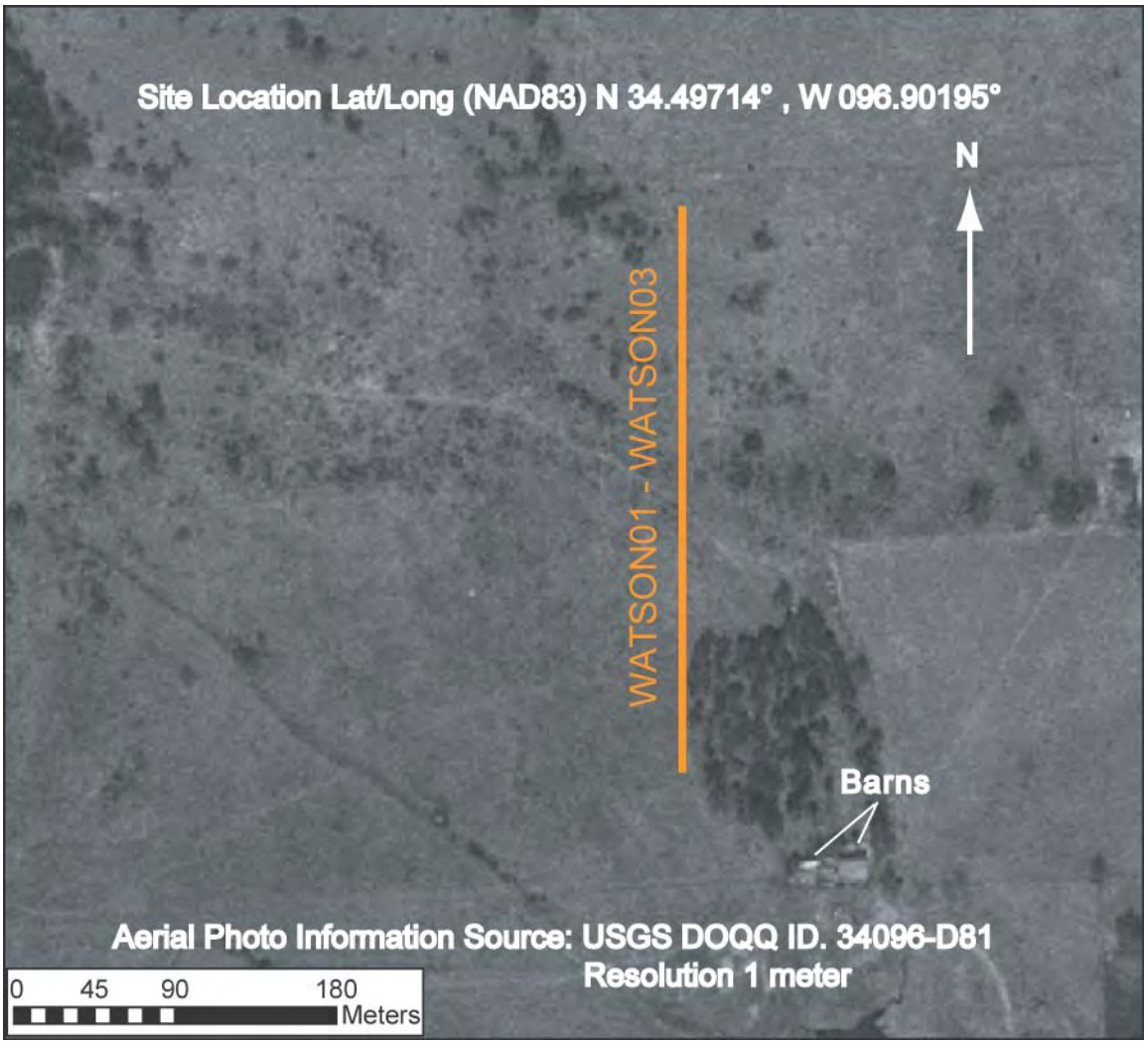

Figure 19. Watson/Sulphur Fault Site with location of surface electrode placement. Aerial photo courtesy of USGS.

4.13 Clay Jack Well

The Clay Jack well site is located 2.5 miles southwest of Hickory, OK. The site is located on the West Spring Creek Formation of the Arbuckle Group. A single BERI experiment was conducted at the site to evaluate the processing of BERI data. Only a single surface/borehole orientation was collected at the site.

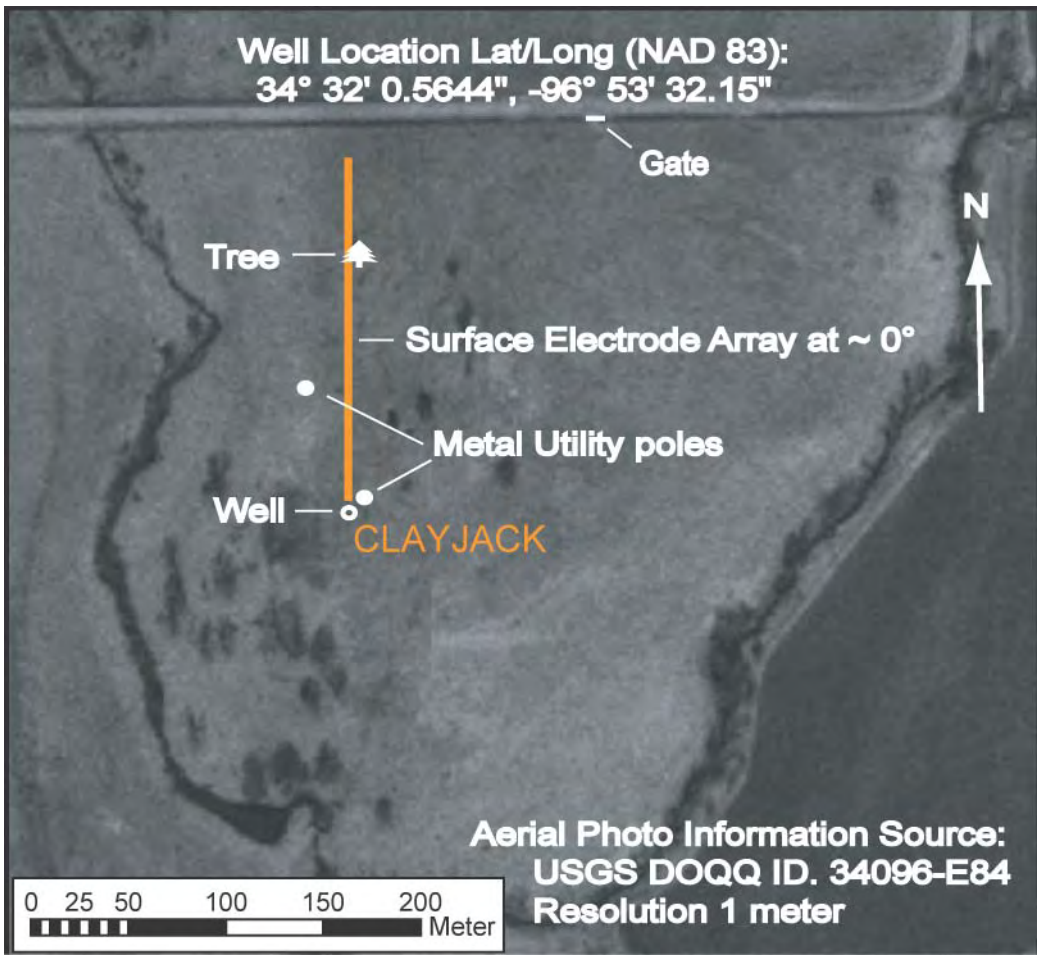

Figure 20. Clay Jack Well Site with location of surface electrode placement and well. Aerial photo courtesy of USGS.

4.14 Wingard 2 Well

The Wingard 2 Well site is located ~ 6 miles ESE of Roff, Oklahoma, 0.8 miles south of E1650 Rd. on N3520 Rd. The legal location for the site is 02N-05E-25, SW ¼. .The gate to the property is on the east side of N3520 Rd. just south of the bridge over Blue River. The well is located ~ 920 ft south of the gate and 140 ft east of the fence line paralleling the road. The well is unused at the present time. A power pole and ground is 7.1 m (23 ft) from the well to the south. The site is relatively level and otherwise free of obstructions for ~ 800 ft in an arc from 0° to 70° from north.

The depth of the well is logged as 2048 feet total depth. The well was found to be partly obstructed at ~66 feet (20 m) below TOC and completely obstructed below ~1300 ft (~400 m). The depth to water was measured at 31.72 feet (9.670 m) TOC. The BERI was temporarily installed in the well. Surveys with the BERI were taken with the top electrode at 225 m (738 ft), 210 m (689 ft), 180 m (591 ft), 150 m (492 ft), 120 m (394 ft), 62 m (203 ft), 47 m (154 ft), 32 m (105 ft), and 17 m (56 ft), below TOC. This would comprise borehole data collected from 56–1001 feet (17-305 m). The electrode spacing for the horizontal surface line was 5.0 m (16.4 ft). The horizontal surface line was rotated about the vertical cable at 0° and 45° (Figure 21). A large bull and a number of cows limited the areas that equipment could be placed without being trampled. The west side of the well could not be surveyed due to a fence and a gravel road. One borehole image and the two surface images were inverted. Data were analyzed for signal quality to a depth of 1001 feet. Due to the well obstructions that made further surveying of the well risky for the equipment, the well was not completely surveyed.

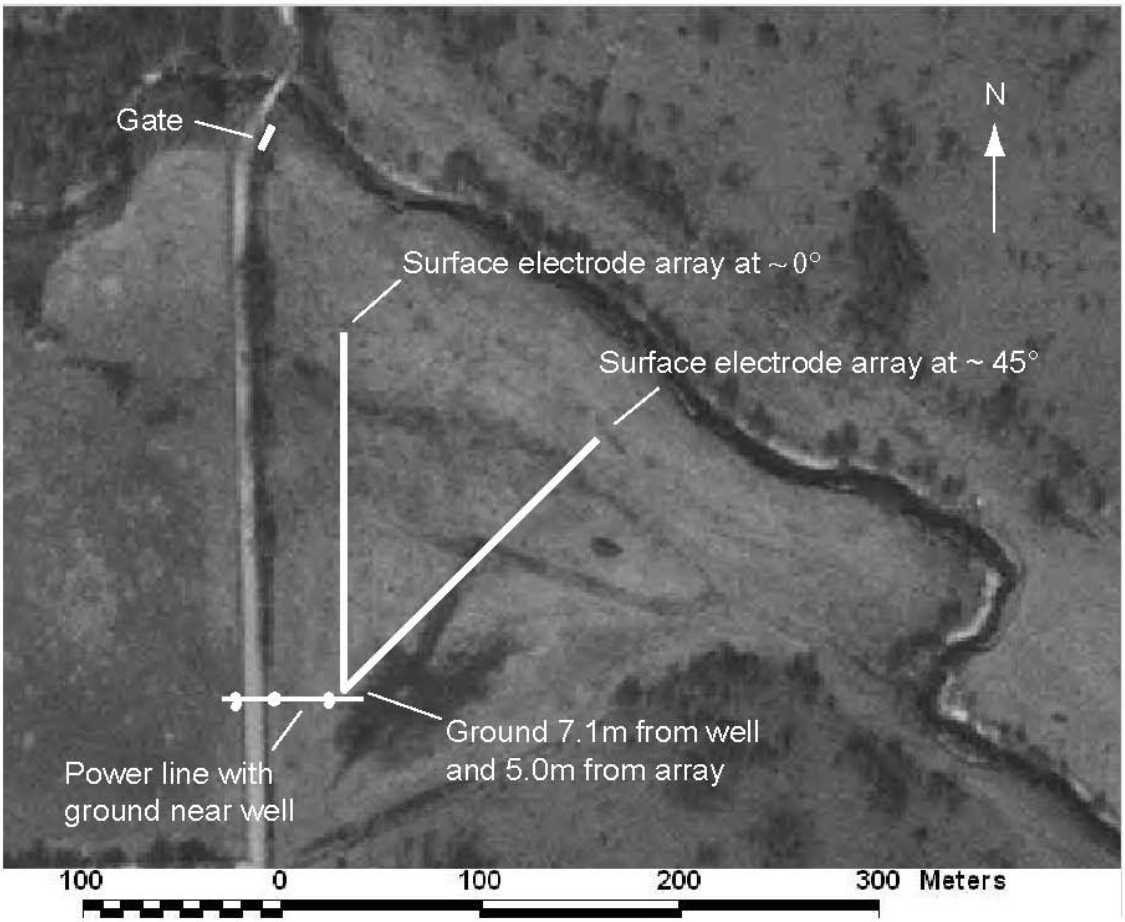

Figure 21. Wingard 2 Well Site with location of surface electrode placement and other line features noted (Halihan et al., 2004). Aerial photo courtesy of USGS.

5.0 Lithology Evaluation

Using quarries and soil-free outcrops where possible, the lithologies of the Arbuckle-Simpson aquifer system were evaluated to determine the electrical properties of the native unfractured formations. This was performed for three formations on exposed bedrock, and one additional formations with soil cover. The lithology is evaluated from the basement upwards through the available formations. The formations that were evaluated are listed in stratigraphic order in Table 2. Other formations were imaged with the technique (See Chapter 4), but they are generally adjacent to fault zones, so interpreting the properties of the lithology absent of tectonic influences and alterations is not possible.

Formation	Location
Oil Creek Sandstone	US Silica Quarry
West Spring Creek Dolomite	Spears Well Site; Fittstown Mesonet
Butterly and Royer Dolomite	Unimin Quarry
Tishomingo Granite	Devil's Den

Table 2. Unfaulted lithologies evaluated using ERI.

5.1 Tishomingo Granite

As expected, the Tishomingo Granite is the most resistive formation evaluated in the study. Resistivities of the unfractured granite are typically above 10,000 ohm-meters and range between 10K and 100K ohm-m. In this range, lithologic features such as fractures and dikes can be observed in the data, but the values are still high resistivity values. Even in the weathered surface area, the resistivity values remain above 10K ohm-meters.

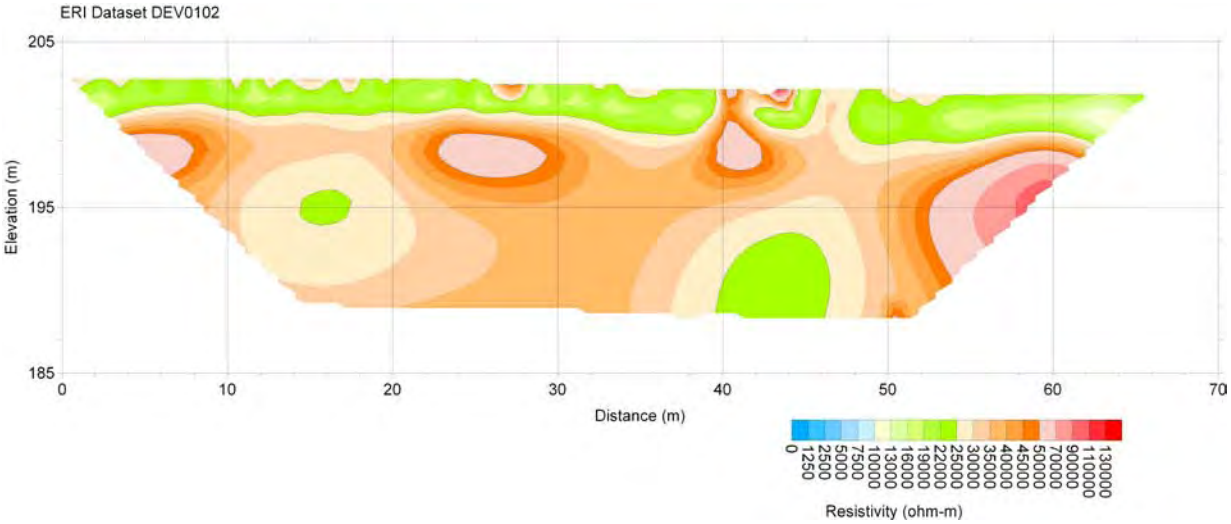

Figure 22. ERI dataset over exposed Tishomingo Granite (from Cemen et al., 2008). Note much higher range in color scheme for the granite.

5.2 Butterly and Royer Dolomite

The unweathered Butterly and Royer Dolomite exposed at the Unimin quarry was also highly resistive. However, the lithology was often more conductive than the granites at Devil's Den. The values observed at the quarry floor were 350 – over 100K ohm-meters. The possible weathered zone in the image at 25 meters lateral distance and a depth o 2 meters indicates that faulting or weathering may change the electrical properties significantly by lowering the values in the weathered or faulted areas.

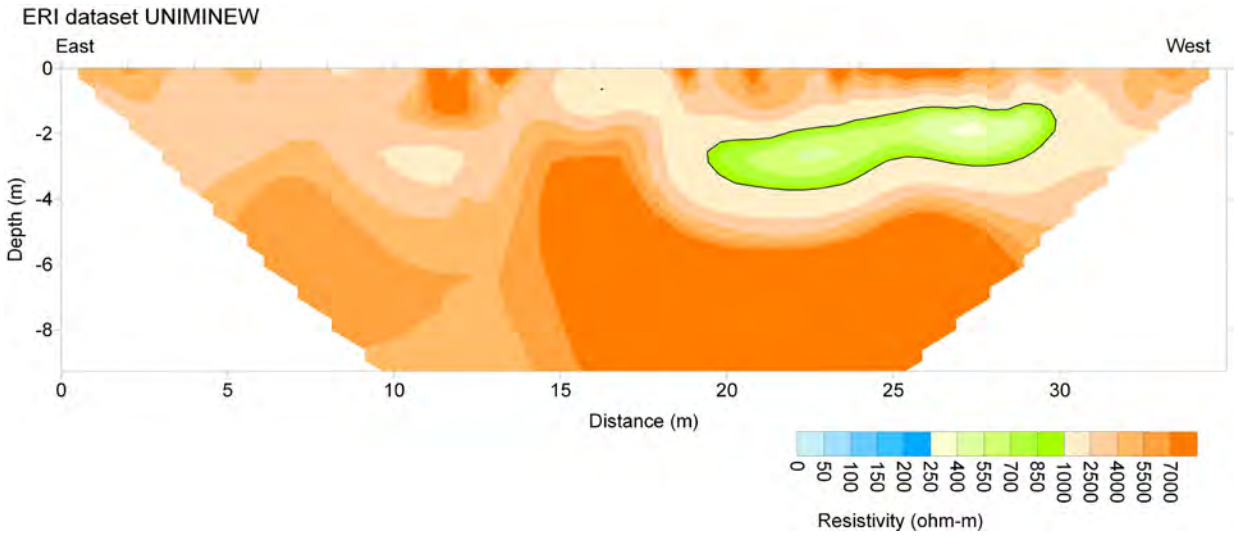

Figure 23. ERI image of the Butterly and Royer Dolomite from the Unimin Quarry floor.

5.3 West Spring Creek Dolomite

Although a quarry image of the West Spring Creek Dolomite is not available, several images were collected over this formation, so they will be discussed for lithologic properties. Below the weathered epikarst zone, the formation is more conductive than the other formations. The formation can have unweathered resistive properties, but can also be quite conductive at depth ranging from 40-1000 ohm-meters at the Spears Well Site (Figure 24). At the Fittstown Mesonet site, the conductive nature and high variability of the formation is similar with values ranging from 70-14,000 ohm-meters (Figure 25). As these locations are not at quarries, they are more weathered locations than quarries, but the data indicate that the formation is generally more conductive than the granites or the Butterly and Royer Dolomite.

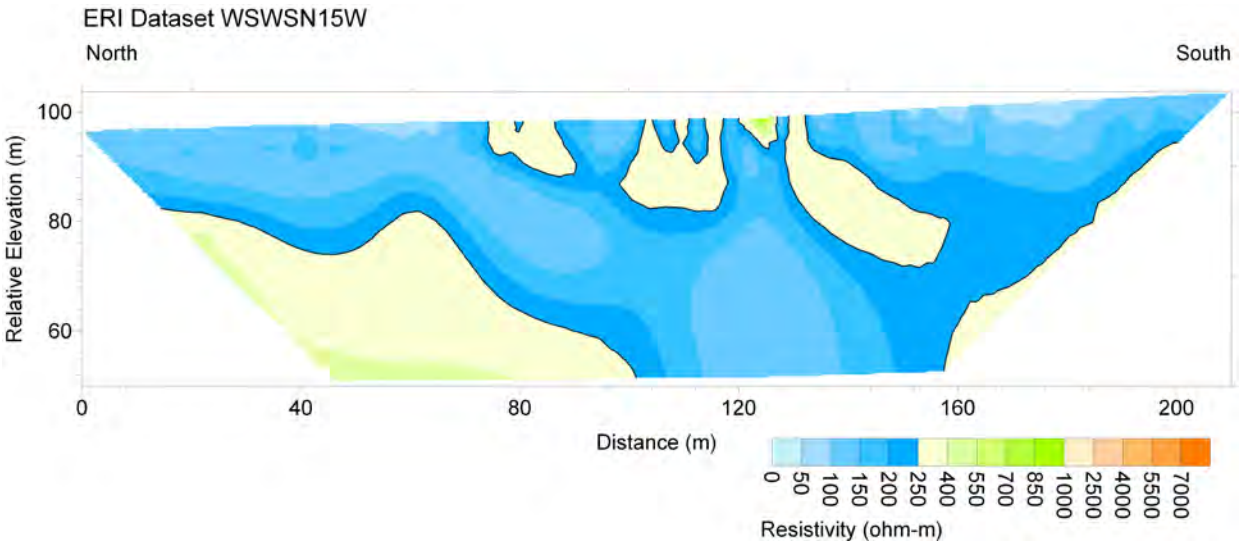

Figure 24. ERI dataset at Spears Ranch site over the West Spring Creek Dolomite.

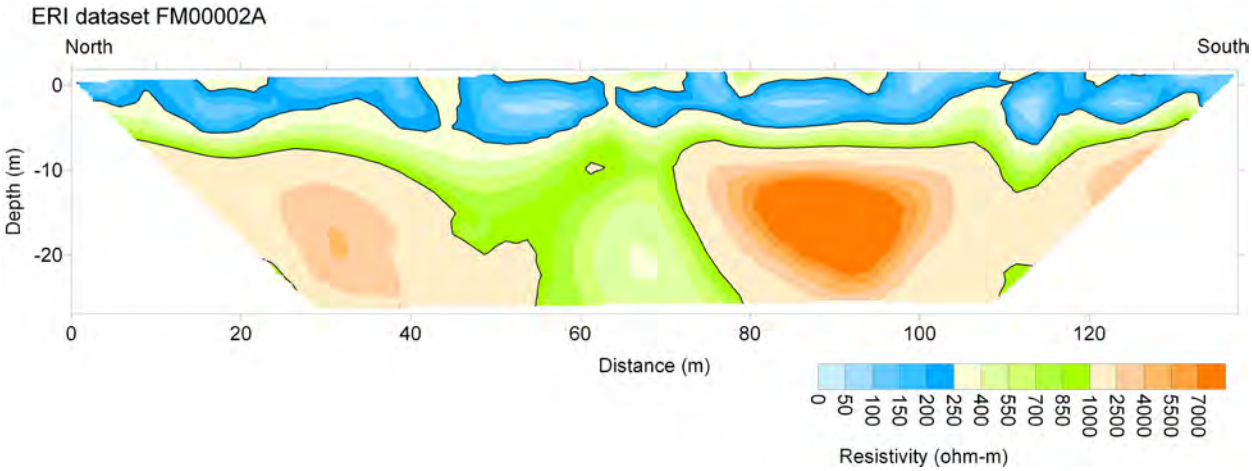

Figure 25. ERI dataset at the Fittstown Mesonet site over the West Spring Creek Dolomite.

5.4 Oil Creek Sandstone

The Oil Creek Sandstone is the most conductive bedrock formation imaged. At the floor of the quarry, the water table was only a meter below the surface, and the increasing conductivity of the formation due to water saturation is evident in the ERI data. The formation ranged from 250-1000 ohm-meters when dry and 50-250 ohm-meters when wet. Additional data was not available to cleanly delineate the boundary between the wet and dry formation.

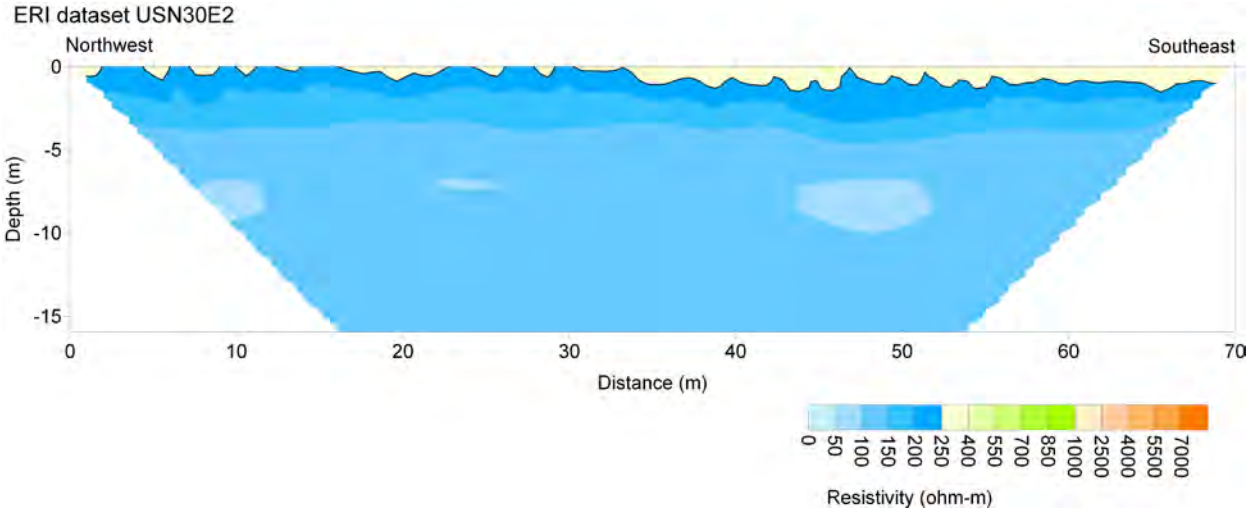

Figure 26. ERI dataset at the US Silica Quarry over the Oil Creek Sandstone.

6.0 Epikarst Evaluation

OSU was tasked by OWRB to characterize the epikarst zone of the Arbuckle-Simpson Aquifer over the Hunton Anticline in terms of its thickness and the hydraulic properties of hydraulic conductivity and storativity. Michael Sample took on this task as part of his Master's thesis (Sample, 2008). Three field sites, the Hatch, Spears Ranch, and Arbuckle-Simpson Ranch sites, were selected for the project which provided a sampling of the diverse range of environments found across the Hunton Anticline. The field methods used to collect the data for the study were static water level measurements, direct push sediment cores and electrical conductivity logs, surface electrical resistivity imaging surveys, and concentric cylinder infiltration tests. The field data were collected between September 2006 and July 2007. Laboratory analyses of the field data included porosity and particle size distribution analyses of the direct push sediment cores.

6.1 Epikarst

The uppermost weathered layer of carbonate (limestone or dolomite) rock of fractured karst aquifers that lies beneath the lands surface and any mantling of soil but above the phreatic zone is called the epikarst zone (Klimchouk, 2004; Williams, 1983) (Figure 27). The epikarst zone is recognized as an important part of fractured karst aquifers for recharge and storage (Klimchouk, 2004; Perrin et al., 2003; Williams, 1983). It has been suggested that storage in the epikarst zone can be greater than storage in the underlying saturated zone (Perrin et al., 2003). Understanding the thickness and hydraulic properties of the epikarst zone is important for quantifying the hydrologic budget of fractured karst aquifers which is required for the proper management of regional water resources.

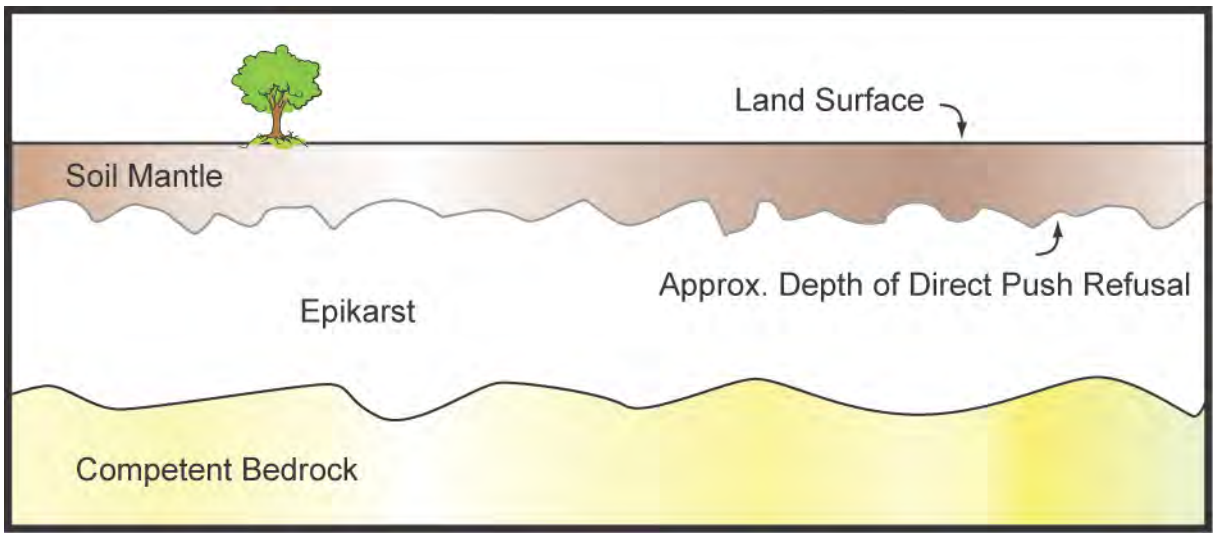

Figure 27. Schematic diagram and terms associated with Epikarst.

6.2 Epikarst thickness

The thickness of the epikarst zone can be highly variable (Klimchouk, 2004) and has been reported as ranging between a few meters to more than 160 meters thick (Bosak and Benes, 2003). Epikarst zones are most commonly reported as less than fifteen meters thick (Klimchouk, 2004). The formation of epikarst is dependent on several environmental factors like climate, micro-climate, local topography, the composition, structure, and texture of the parent rock, and time (Klimchouk, 2004).

The formation of the soils mantling the epikarst is controlled by the same factors (Soil Survey Division Staff, 1993). Soils forming in far removed areas with similar environmental factors will develop with similar physical and chemical characteristics which are used as the basis used for classifying soil types (Soil Survey Division Staff, 1993). The soil types potentially present at the field sites were identified from the 'sa_miads_soils' layer in the OWRB GIS dataset. The specific MIADS soil types sampled by the sediment cores were identified by comparing the results of textural analysis of the sediment core material against the properties of the potential MIADS soils as defined in the NRCS Soil Survey database (Soil Survey Division Staff, 2005). The MIADS soils with properties most closely matching the cored sediments were selected as the soil types sampled by the sediment cores. There are 315 MIADS soils in the study area. The frequency distribution of the MIADS soils ranges between 0.001% and 4.107% with an average frequency of 0.317%.

The approximate thickness of the soil mantling the epikarst was defined as the average of the final direct push probing depths (depth of refusal) within each of the MIADS soil types represented at the field sites (Table 3). The average depths of refusal of the identified MIADS soils were compared against the typical thicknesses of the soils as defined in the NRCS Soil Survey database (Soil Survey Division Staff, 2005). The comparison was done in order to determine whether it would be reasonable to use the soil thicknesses in the NRCS Soil Survey database for the thickness of all of the soils mantling the epikarst over the aquifer. In general the typical thicknesses of the MIADS soils correlates well with the average direct push depths of refusal (Table 3).

The natural variability expected within the epikarst and the soil mantle explains the majority of the observed differences between the direct push refusal depths and the published soil thicknesses. The correlation between the average total direct push depths of refusal and typical thicknesses for the MIADS soils from the NRCS data suggest that it would be reasonable to apply the typical soil thicknesses for all of the MIADS soils over the Hunton Anticline to the problem of defining the thickness of the epikarst.

The observed difference between the published thickness of the Stephenville Fine Sandy Loam and corresponding depths of refusal at the Hatch site appears more significant. Locally intense weathering of the epikarst could potentially account for the observed difference. A local thickening of the soil cover due to anthropogenic causes can not be ruled out due to the long history of agricultural use at the Hatch field site. The core material identified as Stephenville Fine Sandy Loam may also be from a different soil type not identified from the 'sa_miads_soils' layer in the OWRB GIS dataset.

An attempt to determine the approximate thickness of the soil mantling the epikarst was also attempted using the results of the electrical resistivity imaging (ERI) surveys. An ERI image processed from electrical resistivity data collected from the Hatch field site is shown (Figure 28) with the locations of the direct push sediment cores with the final direct push depths of refusal. Two MIADS soils are represented at the Hatch site the Verdigris Silty Clay Loam and the Stephenville Fine Sandy Loam member of the Stephenville-Darnel Complex.

Field Site	MIADS Soil Type	Percent of Area with Soil Type (%)	Average Direct Push Depth of Refusal (ft)	Typical MIADS Soil Type Thickness (ft)	Approximate Average Depth to Bottom of Epikarst (ft)	Approximate Epikarst Zone Thickness (ft)	Epikarst /MIADS Soil Thickness Ratio	Depth to Groundwater Table (ft)
Hatch	Verdigris Silty Clay Loam	2.47	6.5	6.0	45.0	39.0	6.5	79.8
	Stephenville Fine Sandy Loam	0.57	10.1	3.3	45.0	41.7	12.6	79.8
Spears Ranch	Kiti Very Flaggy Silt Loam	3.11	1.4	1.3	15.0	13.7	10.5	25.4
Arbuckle-Simpson Ranch	Gowton Loam	0.14	6.6	5.8	49.0	43.2	7.4	9.0

Table 3. Summary of the Epikarst Thickness Calculations.

The observed electrical resistivity values of the MIADS soils, as constrained by the final depths of refusal, appear to be highly variable in nature but are generally less than 55 ohm-m. The differences between the physical properties of the two MIADS soils appear to be significant enough to be observed in the ERI image (Figure 28). The more conductive feature near the surface at the distance of from around 315 to 510 feet appears to coincide with the presence of the sandy loam and loamy sand characteristic of the Stephenville soil type. The highly variable nature of the electrical resistivity values observed near the surface would make identifying the boundary between the soil mantle and the top of the epikarst zone problematic without the direct observations made possible by the direct push methods.

The depth to the surface of the groundwater table was determined from static water level measurements. The depth to the static water level from the land surface was measured from wells at the Hatch and Spears Ranch sites. The depth to the surface of the groundwater table at the Arbuckle-Simpson Ranch was estimated from the surface water elevation of a pond located at the site (Table 3).

The approximate average depth to the bottom of the epikarst zone at each field site was estimated from the results of the ERI surveys (Table 3). The variability in the electrical properties of the Earth materials in the ERI images from the field sites was observed. A high degree of electrical variability was expected to be observed from the soils and from the highly weathered rocks of the epikarst zone relative to the electrical variability observed from the more competent underlying rock mass.

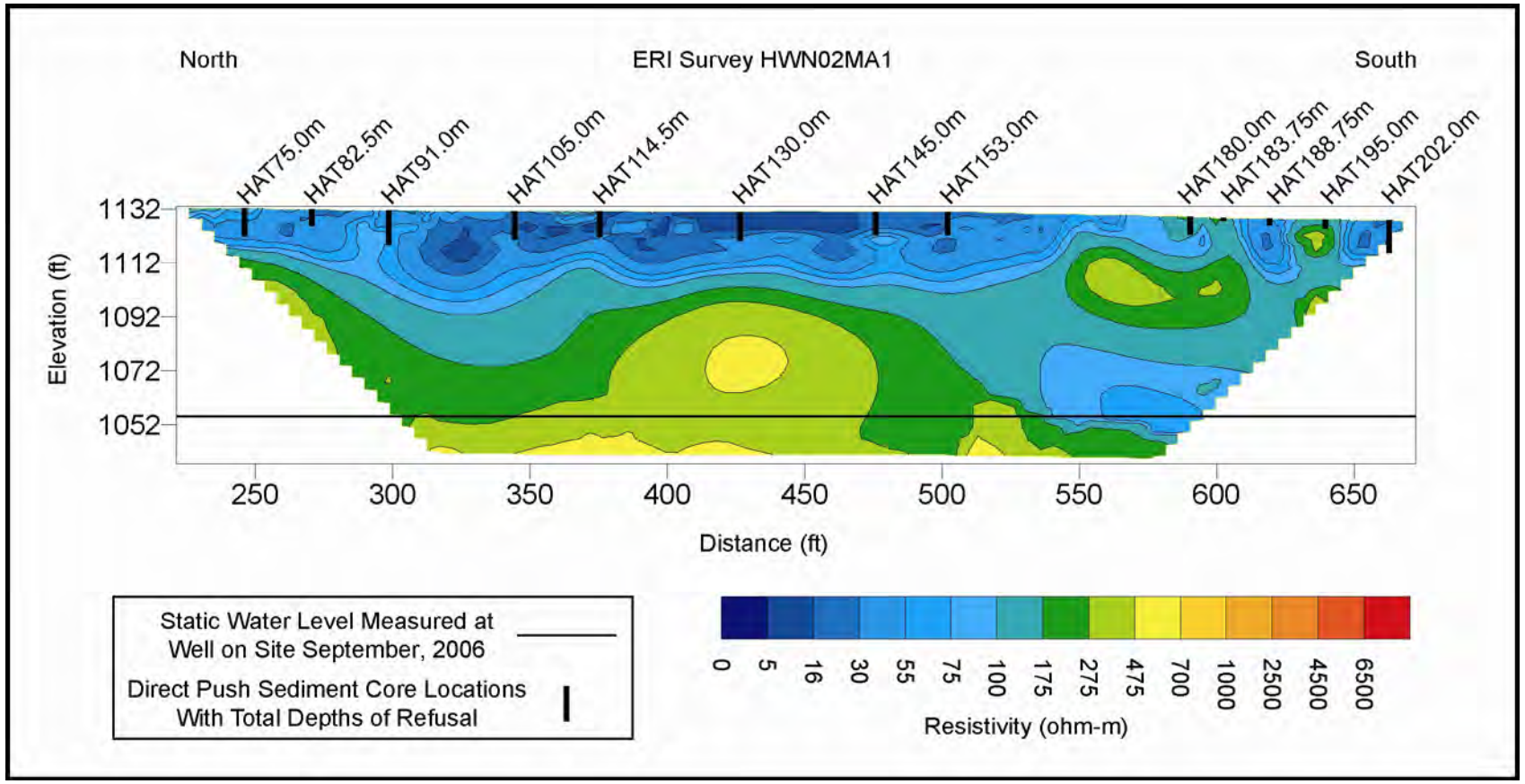

Figure 28. Electrical Resistivity Imaging Results From the Hatch Field Site With Sediment Core Locations.

Electrical resistivity values in the Hatch site ERI image are observed to generally increase with depth (Figure 28). In general the upper ~ 45 feet of the ERI image shows a relatively high degree of electrical variability as compared to the observed electrical variability below that depth. The observed electrical variability appears to be highest near the surface and the degree of electrical variability appears to decrease and become more homogeneous with depth. The zone of relatively high electrical variability appears to vary considerably in thickness across the ERI image. The ERI data from each of the field site show similar electrical features in the shallow subsurface that are consistent with the electrical variability associated with epikarst.

The observed variability in the electrical properties of the subsurface materials is greatly decreased at depth but continues to extend to depths below the indicated static water level (Figure 28). The electrical variability observed extending vertically to the bottom of the ERI image may indicate that weathering processes associated with the epikarst zone may extend into the phreatic zone. The observed electrical variability at depth may also indicate that the water table is lower at the ERI survey location than the static water level measurement at the nearby well indicates. No clear relation appears to exist between the observed electrical resistivity features and the measured static water level at any of the field sites. The approximate thickness of the epikarst zone for the area under each soil type was determined by subtracting the typical thickness of the MIADS soils from the approximate average depth to the bottom of the epikarst zone (Table 3). The results indicate that the epikarst thickness is highly variable across the Hunton Anticline.

Because the formation of the epikarst and the soil mantle are controlled by the same environmental factors it would seem to be reasonable to expect that a relationship might exist between the resulting thicknesses of each. The ratios of the approximate thicknesses of the epikarst zone under each of the soil types versus the MIADS soil thickness were calculated (Table 3). The calculated geometric mean value of the thickness ratios is 9.0, indicating for a given soil thickness, the epikarst zone would be expected to be nine times larger. In the absence of additional data, it would be reasonable to consider using the geometric mean value of the thickness ratios for the purpose of estimating the epikarst zone thickness under each of the MIADS soils across the Hunton Anticline. As the soil thicknesses in the NRCS soils range from 0.0 to 7.2 feet for the area, the epikarst zone would range from negligible to over 60 feet.

6.3 Hydraulic Conductivity

Hydraulic conductivity, *K* [μm/s], values for the MIADS soils were estimated from the direct concentric cylinder infiltration measurements. Hydraulic conductivity values for the MIADS soils were also calculated empirically from the direct push sediment core porosity and grain size distribution analyses results using the Fair-Hatch (Todd, 1959) and Carmen-Kozeny (Bear, 1972) equations. The Fair-Hatch equation provided K values that more closely approached both the K values estimated from the direct concentric cylinder infiltration measurements and the K ranges established for the MIADS soils in the NRCS Soil Survey database than did the K values calculated using the Carmen-Kozeny equation. Only the hydraulic conductivity results calculated from the Fair-Hatch equation are discussed here.

Hydraulic conductivity profiles were constructed for each sediment core from the results of the Fair-Hatch calculations. The infiltration test results and constructed hydraulic conductivity profiles for each of the MIADS soils at a field site were plotted together along with the typical hydraulic conductivity range for the MIADS soils as defined in the NRCS Soil Survey database (Soil Survey Division Staff, 2005) (Figure 29). The range of soil hydraulic conductivity values listed for the soils in the NRCS soils database is 0.01 – 141.14 μm/s. In addition, some hydraulic conductivity values of 0.0 μm/s are given for urban areas and a few rock bodies in the NRCS soils database. The Combined hydraulic conductivity plots for each of the MIADS soils were analyzed for trends.

Several of the infiltration results fell within the expected range for the identified MIADS soils (Figure 29) but the majority of the infiltration tests produced hydraulic conductivity values that were below the expected range by, on average, one order of magnitude. The sediment core analysis results plotted as hydraulic conductivity profiles show hydraulic conductivity values that are, on average, approximately one order of magnitude lower than the expected hydraulic conductivity range. The hydraulic conductivity values empirically calculated from the sediment core analysis do not have any directional orientation and thus can not be used to say anything specific about vertical anisotropy in the sediments above the epikarst zone. The gaps seen in the hydraulic conductivity profile represents core intervals with no data due to the loss of data (Figure 29). Gaps in the data from the other field sites (not shown) indicate intervals of weathered rock in the sediment cores. The weathered rock intervals were not subjected to porosity and grain size distribution analysis because the methods used for the sediment core analyses were not appropriate for the analysis of rock fragments.

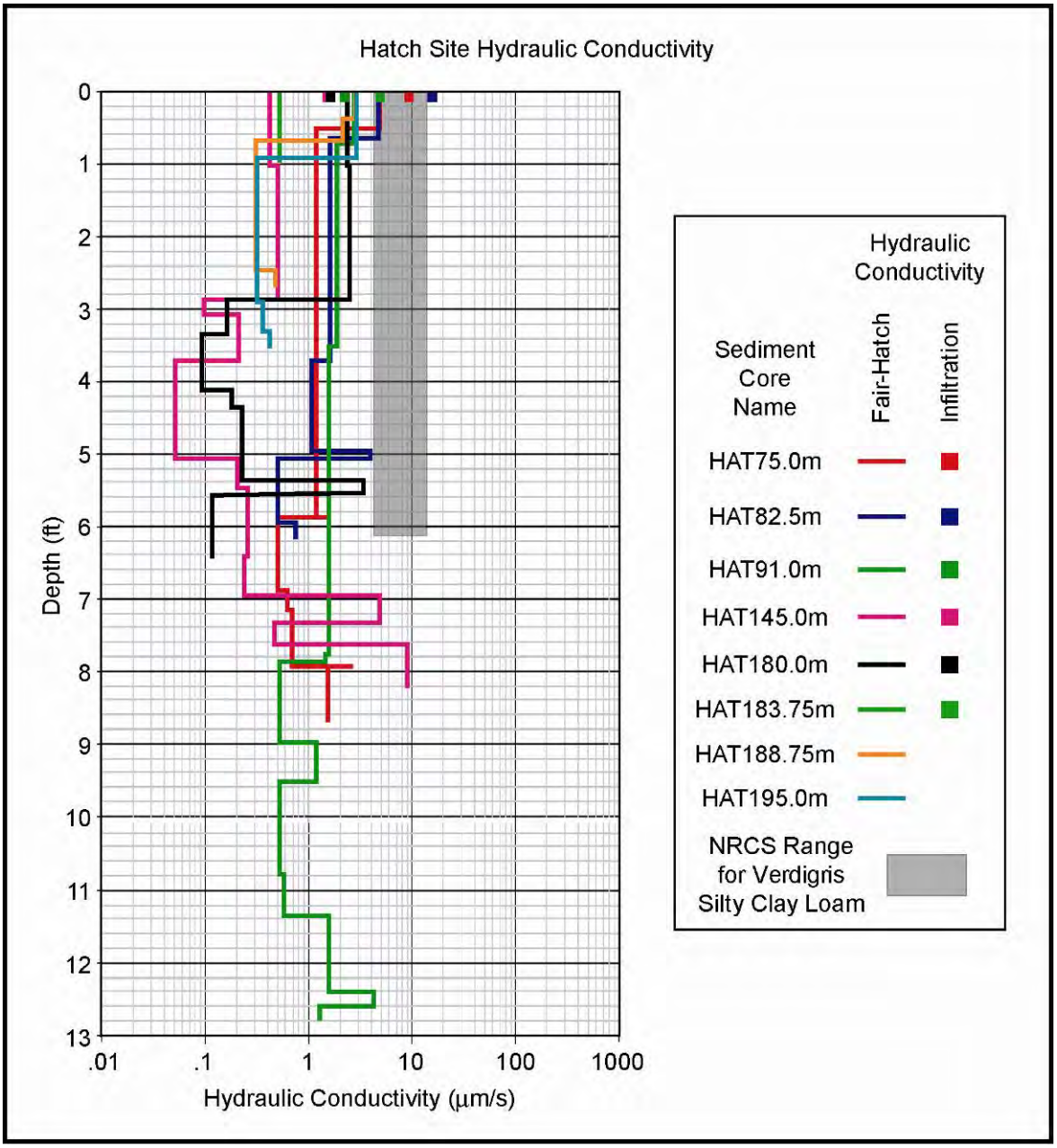

Figure 29. Hydraulic conductivity results corresponding with the Verdigris Silty Clay loam soil type.

Material Type	Material	Hydraulic Conductivity Range (μm/s)
Unconsolidated	Unweathered marine clay	$8 \times 10^{-7} – 2 \times 10^{-3}$
	Clay	$1 \times 10^{-7} – 4.7 \times 10^{-3}$
	Silt, loess	$1 \times 10^{-3} – 20$
	Fine sand	0.2 – 200
	Medium sand	0.9 – 500
	Coarse sand	0.9 – 6000
	Gravel	300 – 30000
	Till	$8 \times 10^{-6} – 2$
Sedimentary rocks	Shale	$1 \times 10^{-7} – 2 \times 10^{-3}$
	Siltstone	$1 \times 10^{-5} – 1.4 \times 10^{-2}$
	Sandstone	$3 \times 10^{-4} – 6$
	Limestone, dolomite	$1 \times 10^{-3} – 6$
	Karst and reef limestone	1 – 20000

Table 4. Hydraulic Conductivity Values of Common Earth Materials (Modified after Weight and Sonderegger, 2001).

The hydraulic conductivity of soils is highly variable and can vary by more than a factor of ten within an area smaller than a square meter (Soil Survey Division Staff, 1993). The replication of hydraulic conductivity measurements (10 to 20 or more) would be required to achieve an adequate statistical distribution to arrive at a mean hydraulic conductivity for an area the size of an average plot (Reynolds et al., 2002b). Hydraulic conductivity measurements are scale dependent and increase with the scale of the measurement regardless of the method used (Rovey and Cherkauer, 1995).

All three field sites are known to have experienced varying levels of anthropogenic disturbance which could have depressed the infiltration results. Erratic changes in the

infiltration rates which can be caused by a high degree of variability in soil properties (Reynolds et al., 2002a) were observed in several of the infiltration tests which affected the interpretation of the infiltration test results. The empirically calculated hydraulic conductivity results generally varied within one order of magnitude for each of the soil types and tended to mirror trends if any seen in the typical hydraulic conductivity ranges for the MIADS soils as defined in the NRCS Soil Survey database. Both the infiltration tests and the sediment core laboratory analyses are very small scale measurements and were not expected to have sampled the full range of hydraulic properties at any of the field sites. All of the calculated hydraulic conductivity values did however fall within the range of values expected for the Earth materials encountered (Table 4). These results suggest that it would be reasonable to use the hydraulic conductivity values from the NRCS Soil Survey database for all of the MIADS soils over the Hunton Anticline.

Much of the sediment core data extends significantly deeper into the subsurface than the corresponding NRCS soils data (Figure 29). The calculated hydraulic conductivity values extending deeper than the NRCS soils data does not differ significantly from the overlying hydraulic conductivity values in any of the constructed hydraulic conductivity profiles. No bedrock was encountered near the bottom of the soil profile In the NRCS data for the Verdigris Silty Loam encountered at the Hatch Site but several direct push depths of refusal occurred close to the bottom of the soil profile which suggests that the hydraulic conductivity data collected from below that point may reflect hydraulic property conditions within the epikarst zone. The NRCS data for other MIADS soils encountered in the field work (not pictured) do indicate that bedrock was encountered near the bottom of the NRCS soil profiles which again suggests that the hydraulic conductivity data collected from below those depths may reflect hydraulic property conditions within the top of the epikarst zone. These results suggest that the hydraulic conductivity values at the top of the epikarst zone are at the same order of magnitude as the overlying soil mantle and that it would be reasonable to apply the hydraulic conductivity values for each of the MIADS soils over the Hunton Anticline to the top of the underlying epikarst zone corresponding to the soils.

6.4 Storage

Storativity, *S* [dim], is a measure of the amount of water that can be stored by an aquifer (Fetter, 2001). Storativity is defined by the equation

$$S = S_y + bS_s \quad \text{(Eq. 1)}$$

where S_y [dim], is the specific yield, S_s [L^{-1}], is the specific storage, and *b* [L], is the saturated thickness of the aquifer. The specific or elastic storage component is a measure of the volume of water that an aquifer will yield from the compression of the aquifer skeleton. The specific storage component in an unconfined aquifer is usually very small compared to the specific yield and can be neglected. When the specific storage component is negligible the storativity is commonly taken as equal to the specific yield. For the purpose of this study the storativity of each of the MIADS soils mantling the epikarst was taken as equal to the average calculated total porosity for the individual soils from this study (Table 5). The average total porosities were multiplied by the typical thicknesses of the MIADS soils to provide an estimate of the storage potential in the soil mantle (Table 5). The storage potential would be roughly equivalent to the depth of a lake storing the water in that zone, and ranges from 0.55-2.7 feet for the soils studied.

The storativity of the bulk rock mass of the Arbuckle-Simpson Aquifer has been estimated as 0.002-0.014 (Christenson et al., 2007) (Table 5). The average saturated thickness of the Arbuckle-Simpson aquifer has been estimated as 3000 feet. (Table 5). The storage potential for the saturated thickness of the aquifer was estimated by multiplying the storativity of the bulk rock mass of the Arbuckle-Simpson Aquifer by the average saturated thickness. The storage potential for the saturated thickness of the aquifer was estimated as approximately 6 - 42 feet (Table 5).

The storativity of the epikarst zone has been estimated as 0.05 as a conservative estimate. This would be an order of magnitude above the storativity estimate of the primary aquifer. We know of no studies that quantified this value better than estimating it as 1-2 order of magnitude higher than the bedrock. Additionally, as a conservative estimate, it is an order of magnitude below the storage in the soil zone. The storage potential for the approximate average epikarst zone was estimated by multiplying the storativity of the epikarst zone by the approximate average epikarst zone thickness for each MIADS soil (Table 5). The results suggest that the potential for groundwater storage in the epikarst zone is significant.

Using conservative estimates for storage in the soil and epikarst domains, the total storage in these areas is conservatively estimated to be the same order of magnitude as the entire remainder of the aquifer. The true values may be 2-5 times higher depending on the variability of determining storage in the epikarst zone. This would make the shallow storage zones similar to the aquifer storage parameters and can significantly influence modeling of the aquifer on small scale evaluations of recharge and for contaminant transport. There does not appear to be a significant amount of available water stored in the pore space of the epikarst zone in the areas that were investigated based on previous drilling in the area. Additionally, imaging of several areas indicates conductive areas may be clay dominated and not necessarily indicative of high flow areas of the aquifer.

6.5 Epikarst Conclusions

Three sites were intensively investigated to evaluate the thickness, conductivity, and storage properties of the mantled epikarst of the Arbuckle-Simpson aquifer. The results indicate that the soil thicknesses available from the MIADS database correlate with the thicknesses derived from direct push depth of refusal. The results also indicate that the epikarst zone is approximately 9 times larger than the soil zone. The hydraulic conductivity of these areas is similar to the expected value for the materials present, but the analysis used resulted in values that were smaller than larger field scale measurements. Finally, the storage potential of the mantled epikarst region appears to be the same order of magnitude as storage in the aquifer. This may influence recharge and contaminant transport at the site scale in the Arbuckle-Simpson aquifer.

Field Site	MIADS Soil Type	Typical Thickness of MIADS Soils (ft)	Average Porosity of Soils (dim)	Storage Potential of Soils (ft)	Average Epikarst Zone Thickness (ft)	Estimated Storativity of Epikarst (dim)	Storage Potential of Epikarst (ft)	Storage Potential of Mantled Epikarst (ft)
Hatch	Verdigris Silty Clay Loam	6.0	0.45	2.7	39.0	0.05	2	5
	Stephenville Fine Sandy Loam	3.3	0.46	1.5	41.7	0.05	2	4
Spears Ranch	Kiti Very Flaggy Silt Loam	1.3	0.42	0.55	13.7	0.05	0.7	1
Arbuckle-Simpson Ranch	Gowton Loam	5.8	0.35	2.0	43.2	0.05	2	4
							Approximate Arbuckle-Simpson Aquifer Thickness (ft)	3000
							Approximate Arbuckle-Simpson Aquifer Storativity (dim)	0.002 - 0.014
							Approximate Arbuckle-Simpson Aquifer Storage Potential (ft)	6 - 42

Table 5. Storage Property Estimates for various components of the Arbuckle-Simpson aquifer.

7.0 Fault Orientation

This study is related to a study that was done previously to determine the fault properties in the area with gravity surveys, but will use electrical resistivity imaging (ERI) to investigate the faults. The full study is available as a Master's thesis from Oklahoma State University (Riley, 2007). The data from the gravity surveys is compared to the ERI data collected in this study.

7.1 Introduction

The Arbuckle-Simpson aquifer is a sole source aquifer comprised of fractured carbonates and sandstone in south central Oklahoma. The aquifer underlies an area of approximately 500 mi^2 in the area of the Arbuckle Mountains (Fairchild et al., 1990). The aquifer is a source of many major springs and artesian wells in the area including Vendome Well in the Chickasaw National Recreation Area. A study is currently underway to determine if the removal of additional ground water from this aquifer will affect the surrounding springs and surface water supply. To help determine the properties of this tectonically deformed and fractured aquifer, an investigation of the role that faults play in fluid flow is required.

Faults in the area were primarily mapped during the 1950's to the 1970's (Fairchild et al., 1990; Ham, 1969). These faults were mapped using aerial photography and by field study of the formations. Little is known about faults properties at depth, therefore, a cost effective method of determine the fault properties needs to be developed. The properties of the faults that need to be defined are:

1. The dip of the faults.
2. The fluid properties of the fault as a barrier or conduit to flow.

7.1.1 Goals and Objectives

A combination of modeled data and field data from several sites were used in this study to determine the effectiveness of this technique in determining the properties of faults. To test if this system could define the boundaries of faults, a multi-step approach was used. First, forward modeling was done to determine the effectiveness of ERI data in determining the angle of dip of fault planes (Riley, 2007). This report only presents a summary of the modeling results. Second, field data were collected at three field sites to show repeatability in our ability to resolve the faults. When the terrain permitted, a rotation around the fault was done to help

determine the true dip of the fault. Third, ERI field data were compared with the previously collected gravity surveys.

Several objectives were met for this study; they are as follows:

1. Field Data: Several electrode arrays were used across the sites. These were determined by geographic constraints such as buildings, fences, roads, and property lines. This provided data on the influence of electrode spacing on the resolution of the fault. The amount of data collected was practical given the field constraints that were present.
2. Fault Angle: By rotating the arrays around a fault and knowing the trend of the fault, a calculation of the true dip of the fault should come to approximately the same value regardless of the orientation to the fault to the ERI data line. This was essential in determining the degree to which a fault can be resolved.
3. Data Repeatability: Completing surveys at several sites was necessary to show that the technique can be used to determine the fault angles at more than one site. Three sites were selected for this study, which included one site that was open and allowed for good survey coverage, one site that has an active spring along the fault and one site that has an exposed fault trace that allowed the comparison of the resistivity image to a measured surface fault angle.
4. Comparison with Gravity Data: Comparison of the field data with gravity data was completed to correlate with another geophysical data type. Also a comparison of measured strike and dip of an exposed fault was compared to the field data for one site. This provided a comparison with the field ERI data collected at the site.

7.1.2 Resistivity Measurement of Faults

Two-dimensional multielectrode resistivity has been used since the early 1990's to help determine the location of faults. Griffiths, et al. (1993) used simple computer models to test the ability of a Wenner array to determine the location of a fault in a region of complex geology. This study noted that 25 electrodes spaced at a distance of 50 m could electrically image down to a depth of ~200 m, however it was noted that the lack of data saturation had a negative effect on the ability to image the faults in any detail (Griffiths and Barker, 1993). Borehole surveys were performed that showed that faults can be imaged with good detail. With borehole surveys the fault position and displacement of the fault can be determined on the order of 1-10 m

(Suzuki et al., 2000). This method does not provide enough detailed information about the structure of the faults to identify the properties such as dip. Ground penetrating radar (GPR), seismic reflection and refraction, and resistivity have all been used as an integrated investigative technique (Suzuki et al., 2000). Resistivity has helped to provide a confirmation of the data from other geophysical techniques (Cai et al., 1996; Demanet et al., 2001). Nguyen and others (2005) used a crest line extraction process in gradient images to determine the location of a fault in the European PALEOSIS project. They used a Wenner-alpha array in modeling and data collection. Three models were compiled: a vertical fault, a dipping fault, and a step-like structure. The study identified the locations of the faults to within 1-3 meters however no comparisons to the dipping features and the true dips of the features were made. The study noted that higher contrast ratios increased the location error (Nguyen et al., 2005).

The primary difficulty with determining the properties of faults is the lack of data density that is required to define the location and dip of a fault at depth. Because the resolution of a survey decreases with depth, the array must be setup so that maximum data density is obtained at the site of the fault. Modeling has shown that faults are easier to image with a thin overburden less than the width of the fault zone (Louis et al., 2002).

Resistivity measurements utilize four electrodes to take a single apparent resistivity measurement. When hundreds of measurements are collected with a set of electrodes, the apparent resistivity data can be inverse modeled to determine an estimate of the true resistivity at various locations in the subsurface. This modeling of resistivity data has been more common since the early 1990's with the advent of windows based resistivity software (Loke and Barker, 1996).

All numerical resistivity models rely upon a numerical grid. Most commonly, a rectangular grid is utilized. To accommodate the physics of resistivity measurements, generally, the grid consists of two horizontal grid cells located between each electrode at the surface. Vertically, the resolution of the resistivity data decreases with depth, so a grid multiplier is provided that allows for larger grids with depth. For a 56 electrode array, this provides 112 horizontal grid cells and 13 vertical cells when using a vertical multiplier of 1.1 (Figure 30).

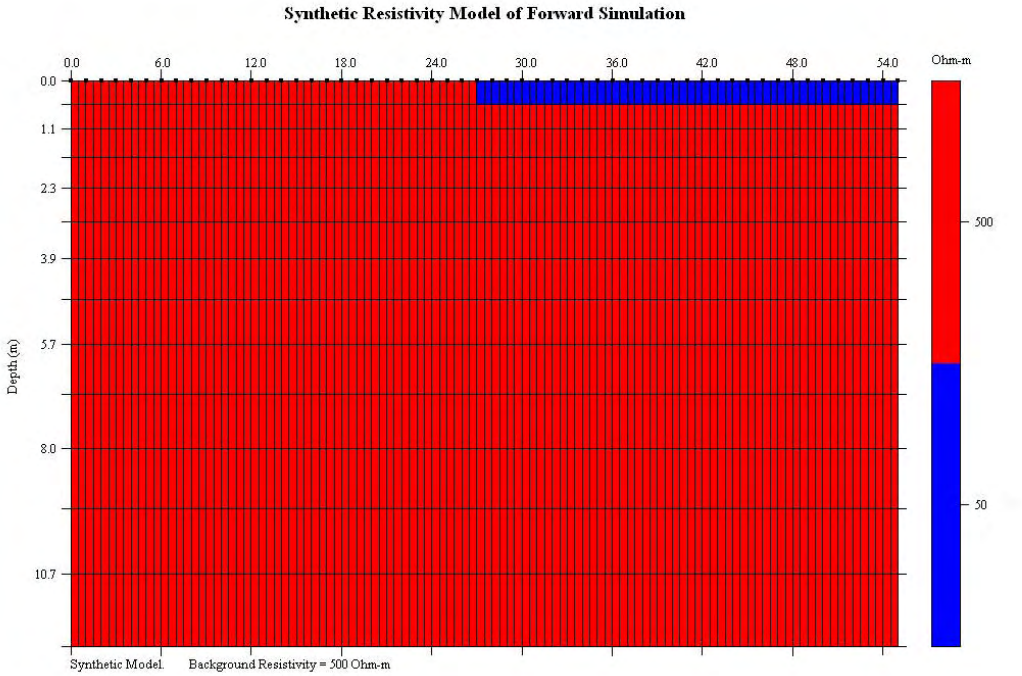

Figure 30. The resistivity imaging grid cell for a 56 electrode array.

The resistivity modeling software can either be used in forward or inverse mode. In inverse model mode, a set of field apparent resistivity data are provided, and the numerical grid is then used to estimate a value of true resistivity at each grid node. In forward model mode, the user inputs a set of values of true resistivity at each grid cell. The model then calculates the apparent resistivity that would be obtained given the defined grid and a specified collection array, such as a Wenner array. The model then utilizes this model set of apparent resistivity data to calculate an inverse model of the true resistivity. This study utilized both forward models to evaluate the ability to resolve dips in ERI images and inverse models to estimate dips in field ERI data.

Due to the nature of surface multielectrode resistivity measurements the data are collected in a set that results in a wedge shaped dataset (Figure 31). This is a result of the ability to resolve boundary conditions outside of this field.

Figure 31. Data field for a standard resistivity survey.

7.1.3 Gravity Data of Arbuckle Simpson Study Area

An extended gravity survey was conducted in the study area over a 20 month period in 2004 and 2005. The purpose of this gravity survey was to determine the dips of the faults in the area. Two methods of survey were conducted. A continuous gravity survey (data collected in real time as a vehicle drove the instrumentation along roads) and a standard stationary discrete gravity survey were completed (Scheirer and Scheirer, 2006). For the purpose of this study the driving survey is used.

7.2 Methods

Two primary methods were utilized in analyzing fault structure in the Arbuckle-Simpson aquifer with ERI data. Forward models of ERI data were performed to determine the resolution of fault features available with current technology. Sources of error were identified and examined to determine the effect they have on the data and to determine how to decrease that effect. These results are summarized in Riley (2007). Field data were collected to compare to the modeled data. The methods used to collect the data were described. The equipment used along with the field methods was described.

Since the focus of this study was to determine fault angles as deeply as possible in the bedrock, it was determined that the maximum electrode spacing possible was required for maximum depth imaging. The following protocol was followed for survey setup:

The field site was visually examined to determine the locations of any major faults on the property, possible obstructions to survey line locations, and the size of the site for an idea on how long the electrode lines could be set up.

After locating the fault, a survey was set up perpendicular to the fault trend. This survey was setup to be as long as possible to image as deep as possible. The following survey

patterns were used; parallel, 30 degrees, and 60 degrees to the fault. This arrangement was designed to observe variations in the dip of the rocks, as the apparent dip should change. The survey layouts were designed to provide the greatest depth penetration along with high enough resolution to image a fault's fractured zone. Since this zone can be large, the largest electrode spacing possible was used. The terrain was also a major consideration in the electrode line layouts.

Since electrode cables were not durable enough to allow vehicles to drive over the line, roads cannot be crossed without traffic control. As a result, the study was limited to sites off of roads that presented no danger to the cables or vehicles. The other limitation was permission from the landowners to access property and limited the surveys to areas within land ownership boundaries.

The surveys also had to cross the fault toward the center of the line for the best resolution at depth. This was the most critical part in designing the surveys and choosing the sites. The key was to find property that had enough open range on both sides of the fault to allow the survey line to extend out for at least 100 meters on either side. The three sites that were chosen were open enough for each of the surveys to fit the criteria.

The final choice in site selection was that the site had to be accompanied by data from gravity surveys that were done on the area in the previous year. This was necessary so that a qualitative comparison between the resistivity and the gravity data could be carried out. This limited data acquisition to the Arbuckle-Simpson study area.

Analysis of the dipping beds in each survey was conducted by:

1. Highlighting the zones of lower resistivity.
2. Picking the edges of these zones and calculating the angle of slope for both edges.
3. Averaging the two slopes.
4. Marking the center of the highlighted area with the average slope.

This allowed for a standardized method of picking the dipping features in the image. By picking the two edges of the zone and averaging them, the error from the inversion should be reduced. Moving the average slope to the middle of the zone is a more accurate representation for the actual location. This is supported by the modeling of the technique (Riley, 2007).

7.3 ERI Field Surveys Results

Field data were collected at three sites and is presented here. Four surveys were completed at the Hartman Fault site with three dipping features identified. Two surveys were completed at the Clement Springs Fault site with three dipping features identified. One survey was completed at the I-35 site; no dipping features were identified.

Several dipping features were identified in the study. The accuracy of these dipping features was determined by error calculations based on the modeling and GPS errors. At the Hartman field site four surveys were run. In those surveys two dipping features were identified. Both originated near the middle of the survey lines. Clement Springs had two surveys run at the site. Three dipping features were identified at this site. Two were on the southern end of the site while one was at the northern end. One survey was run at the I-35 site. No dipping features were identified at this site.

7.3.1 Hartman Site Data

The preliminary images for the two 9 meter surveys were combined and inverted in one file. The result of this file is figure 32. A low resistivity anomaly is evident in the upper part of the image from 100 feet to 400 feet and from 500 feet to 750 feet. Each is about 25 feet thick. Just below these two low resistivity anomalies there are two high resistivity anomalies. After modeling and seeing the effect that a low resistivity anomaly can cause, the high resistivity anomalies at 150 and 610 feet along the line may be abnormally high values. Also note that the zones occur only beneath the low resistivity values. At 400 feet along the line and 100 feet deep there is another low resistivity anomaly that occurs. At 850 feet along the line and 100 feet deep there is a second low resistivity anomaly. At 1200 feet there is an abrupt change in the resistivity values from the north side to the south side. This is a feature dipping at ~50 degrees to the north. On the north side of this fault are rocks of the West Spring Creek / Kindblade formations; on the south side of this zone are rocks of the Deese group. Hand samples were collected along the survey line and analyzed. The composition of these samples supports this conclusion. To the south of the fault zone in the Deese Group there is little change in the relative resistivity of the rocks.

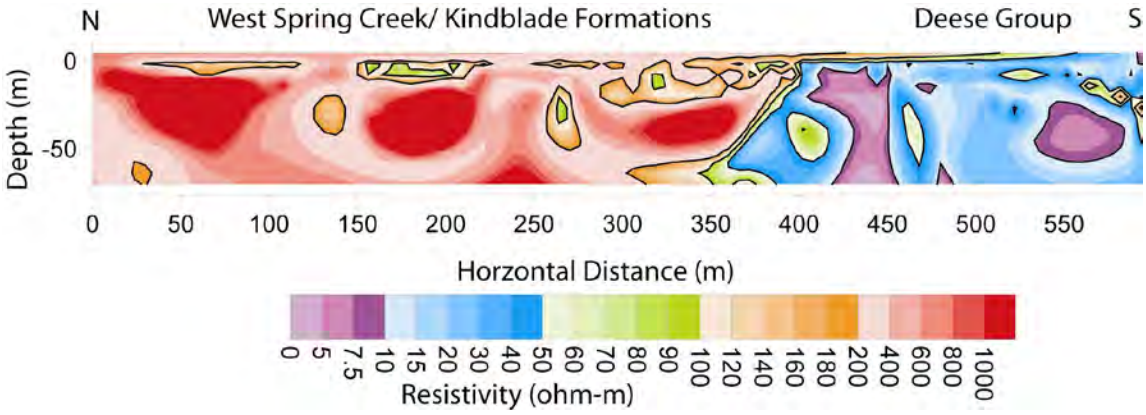

Figure 32. Inverted resistivity section of the preliminary survey done at the Hartman Ranch field site showing the Mill Creek Fault Zone.

Further analysis was completed on this line to identify the major dipping features. Figure 33 shows the low resistivity anomalies identified in the data set. In this analysis, the same dipping feature is analyzed at two different scales. The upper image with feature A is a shorter, 36 electrode, survey. Feature A in this image is dipping at 63 degrees and has a large area that was inverted as the lower resistivity zone. Note that the grid error will be larger in this image due to less grid cells relative to the total line length. Feature B is located on a longer line run along the same location. This line has the feature dipping at an angle of 102 degrees. The fault is interpreted as extending to the surface at this location along the survey line.

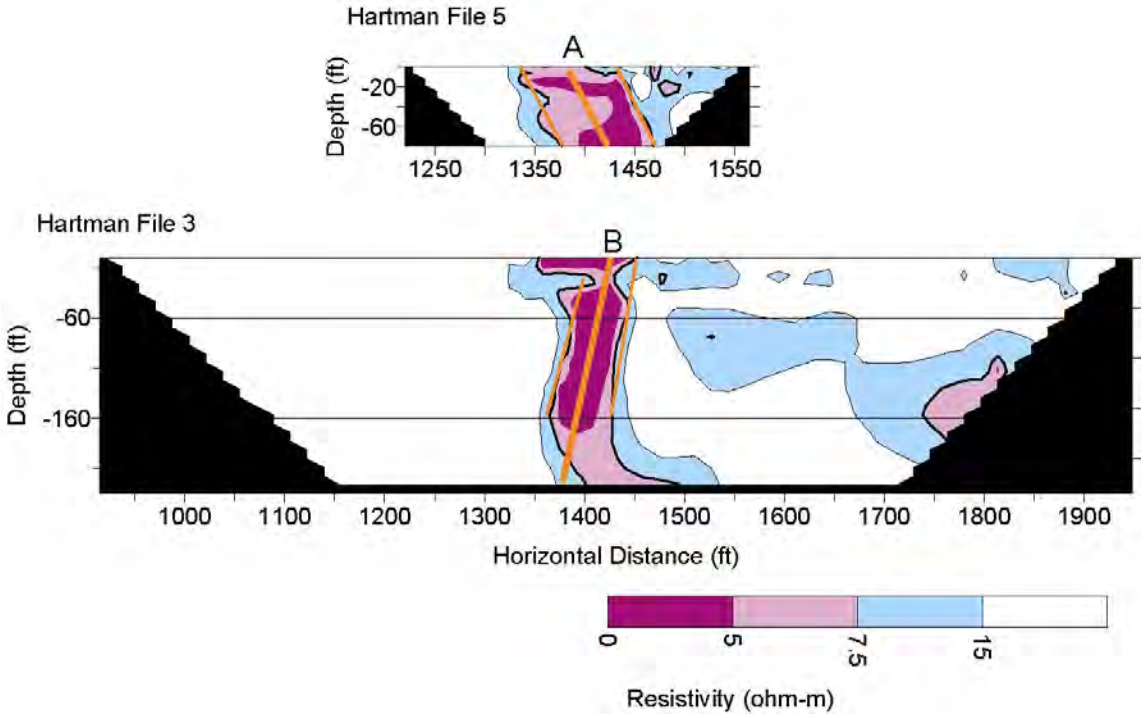

Figure 33. Two surveys taken at the Hartman Field site showing the same dipping feature at two separate scales. The upper image with feature A is a short line that shows the increased dispersion caused from grid error on lines with less electrodes. The lower image contains feature B that is more defined with consistent slopes on both sides of the low resistivity zone.

7.3.1.1 DH01PERP Analysis

On the northern edge of the survey near the surface from 0-100 meters is a lower resistivity signature. From 225 – 300 meters there is another low resistivity. At 340 meters along the upper edge of the survey there is a lower resistivity plane that is dipping to the north – east with an apparent dip of ~45 degrees. At 350 meters there is a near vertical feature of low resistivity. West of the vertical feature is generally higher resistivity than the east side of the feature. The west side of this feature should be rocks of the West Spring Creek/ Kindblade formations and east of the feature are rocks of the Deese Group. Most of the low resistivity trends in the Deese Group seem to have a near vertical trend, which could reflect features associated with the fault (Figure 34).

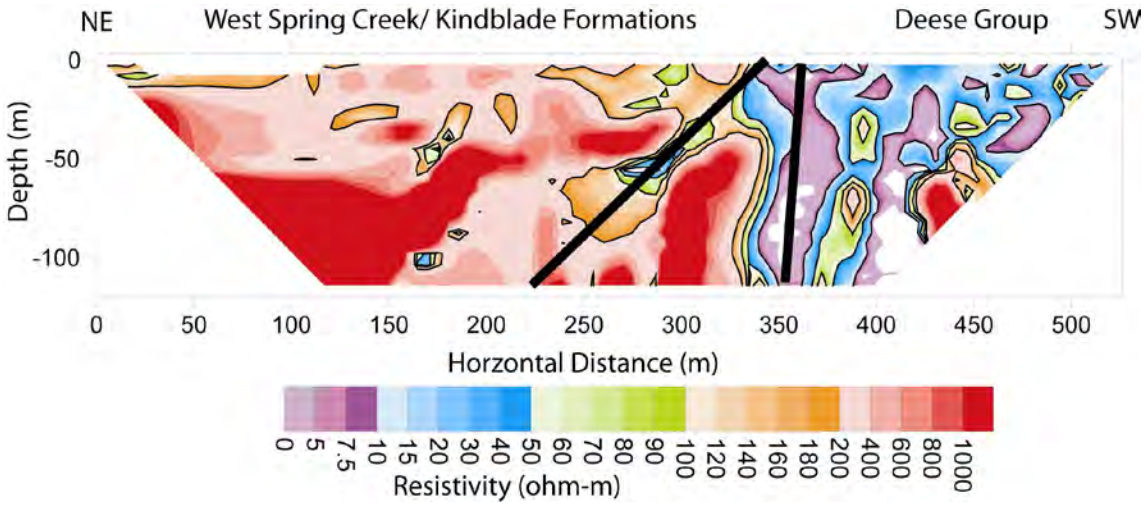

Figure 34. DH01PERP inverted resistivity image showing what appears to be a near vertical fault at 350 meters and a feature dipping at 32 ± 5 degrees at 325 meters.

The analysis was extended on this line to interpret the dipping features. Figure 35 shows three dipping features inferred from resistivity trends present in the data set. Feature A is the shallowest dipping feature interpreted in the low resistivity zone. Feature B is dipping at an angle of 96 degrees. Feature C is dipping at 108 degrees.

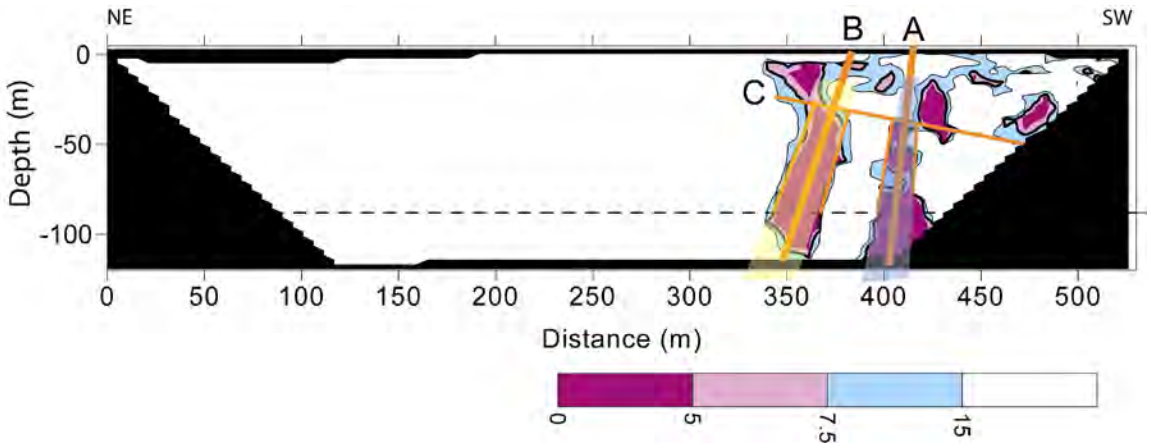

Figure 35. Low resistivity zone highlighted in the DH01PERP line at the Hartman Ranch site. The image shows three dipping features: A, B, and C.

7.3.1.2 DH02N30W Analysis

The second survey conducted at the Hartman ranch was strung with the fault in the middle of the line. To the NW side of the survey are the higher resistivity West Spring Creek / Kindblade formations. At 50 and 100 meters there are two high resistivity zones that occur at around 50 meters in depth. At 150 meters there is a lower resistivity zone. There was evidence at the site that of dissolution features. At 300 meters along the line a dipping lower resistivity plane is present. This plane is dipping at 40 degrees. At 350 meters there is a vertical feature with a sharp contrast in resistivity on each side of the feature. In the Deese group, some horizontal and vertical features are evident (Figure 36).

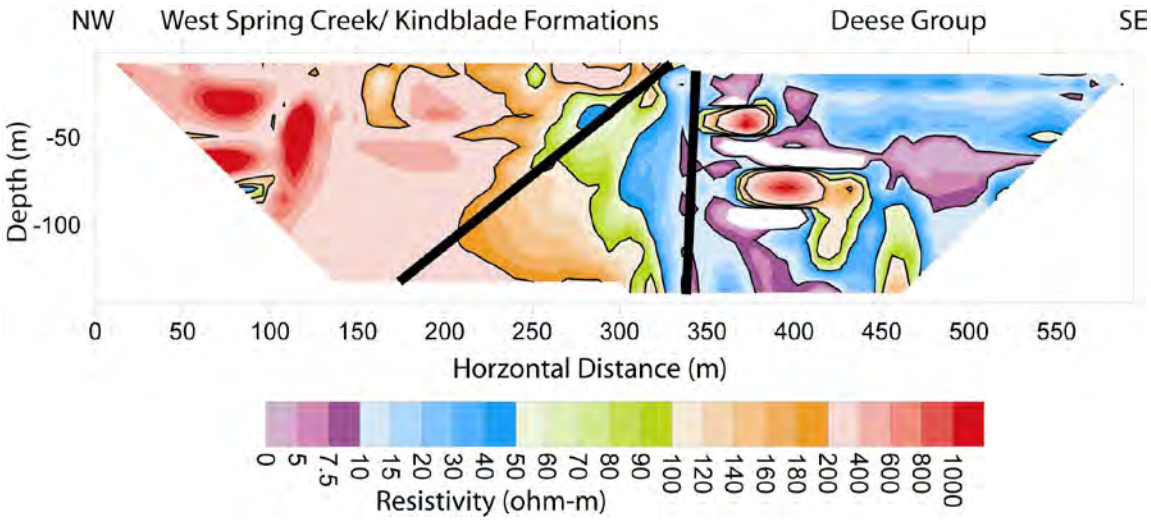

Figure 36. DH02N30W inverted resistivity image showing an interpreted vertical fault and a dipping bed with an apparent dip of 25 ±5 degrees which gives a true dip of 34 degrees at 48 degrees from the fault.

Further analysis was completed on the results of this survey (Figure 37). Three dipping features identified. Feature A in the middle dips at 55 degrees. Feature B is a low resistivity zone with a dip of 93 degrees. Feature C is the shallowest dipping feature at 10.3 degrees.

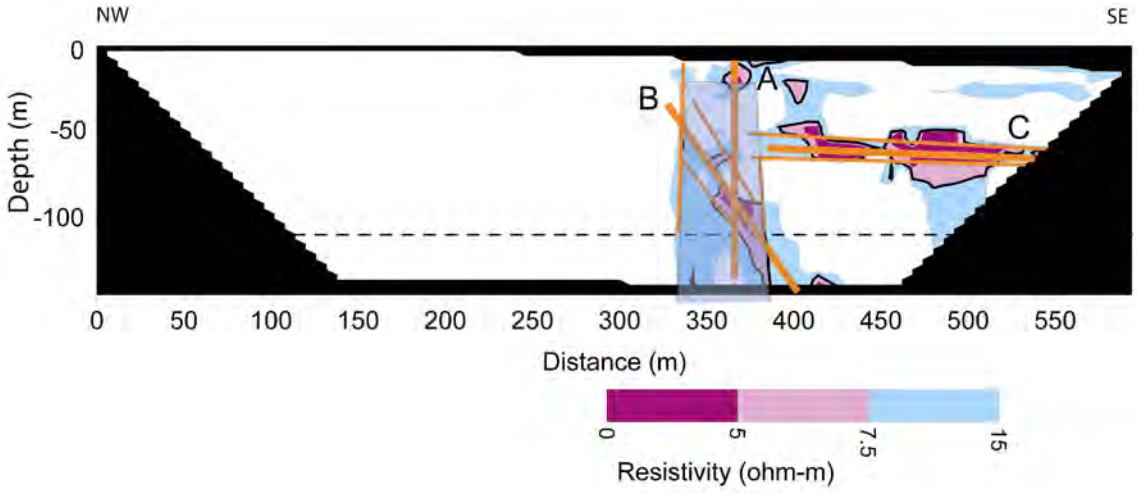

Figure 37. Low resistivity zone of line DH02N30W. Three dipping features were identified in the image.

7.3.1.3 DH03PARA Analysis

The third line at Hartman ranch was also the shortest. In this case only the 36 smart electrodes were used for the survey. The higher resistivity West Spring Creek and Kindblade formation is to the north – west of the 100 meter mark on this survey. There is a plane at 80 meters that dips 30 degrees to the northwest. To the southeast of the fault some low resistivity trends are evident in the Deese group as well. At 120 meters there is a slightly higher resistivity "finger" dipping at about 40 degrees (Figure 38).

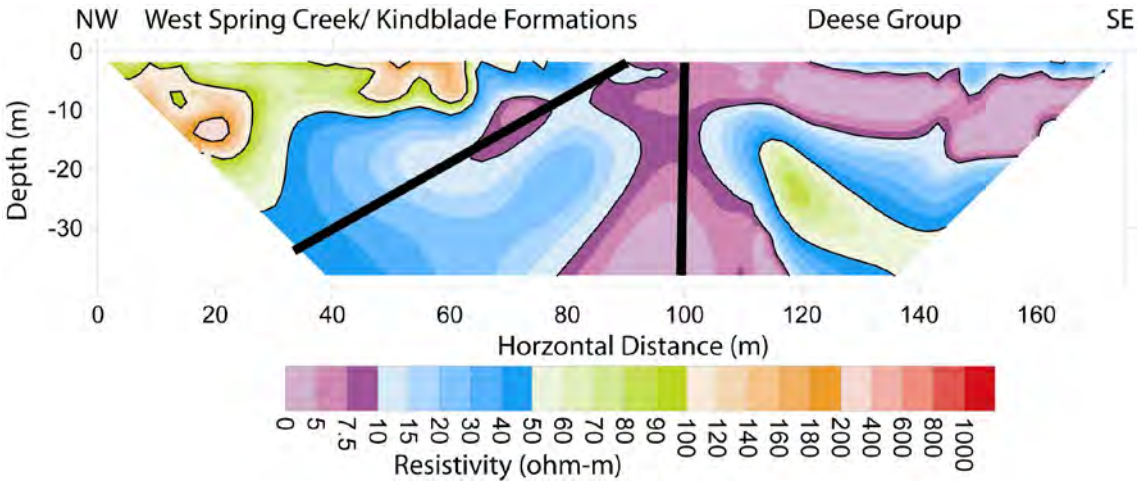

Figure 38. DH03PARA inverted resistivity profile showing a vertical fault and a horizontal bed dipping at 20 ±12 degrees which gives a true dip range of 22 – 61 degrees.

Further analysis was completed on this survey (Figure 39). The analysis showed three dipping features in the image. Feature A which dips at 140 degrees is the middle dipping feature in the image. Feature B is the shallowest dipping feature at 10.3 degrees. Finally, feature C is the steepest dipping angle in the image with a dip of 95 degrees.

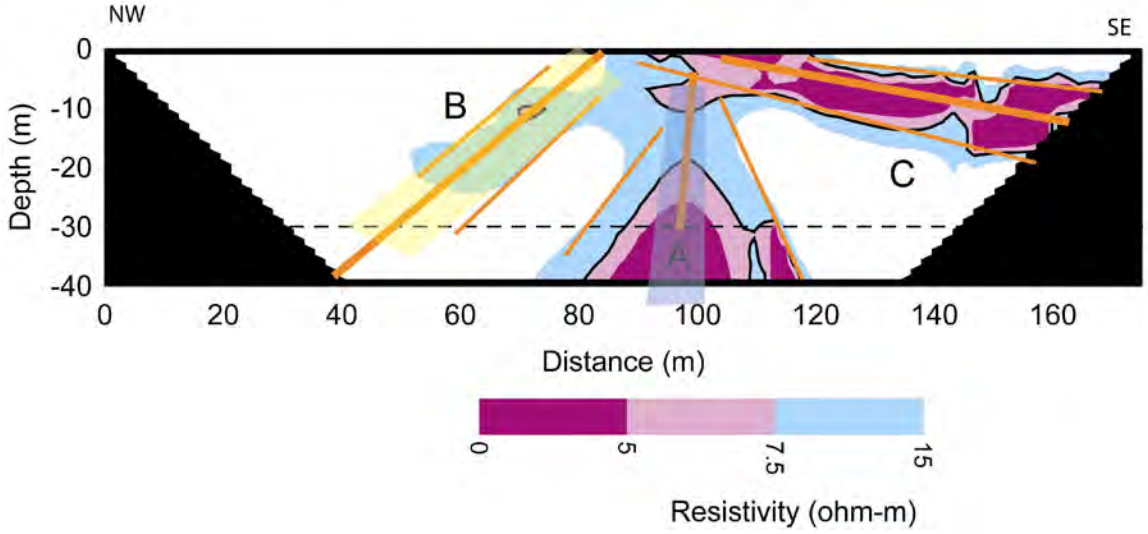

Figure 39. Line DH02PARA at the Hartman Ranch. Three dipping features were identified in the image. The spread is greater from the limited number of electrodes.

7.3.2 Apparent Dip of Hartman Dipping Beds

The same dipping bed can be traced through all of the surveys taken at Hartman ranch. As rotation around the fault occurs there should be a visible change in the apparent dip of the beds. For example, if a fault was dipping at 45 degrees and the survey were perpendicular to the strike, a cross-section would show the true dip. As the survey rotates closer to parallel, the dip of the fault will appear shallower and shallower. If the dip was 45 degrees and the survey was taken at 60 degrees to the fault then the apparent dip would appear to be 40.9 degrees. If the survey were rotated even further around to 30 degrees from the strike, the apparent dip drops all the way to 26.6 degrees. After 60 degrees the rate that the apparent dip changes increases dramatically. The apparent dip (A) can be calculated using the following formula:

$$(4)\ \cos Q = (\tan A)/(\tan D)$$

where Q is the angle off of the strike and D is the true dip.

Low resistivity zone analysis reveals from survey DH01PERP, that: Feature B dips at 108 degrees and Feature C at 96 degrees. These values should be close to the true dip of these features. The apparent dips of these in DH02N30W are: Feature A is calculated at dipping 104 degrees, Feature C dips at 91 degrees. On line DH02PARA Feature A dips at 92 degrees and Feature B dips at 86 degrees.

7.3.3 Clement Spring Field Data

Two surveys were performed on this site. The first survey was roughly north–south, perpendicular to the fault. The second line was run at 30 degrees to the fault. The north–south survey was the longest survey completed on the site at 550 m long. The second survey was only 220 meters long due to terrain constraints.

7.3.3.1 CMT01 Analysis

CMT01 was the first line run at the Clement Springs site (Figure 40). To the southern end of the site are the highly resistive West Spring Creek and Kindblade Formations. East of the 150 meter mark along the line are the Oil Creek and Joins Formations. At 150 meters there is a vertical feature. This feature is represented by low resistivity, less than 50 ohm-m. There is evidence in this area that this fault is a conduit for fluid flow; discharge near the fault trace. There is a dipping feature indicated on the data from CMT01 at 200 meters, it has a resistivity of

around 90 ohm-m. This feature could be a dipping bed or a conduit to water flow. A third resistivity feature is present at 400 meters. This feature has a signature that is similar to the feature at 200 meters.

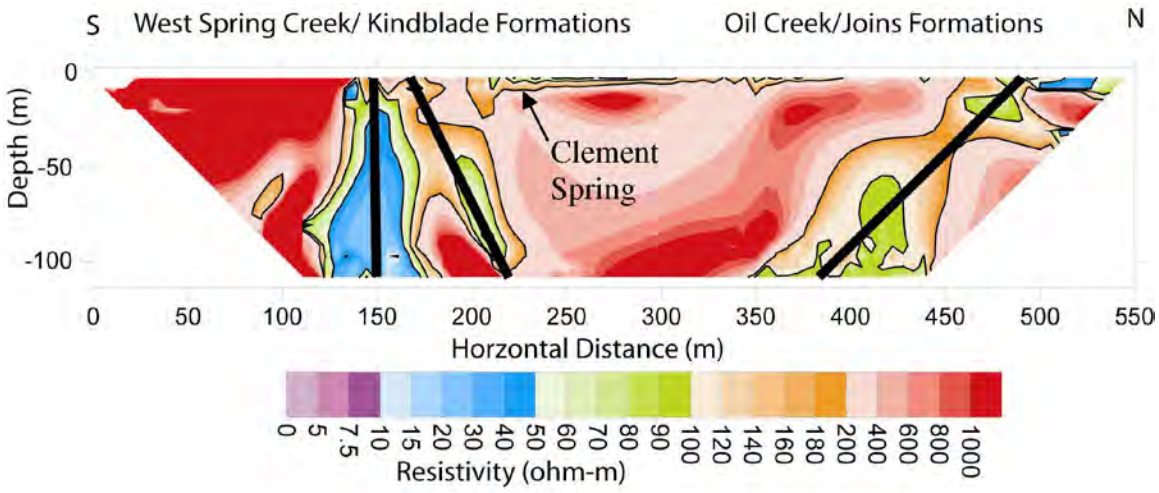

Figure 40. Inverted resistivity section of Clement Springs showing a fault zones. The southern fault is the South Sulphur Fault. The two other marked features are possibly conduits to fluid flow or part of faults themselves.

7.3.3.2 CMT02 Analysis

CMT02 is the second, and shortest, survey done at the Clement Springs site (Figure 41). This survey was oriented at 30 degrees to the strike of the fault. There were three significant features identified in this image. The first, at 110 meters, is a vertical feature with resistivity values down to 15 ohm-m. The second significant feature is the dipping low resistivity feature present at 130 meters. The third is the nearly flat feature at a depth of about 10 meters. This is a significant feature because the spring is located about 20 meters to the north of the 140 meter mark on this survey.

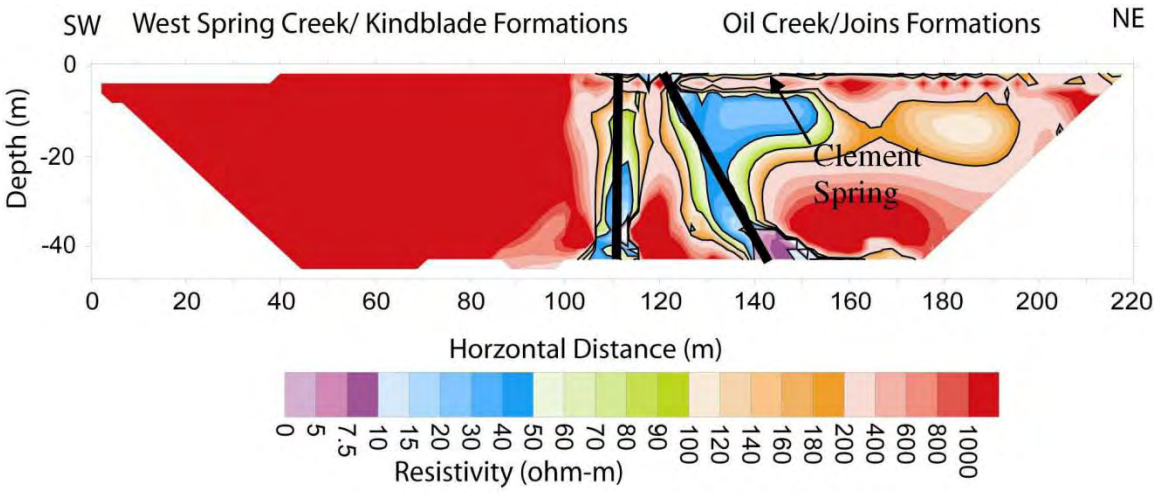

Figure 41. Inverted Resistivity section of Clement Spring 30 degrees to the trend of the fault. Three significant features are identified in this image. The first is interpreted as the fault located at 110 meters. The second is a fluid conduit at 130 meters. Third is a horizontal feature that may be another conduit for fluid flow, and a possible source for the spring.

7.3.4 Apparent Dip of Clement Springs Features

Extended analysis was done on both of the Clement Spring lines (Figure 42). Clement Spring Feature A is dipping at 93 degrees, Feature B is dipping at 72.4 degrees, Feature C is dipping at 118.7 degrees and Feature D is dipping at 72.4 degrees.

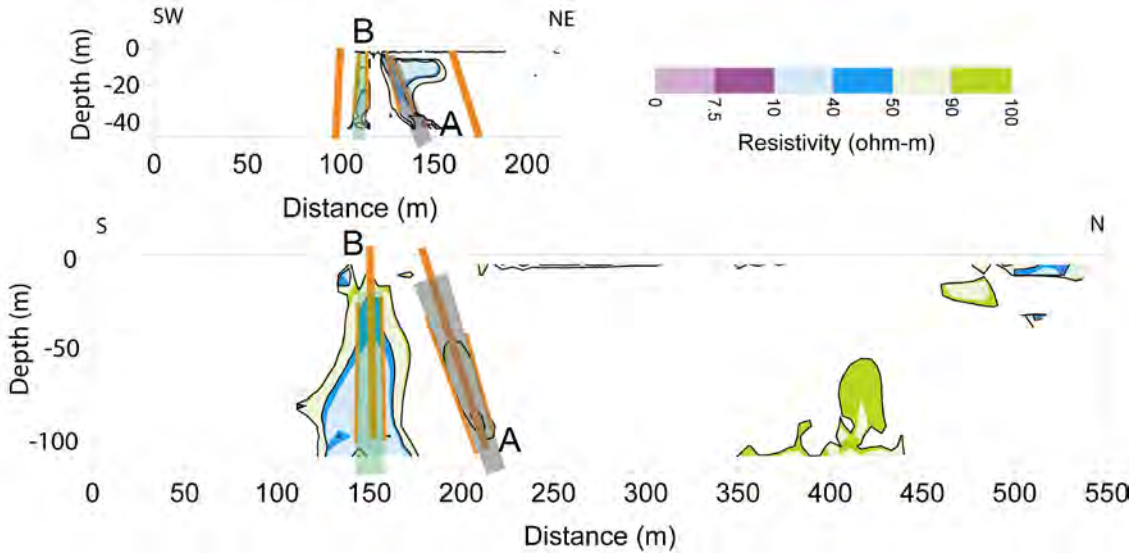

Figure 42. Clement Spring low resistivity analysis. Four dipping features were interpreted in the two images.

7.3.5 I-35 Mile Marker 49 Field Data

A single line was completed, oriented parallel to I-35 at the scenic turnout (Figure 43). This south to north line was 137.5 meters in length. The structural dip to the beds at this location is about 45 degrees to the north, which is apparent in the data on the north half of the image. At 80 meters along the line the first dipping feature can be seen. This feature is likely a dipping bed. Vertical features are apparent as a conductor at 45 meters lateral distance and a resistor at 100 meters lateral distance.

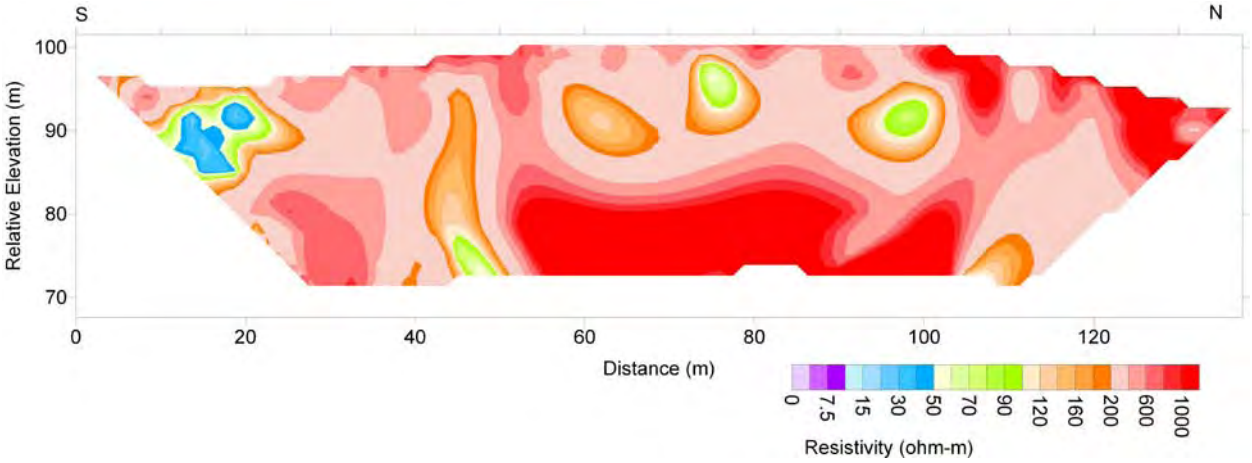

Figure 43. Inverted Resistivity Section showing the I-35 cross-section. A possible fault can be seen at 45 m along the line.

7.4 ERI Comparison with Gravity Data

Gravity data was acquired over much of the field to identify the changes in lithology, identify changes in porosity, and locate and characterize faults and folds. The last part of these goals is the most important for this study as it contributes to identifying the faults and how they trend in the subsurface. The work in the study was done for the United States Geologic Survey (USGS) over a 20 month period in 2004 and 2005 (Scheirer and Scheirer, 2006).

A continuous gravity survey was completed across the area (Figure 5.18). The faults that were located and identified in the surveys were the: Sulphur Fault, South Sulphur Fault, Mill Creek Fault, and Reagan Fault (Scheirer and Scheirer, 2006). The two faults that are relevant to this study are the South Sulphur Fault and the Mill Creek Fault.

The South Sulphur Fault, from the gravity modeling, shows the fault with a slight dip to the north in the western part of the study area. As the fault proceeds west the best fit in the model moves the fault more towards a vertical fault. The dipping of the fault to the east does not agree with the modeled data from the resistivity for the major area of resistivity change. Figures 44 and 45 shows the gravity profile along with the resistivity line of the South Sulphur Fault.

The Mill Creek Fault, near Hartman Ranch, was also part of the gravity survey and shows the South Sulphur Fault at the area of the survey to be nearly vertical. This concurs with the resistivity data that was taken at the Hartman Ranch. At the Hartman Ranch site the Mill Creek Fault seems to be a vertical fault near the surface. Figure 46 shows the gravity data for the area around Hartman Ranch.

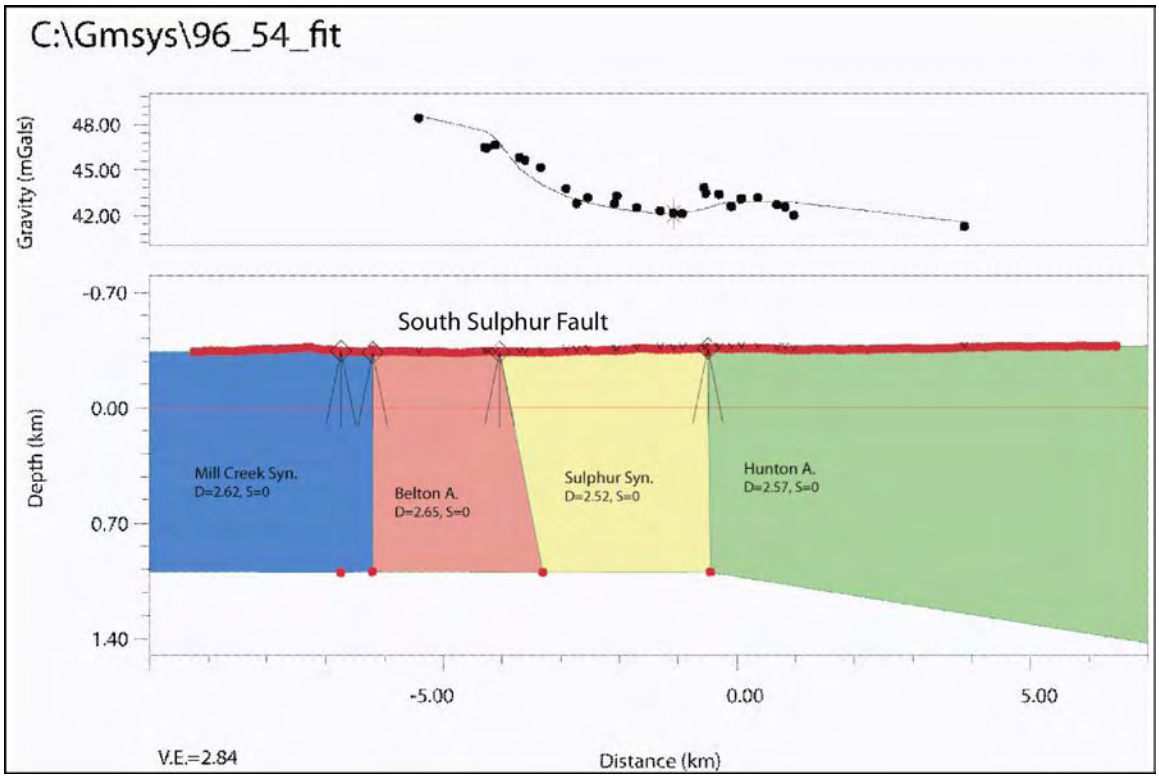

Figure 44. Gravity survey completed by the USGS. The South Sulphur Fault is indicated in the image as a dipping bed (Scheirer and Scheirer, 2006).

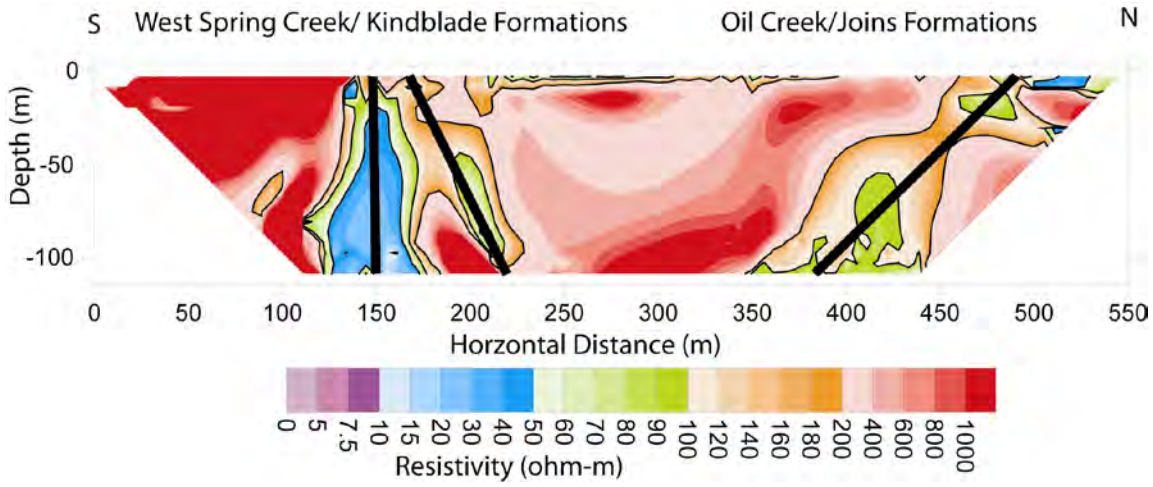

Figure 45. Resistivity survey of the South Sulphur Fault showing a near vertical resistivity feature at 150 meters.

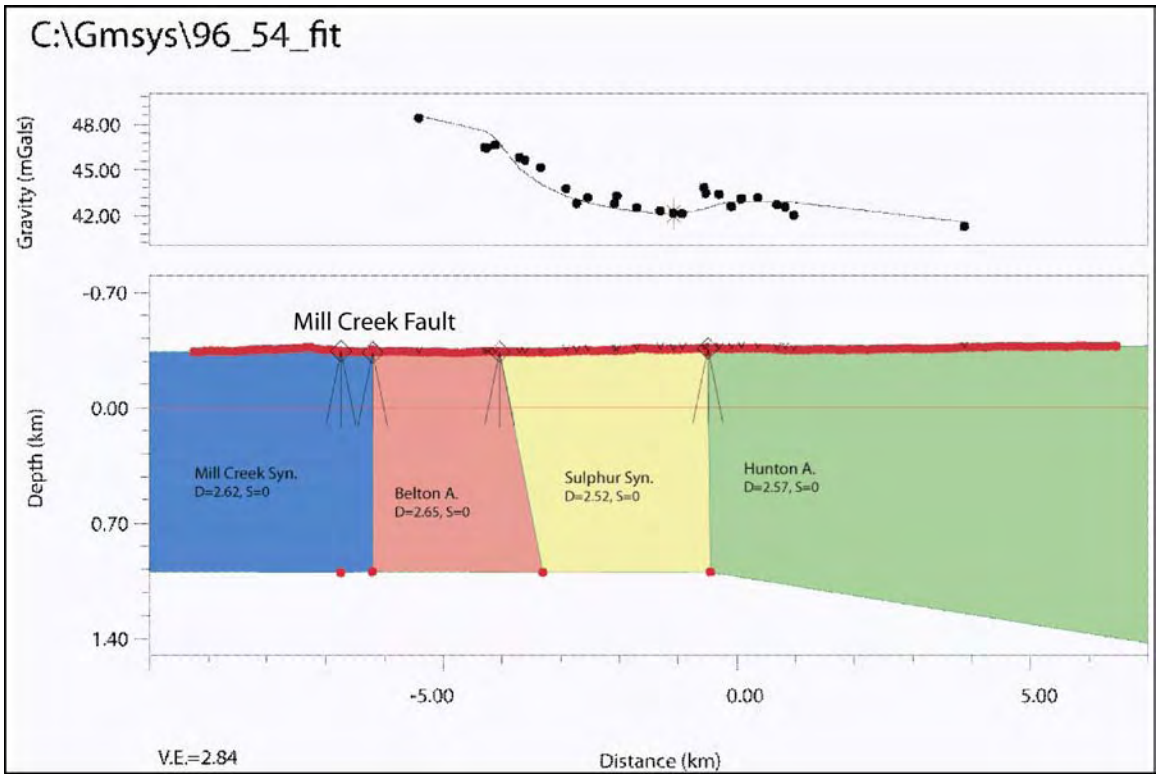

Figure 46. This image shows the Mill Creek Fault as a vertical fault in the vicinity of Hartman Ranch (Scheirer and Scheirer, 2006).

7.5 Discussion

Forward modeling answered the questions on the ability to model data and addressed problems that were presented by gridded data. This work showed similar trends in the modeled data versus the field data. Field conditions that may have affected data collection are also examined.

7.5.1 ERI Forward Modeling

Forward modeling was completed to establish limits for the software and inversion methods. Interestingly there is a connection between the contrast ratio of the image and the ability to accurately resolve the fault. This seems to be the result of the averaging algorithm that is used to calculate the grid values. When the contrast increases the averaging also increases in radius. This has the affect highlighting the fault and making it easier to see but less accurate. At lower contrasts the faults are harder to image but easier to accurately select. From the forward modeling, it was determined that the highest instance of error from the fault picking algorithm is at the 23 degree angle. This is interesting because that is the angle that intercepts the corner of the image and begins to track up the side.

To obtain the best results from the forward modeling, the first and lower three points in the analysis of the fault were dropped. The field data showed similar results with the data quality degrading with depth. Therefore the field data analysis was done with the lower three data points removed from the data set.

Grid error and depth error are always present in the data. This is an unavoidable issue that limits the resolution of faults by several degrees. An understanding of how the grid system operates helps with the picking of faults. Acquisition error is present in all data sets collected. The best way to minimize this error is by minimizing the contact resistance as much as possible. With this error reduced and the grid and depth error present, the faults can be resolved to a degree of accuracy of 5 degrees.

7.5.2 ERI Field Surveys

Data collection at these sites was difficult as bedrock was on or near the surface at all locations. Because of this contact resistances varied across all field sites. Salt water was added to reduce the contact resistance to below 500 ohm-m. Vegetation was not a factor in the placement of the surveys or had a pathway present along the length of the line.

7.5.2.1 Hartman Ranch

The Hartman Ranch has a number of sink holes on site. Sinkholes are characteristic in the dolomite and limestone along the northern half of the site. A large sinkhole was located at the north end of the preliminary line run at the site. This sinkhole was approximately 16 feet across and 15 feet deep. Overall contact resistance error was low at this site. The contact resistance for problem electrodes dropped below the upper limit of 500 ohm-m with addition of the salt water solution.

The corrected apparent dip values for low-resistivity features were used to identify two dipping beds at the Hartman Ranch field site. Feature C on line DH01PERP correlates well with Features A on DH02N30W and C on DH02PARA, which have corrected dips of approximately 90 degrees. Feature B on line DH01PERP correlates well with Feature A on line DH02PARA at around 108 degrees.

7.5.2.2 Clement Spring

The southern half of the field site is composed primarily of well indurated limestone and dolomite. This presented problems when trying to lower the contact resistance of some electrodes. Even with the salt water solution, the contact resistance for some electrodes was above the 500 ohm-m limit. This added error to the data sets; however the poorer quality data was removed to reduce the error.

A spring discharged along the fault at this site. This spring may be the source of the lower resistivity anomaly in the two images from this site. Water flowing up the fault along fractures, on bedding planes near the surface, may be the source of the water for the spring.

7.5.2.3 I-35 Mile Marker 49

This site was exposed conglomerate along the entire line. There was a large amount of drilling necessary at this site. The hole for each electrode location had to be drilled. The conglomerate was difficult to drill. The hammer drill that we were using suffered catastrophic failure approximately half way through the line and an additional drill mobilized to the site.

7.6 Conclusions

Electrical resistivity imaging is a powerful tool that can be used to identify fault locations and dips to an accuracy of 10 degrees. Even though some sources of error are present, they are relatively minor if the following suggestions are followed:

1. Use longer lines to extend below weathered portions of faults.
2. Survey as close to perpendicular to the fault as possible.
3. The closer to parallel the line is to the fault, the longer the line must be to determine the fault dip accurately.
4. Shorter line lengths induce greater error due to (1) GPS error of the end points and (2) increased grid error resulting from increased grid spacing.
5. Keep location of the fault near the center of the line.
6. The closer the fault is to the corner of the model, the greater the grid error.
7. Correct for depth error.
8. As the fault approaches vertical the depth error increases. Depth errors can be averaged to approximately 5 degrees.

For the Arbuckle-Simpson aquifer, faults are readily apparent in ERI images above and below the water table. The faults tend to be near vertical with a fault zone width that extends 5-10 meters. Springs in the aquifer that occur along faults may not necessary coincide with the most conductive regions regionally, but do correspond to conductive regions of an individual image. The presence of clay zones in the images indicates that each conductive area in ERI images may not correspond to high flow zones for the aquifer. The fault zones tend to be uniform with depth. However, interpretation is limited to the depth that good quality data can be collected.

8.0 Borehole Method Evaluation

The borehole equipment developed as part of the research worked reasonably well. There were difficulties in deploying the equipment down boreholes due to the lack of open deep boreholes and the quality of the available boreholes. The primary difficulty in utilizing the approach is finding adequate methods to process the datasets.

8.1 ERI Equipment

The surface equipment and procedures were well established prior to these experiments and performed as expected. The BERI cable and accompanying procedures were modified throughout the experiments.

The BERI cable was constructed of heavy duty cable, but a metal insert or side cable could not be used as it would short out the experiments. A Kevlar line was used as a safety to provide stability to the BERI and to allow a minimum amount of tension to be placed on the BERI. The two cable system proved problematic due to the borehole condition of the deeper Wingard 2 borehole. In locations where the borehole was damaged, the Kevlar line would catch on the sides of the borehole and made moving the cable up or down problematic. Several safety cable configurations were attempted, but poor borehole quality will remain a difficulty for the system. The shallow Hatch well did not present any problems for the equipment.

A disinfection procedure was developed after encountering decaying matter in the Wingard well. A bleach and water mixture was used to wash the BERI as it entered the next well to ensure that no bacteria could be introduced into subsequent wells. This procedure was reasonably easy as the cable was free from the power reel for a length of approximately 5 meters prior to going into the borehole.

8.2 Hatch Well Site

Surface ERI surveys collected good quality data at the site (Figure 48). The inversions of the data provided low root mean squared (RMS) error of between 3.2% and 5.2%. The dataset had between 94.6%-96.1% of the data used in the inversions. The remaining data did not meet the data quality criteria of high signal strength and low error. Compared to other datasets at other locations, these would rank as very good.

Surface ERI surveys at the Hatch well site provided several similar features at various orientations from the well. The images demonstrate a broad range of resistivity values from as low as 1.3 ohm-m to over 100,000 ohm-m. The upper 10 ft (3 m) of the subsurface is very conductive for carbonate area with resistivity below 100 ohm-m. This is interpreted as a soil zone, although bedrock was outcropping at the surface at the site. This zone exists above a very irregular boundary that is likely a feature of carbonate weathering. This interpretation is consistent with zones called epikarst, which have been shown to be important as water storage zones in karst aquifers. The ERI surveys also have a number of conductive (< 100 ohm-m) features in the deeper portions of the images. These zones are irregular conductive features that are interpreted as either highly weathered bedrock or soil filled voids.

At the various orientations, the variability in the data was significant. The irregular 100 ohm-m boundary varied from 0 – 35 feet (0 – 11 m). Deep conductive zones were present at all orientations, except at 150 degrees where no deep conductive zone was present. The high resistivity portions of the images range from several thousand ohm-m to hundreds of thousands. This likely reflect the variability of bedrock weathering at the site.

Figure 47. Equipment setup at Hatch well site for image at orientation of 50 degrees. Picture is taken from the north looking south (from Halihan et al, 2004).

The borehole-surface surveys were difficult at the site due to the limited depth of the well and the deep level of the water table (Figure 48). The data that was collected had high signal strength and low error. However, the inversion software had difficulty modeling the data. This is due to the unique data collection scheme and the fact that the inversion software is very new. The software was only developed recently, and modifications due to this project are expected. The data used for the inversion included 78.1% of the initial dataset and resulted in an inversion with an RMS error of 9.1%. These results can be improved with modification of the inversion code.

The inversion that was conducted showed similar features to the surface surveys (Figure 48). The conductive zones below 60 feet (18 m) are expected to be fractured bedrock. The ERI image also indicates that multiple conductive features are present from the surface to the bottom of the well. This may indicate significant vertical hydraulic conductivity in the shallow portions of the aquifer. Hydraulic testing would be required to confirm this.

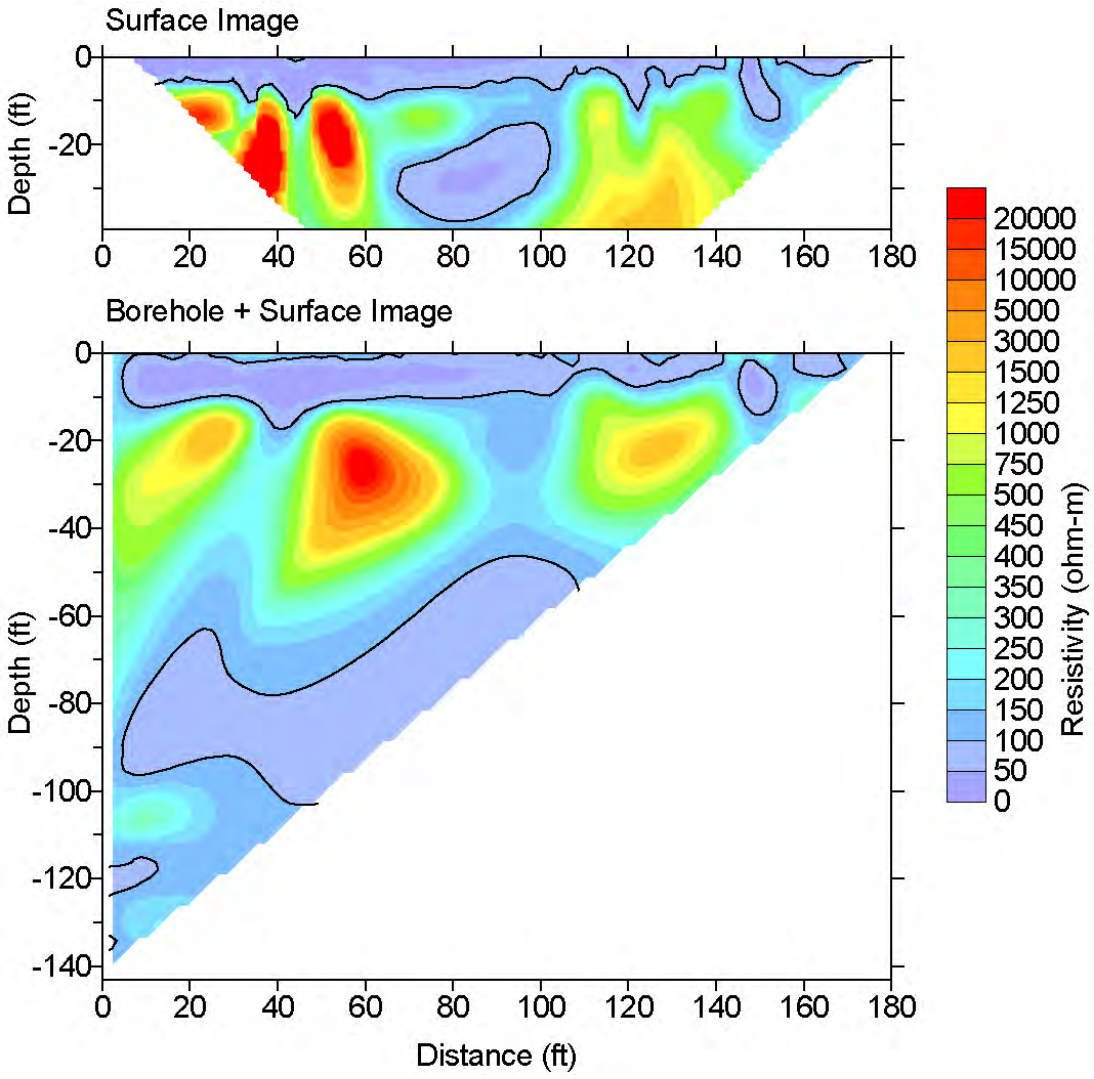

Figure 48. Surface ERI survey and Borehole-surface ERI survey collected at orientation due north of Hatch well. Note the strong conductive features near the surface (top 10 feet) and vertically at 40 and 90 feet lateral distance from the well (from Halihan et al, 2004).

8.3 Wingard 2 Well Site

Surface ERI surveys collected good quality data at the site (Figure 49). The inversions of the data provided low root mean squared (RMS) error of between 3.5% and 6.7%. The dataset had between 94.7%-95.0% of the data used in the inversions. The remaining data did not meet the data quality criteria of high signal strength and low error. Compared to other datasets at other locations, these would rank as very good.

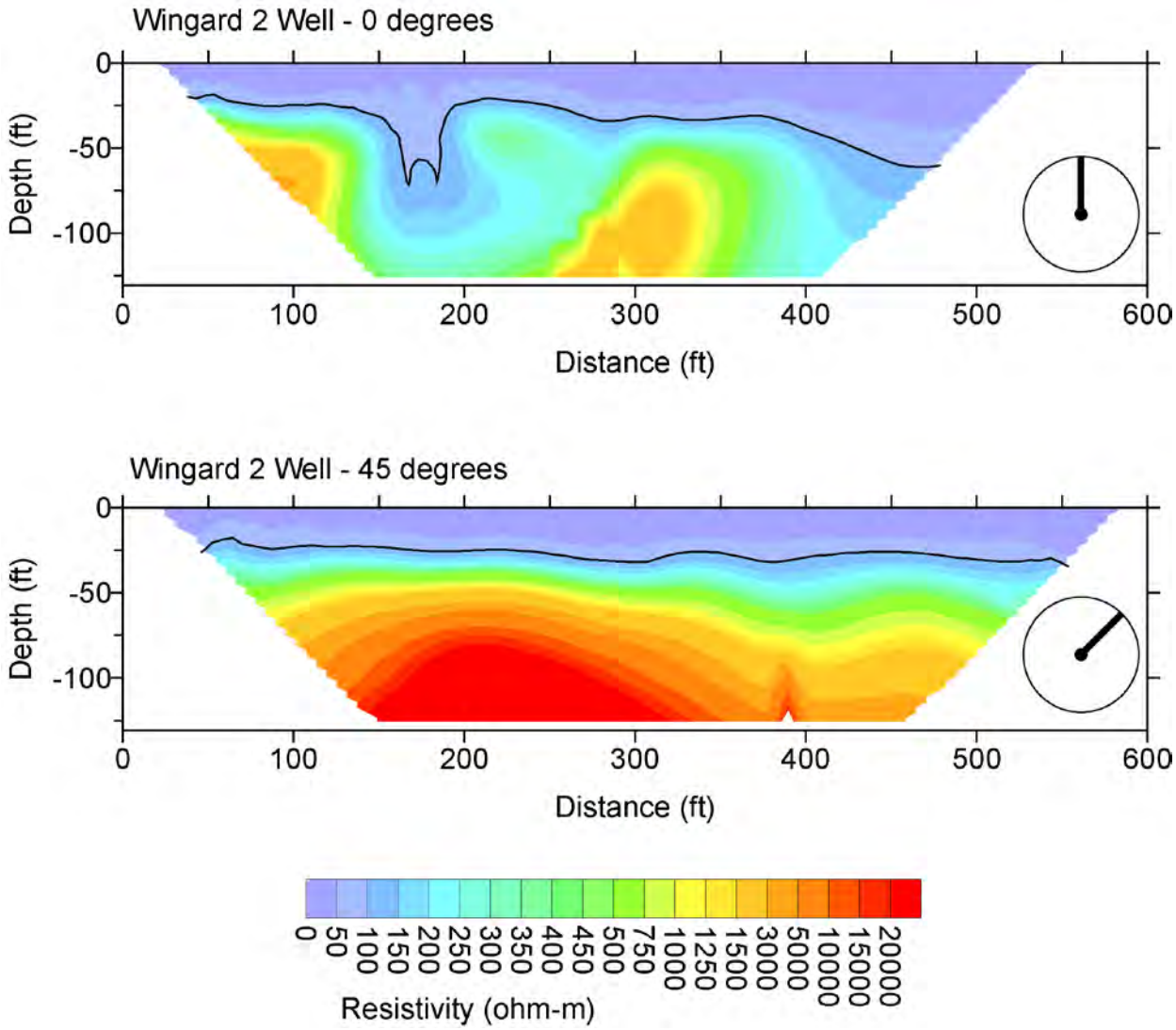

Figure 49. Surface ERI survey results at the Wingard 2 well site. The images are scaled identically and the "clock" figure at the right indicates the orientation, relative to north being up, of each image relative to the well (from Halihan et al, 2004).

Surface ERI surveys at the Hatch well site provided several similar features at various orientations from the well and compared to the Hatch well site (Figure 49). The images demonstrate a broad range of resistivity values from as low as 6.6 ohm-m to nearly 100,000 ohm-m. This is a similar range to the Hatch well. The upper 30 ft (10 m) of the subsurface is very conductive for carbonate area with resistivity below 100 ohm-m. This is interpreted as a soil zone, and is approximately three times as thick as at the Hatch well site. This zone exists above a very irregular boundary on the north south line, but the boundary appears nearly horizontal on the line running northeast of the well. This type of weather is expected in carbonate regions. This potential epikarst zone could be an important water storage zone for the aquifer.

At the two orientations, the variability in the data was significant. The 100 ohm-m boundary varied from highly irregular to nearly horizontal. Deep conductive zones were present at the north south orientation, but not at the northeast orientation. The high resistivity portions of the images range from several thousand ohm-m to hundreds of thousands. This likely reflects the variability of bedrock weathering at the site, but also indicates that well data may not provide a full picture of how the aquifer is functioning.

The deep data for the Wingard 2 well was of good quality. The well was used to collect data down to 1000 feet (305 m), but the difficulties with the irregularities of the borehole did not allow the collection of a complete set of data due to concern about damaging or losing the cable. The data that was collected was analyzed to determine the field data quality at depth, but an inversion of the deep data was not possible with the currently available software.

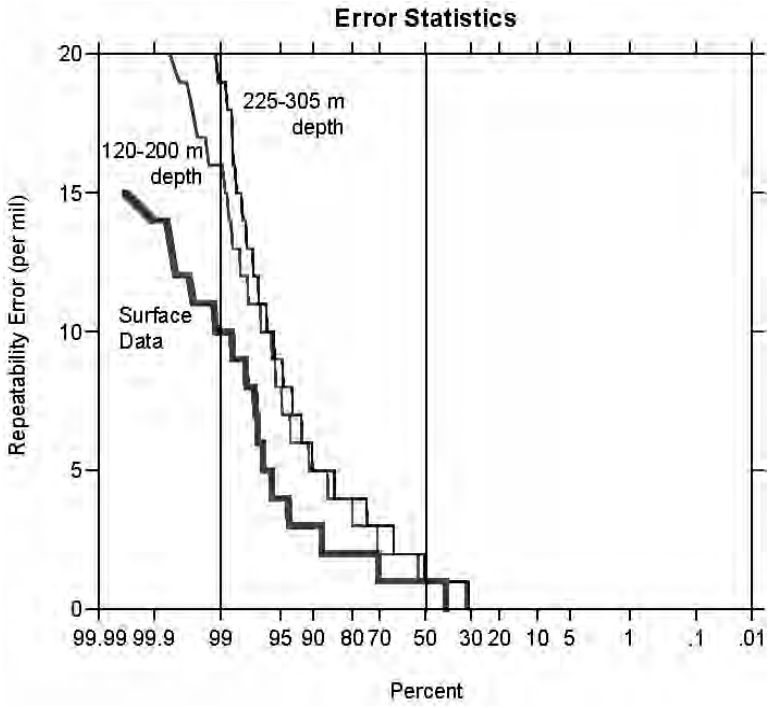

Figure 50. Data repeatability error distribution for ERI data collected at the Wingard 2 well. The median value line and the lowest 1% line are highlighted. The repeatability error is in units of per mil, so the scale is from 0-2% error (from Halihan et al., 2004).

The data repeatability error, which is the ability to repeat an individual measurement, did increase with depth of the BERI cable (Figure 50). Approximately 50% of the data in all datasets was repeatable to less than 0.1% error. Less than 1% of the data was not repeatable within 2%. This gives confidence that the data collection procedures are repeatable.

The injection current for the BERI cable data also became weaker with depth (Figure 12). The instrument adjusted to lower currents when a signal was not possible, and this is shown by the steps in the injected current distribution (Figure 51a). This analysis allows the weaker measurements to be eliminated from the dataset. The overall signal strength of the BERI cable is higher when compared to the surface cable. The strong signal allows for confidence in the inversion results.

A) B)

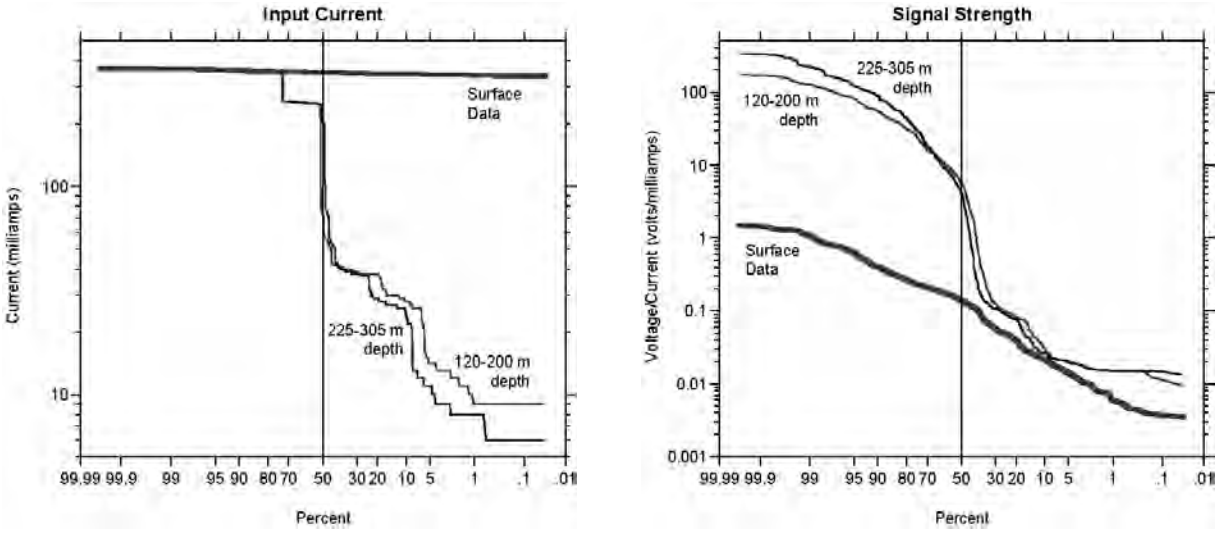

Figure 51. Electrical signal properties for Wingard 2 site data. A) Distribution of injected current during surveys for surface surveys and borehole surveys at two depths. B) Signal strength distribution for same set of surveys (from Halihan et al., 2004).

8.4 Clay Jack Well

A dataset was collected at the Clay Jack well to determine if the processing difficulties were due to data acquisition difficulties at the Wingard 2 Well site. Although the dataset was complete and the data quality was good, no stable inversion could be obtained. Alterations to grid parameters, data density, and inversion settings were performed, but not stable inversion could be obtain. The processing problem with this electrode geometry remains poorly understood.

9.0 Discussion

The ERI images from the Arbuckle-Simpson aquifer indicate that ERI can be a useful tool for improving conceptual models of the aquifer. The data that can be collected in this area is of high quality and provides useful information about the variability of the aquifer. In some bedrock settings, the high resistivity of the lithology makes ERI difficult to employ, but the resistivity of the Arbuckle-Simpson is highly variable and provides a range of electrical properties which can be imaged with the technique.

Surface imaging can provide information on fault location along with data about the thickness of soil zone and the soil/bedrock interface or epikarst zone. This will be important for constructing the storage properties of the aquifer in the shallow areas in the ground water model. The ERI data suggest that the faults can be hydraulically conductive, but their complet hydraulic structure is unclear. While some provide conduits for flow, others may provide barriers, or the faults may be acting as both conduits and barriers.

Borehole imaging of the aquifer provides a similar image to the surface images and indicates that vertically conductive zones may exist for large distances into the subsurface. Inversion software improvements and modified field procedures can improve the borehole imaging datasets, but good borehole imaging sites are the more difficult portion of the work. The limited number of deep undamaged, unused wells limits the ability to obtain good quality data about the structure of the aquifer at depth.

10.0 Conclusions

ERI data was used to address four objectives for the Arbuckle-Simpson aquifer. First, the background properties of the major lithologies were assessed using quarries and outcrops. Second, the properties of the epikarst zone of the aquifer were evaluated. Third, the fault orientations in the aquifer were measured for several major faults. Finally, a borehole technique was evaluated with the technique.

Using quarries and soil-free outcrops where possible, the lithologies of the Arbuckle-Simpson aquifer system were evaluated to determine the electrical properties of the native unfractured formations. The evaluation indicates that the lithologies of the aquifer system have a wide range of resistivities that makes the technique useful for electrical mapping in the aquifer.

Three sites were intensively investigated to evaluate the thickness, conductivity, and storage properties of the mantled epikarst of the Arbuckle-Simpson aquifer. The results indicate that the soil thicknesses available from the MIADS database correlate with the thicknesses derived from direct push depth of refusal. The epikarst zone is approximately 9 times larger than the soil zone. The hydraulic conductivity of these areas is similar to the expected value for the materials present, but the analysis used resulted in values that were smaller than larger field scale measurements. The storage potential of the mantled epikarst region appears to be the same order of magnitude as storage in the aquifer. This may influence site scale properties of recharge and contaminant transport in the Arbuckle-Simpson aquifer.

For the Arbuckle-Simpson aquifer, faults are readily apparent in ERI images above and below the water table. The faults tend to be near vertical with a fault zone width that extends 5-10 meters. Springs in the aquifer that occur along faults may not necessary coincide with the most conductive regions in an image, but do correspond to conductive regions of an individual image. The fault zones tend to be uniform with depth. However, interpretation is limited to the depth that good quality data can be collected. The presence of clay zones in the images indicates that each conductive area in ERI images may not correspond to high flow zones for the aquifer.

The borehole method that was tested has proven difficult to apply to the aquifer due to a lack of suitable borehole locations to test. Few deep boreholes exist and those that do exist have problems accommodating even a small diameter cable. Surface surveys work well in the aquifer, but are limited to how deep they can easily image. The borehole system was tested in

three wells in the aquifer. The resulting field data are of good quality, but the available processing methods could provide a stable solution given the complex grid geometry of the array.

11.0 Appendices

Appendix A1. ERI Site Location Maps

Appendix A2. ERI Images

Electronic Appendix E1. Processed ERI Datasets

12.0 References

Archie, G. E., 1942, The electrical resistivity log as an aid to determining some reservoir characteristics.: Transactions of the American Institute of Mechanical Engineers, v. 146, p. 389-409.

Bear, J., 1972, Dynamics of Fluids in Porous Media: New York, American Elsevier Publishing Company, 764 p.

Bosak, P., and V. Benes, 2003, Geophysical characteristics of epikarst: case studies from Zagros Mts. (Iran) and the Koneprusy region (Czech Republic): Acta Carsologica, v. 32, p. 255-267.

Cai, J., G. A. McMechan, and M. A. Fisher, 1996, Application of ground-penetrating radar to investigation of near-surface fault properties in the San Francisco Bay region: Bulletin of the Seismological Society of America, v. 86, p. 1459-1470.

Cemen, I., R. A. Young, and T. Halihan, 2008, Determination of Fracture Density in the Arbuckle-Simpson Aquifer from Ground Penetrating Radar (GPR) and Resistivity Data, Stillwater, OWRRI.

Christenson, S., N. Osborn, and C. R. Neel, 2007, Groundwater hydrology of the Arbuckle-Simpson aquifer: Oklahoma Water Research Symposium.

Daily, W., A. Ramirez, A. Binley, and D. LaBrecque, 2004, Electrical resistance tomography: The Leading Edge, p. 438-442.

Demanet, D., F. Renardy, K. Vanneste, D. Jongmans, T. Camelbeeck, and M. Meghraoui, 2001, The use of geophysical prospecting for imaging active faults in the Roer Graben, Belgium: Geophysics, v. 66, p. 78-89.

Fairchild, R. W., R. L. Hanson, and R. E. Davis, 1990, Hydrology of the Arbuckle Mountains area, south-central Oklahoma, *in* Oklahoma Geological Survey (OGS), ed., Circular 91, Norman, OK, p. 112.

Fetter, C. W., 2001, Applied Hydrogeology: Upper Saddle River, NJ, Prentice-Hall, Inc., 598 p.

Griffiths, D. H., and R. D. Barker, 1993, Two-dimensional resistivity imaging and modeling in areas of complex geology: Journal of Applied Geophysics, v. 29, p. 211-226.

Halihan, T., S. Paxton, J. Puckette, and M. Sample, 2004, Preliminary Electrical Resistivity Imaging Report for: The Arbuckle-Simpson Hydrology Study, p. 27.

Halihan, T., S. T. Paxton, I. Graham, T. R. Fenstemaker, and M. Riley, 2005, Post-remediation evaluation of a LNAPL site using electrical resistivity imaging: Journal of Environmental Monitoring, v. 7, p. 283-287.

Ham, W. E., 1969, Regional geology of the Arbuckle Mountains, Oklahoma: Guidebook 17: Norman, OK, 52 p.

Herwanger, J. V., M. H. Worthington, R. Lubbe, and A. Binley, 2004, A comparison of cross-hole electrical and seismic data in fractured rock: Geophysical Prospecting, v. 52, p. 109-121.

Klimchouk, A., 2004, Towards defining, delimiting and classifying epikarst: Its origin, processes and variants of geomorphic evolution: Speleogenesis and Evolution of Karst Aquifers, v. 2, p. 1-13.

Loke, M. H., and R. D. Barker, 1996, Rapid least-square inversion of apparent resistivity pseudosections using a quasi-Newton method: Geophysical Prospecting, v. 44, p. 131-152.

Louis, I. F., D. Raftopoulos, I. Goulis, and F. I. Louis, 2002, Geophysical imaging of faults and fault zones in the urban complex of Ano Liosia Neogene Basin, Greece: synthetic simulation approach and field investigations: International Conference on Earth Sciences and Electronics, p. 269-285.

Nguyen, F., S. Garambois, D. Jongmans, E. Pirard, and M. H. Loke, 2005, Image processing of 2D resistivity data for imaging faults: Journal of Applied Geophysics, v. 57, p. 260-277.
Niwas, S., and O. A. L. de Lima, 2003, Aquifer parameter estimation from surface resistivity data: Ground Water, v. 41, p. 94-99.
Nord, J. D., 1996, Geologic and hydrologic controls on flow at Vendome Well, Sulphur, OK: Master of Sciences thesis thesis, Oklahoma State University, Stillwater, OK, 147 p.
Perrin, J., P.-Y. Jeannin, and F. Zwahlen, 2003, Epikarst storage in a karst aquifer: a conceptual model based on isotopic data, Milandre test site, Switzerland: Journal of Hydrology, v. 279, p. 106-124.
Purvance, D. T., and R. Andricevic, 2000a, Geoelectric characterization of the hydraulic conductivity field and its spatial structure at variable scales: Water Resources Research, v. 36, p. 2915-2924.
Purvance, D. T., and R. Andricevic, 2000b, On the electrical-hydraulic conductivity correlation in aquifers: Water Resources Research, v. 36, p. 2905-2913.
Ramirez, A., W. Daily, D. LaBrecque, E. Owen, and D. Chesnut, 1993, Monitoring an underground steam injection process using electrical resistance tomography, Water Resources Research, United States, American Geophysical Union: Washington, DC, United States, p. 73.
Reynolds, J. M., 1997, An introduction to applied and environmental geophysics: Chichester; New York, John Wiley, ix, 796 p.
Reynolds, W. D., D. E. Elrick, and E. G. Youngs, 2002a, The soil solution phase. Ring or cylinder infiltrometers (vadose zone), *in* J. H. Dane, and G. C. Topp, eds., Methods of soil analysis, Part 4. Physical Methods, Agronomy Monograph No. 5: Madison, WI, SSSA, p. 818-820.
Reynolds, W. D., D. E. Elrick, E. G. Youngs, and A. Amoozegar, 2002b, The soil solution phase. Field methods (vadose and saturated zone techniques), *in* J. H. Dane, and G. C. Topp, eds., Methods of soil analysis, Part 4. Physical Methods, Agronomy Monograph No. 5: Madison, WI, SSSA, p. 817.
Riley, M., 2007, Investigation of Fault Properties Using Electrical Resistivity Imaging, Oklahoma State University, Stillwater, 56 p.
Rovey, C. W., and D. S. Cherkauer, 1995, Scale dependency of hydraulic conductivity measurements: Ground Water, v. 33, p. 769-780.
Sample, M. A., 2008, Characterization of the Epikarst over the Hunton Anticline, Arbuckle-Simpson Aquifer, Oklahoma, Oklahoma State University, Stillwater, 207 p.
Scheirer, D. S., and A. H. Scheirer, 2006, Gravity Investigations of the Chickasaw National Recreation Area, south-central Oklahoma, USGS, p. 42.
Soil Survey Division Staff, 1993, Soil Survey Manual: Soil Conservation Service, U.S.D.A. Handbook 18, U.S. Department of Agriculture, Soil Conservation Service, 437 p.
Soil Survey Division Staff, 2005, Soil surveys of Pontotoc and Johnston County, Oklahoma, http://soildatamart.nrcs.usda.gov/Survey.aspx?State=OK.
Stollar, R. L., and P. Roux, 1975, Earth resistivity surveys; a method for defining ground-water contamination, Ground Water, United States, National Water Well Association, Ground-Water Technology Division : Urbana, IL, United States, p. 145.
Suneson, N. H., 1997, The geology of the eastern Arbuckle Mountains in Pontotoc and Johnston Counties, Oklahoma, *in* Oklahoma Geological Survey (OGS), ed., Open-File Report (OFR) 4-97, Norman, p. 1-22.
Suzuki, K., S. Toda, K. Kusunoki, Y. Fujimitsu, T. Mogi, and A. Jomori, 2000, Case studies of electrical and electromagnetic methods applied to mapping active faults beneath the thick quaternary: Engineering Geology, v. 56, p. 29-45.
Todd, D. K., 1959, Ground Water Hydrology: New York, John Wiley & Sons, Inc.

Van Nostrand, R. G., and K. L. Cook, 1966, Interpretation of Resistivity Data, Geological Survey Professional Paper, United States Government Printing Office, Washington, United States Geological Survey.
Weight, W. D., and J. L. Sonderegger, 2001, Manual of applied field hydrogeology: New York, McGraw Hill.
Williams, P. W., 1983, The role of the subcutaneous zone in karst hydrology: Journal of Hydrology, v. 61, p. 45-67.

Appendix 1

ERI Site Location Maps

A)

Figure A1.1A. Arbuckle-Simpson Ranch site showing location of ERI lines. Aerial photo courtesy of Google Earth.

B)

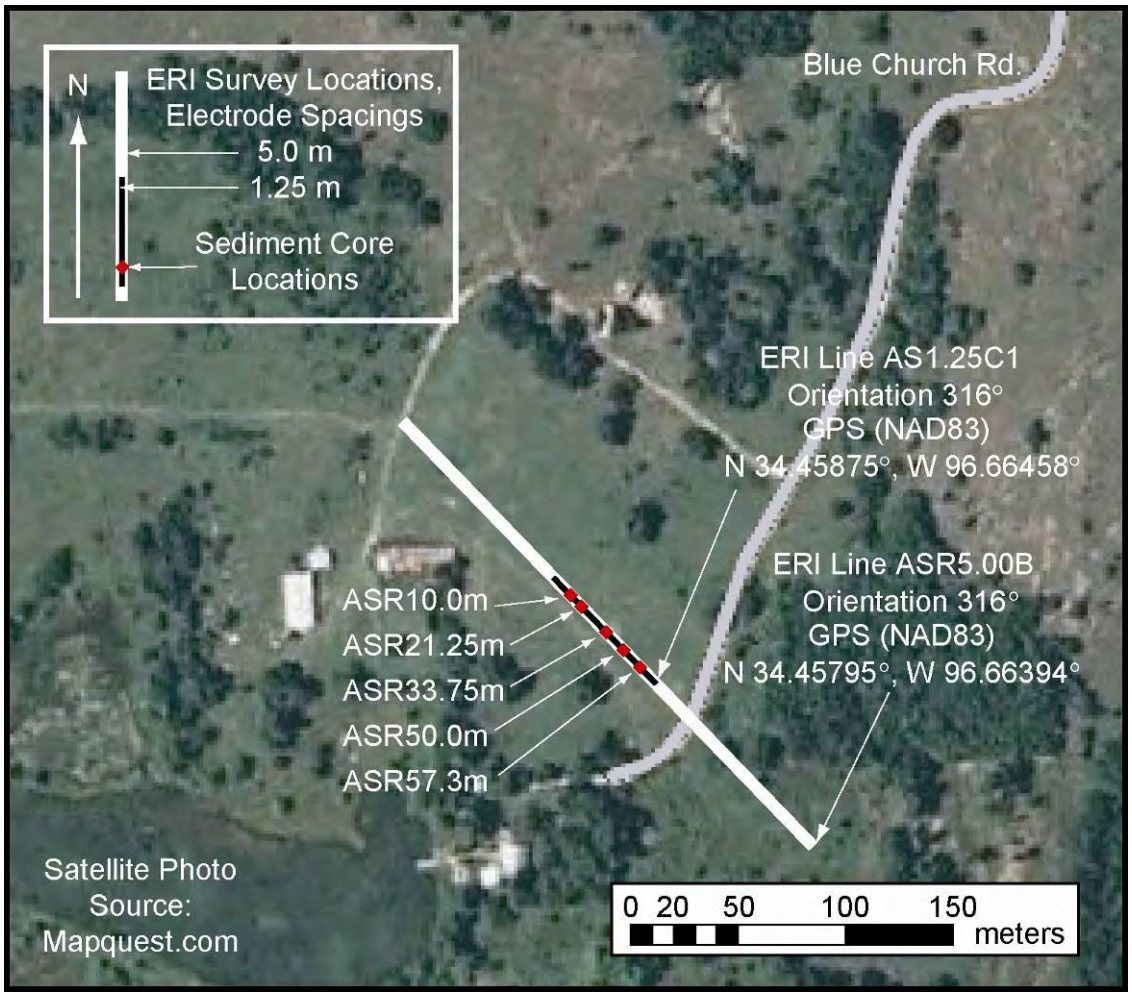

Figure A1.1B. Arbuckle-Simpson Ranch site map with surface electrical resistivity and direct push locations (from Sample, 2008). Aerial photo courtesy of Mapquest.

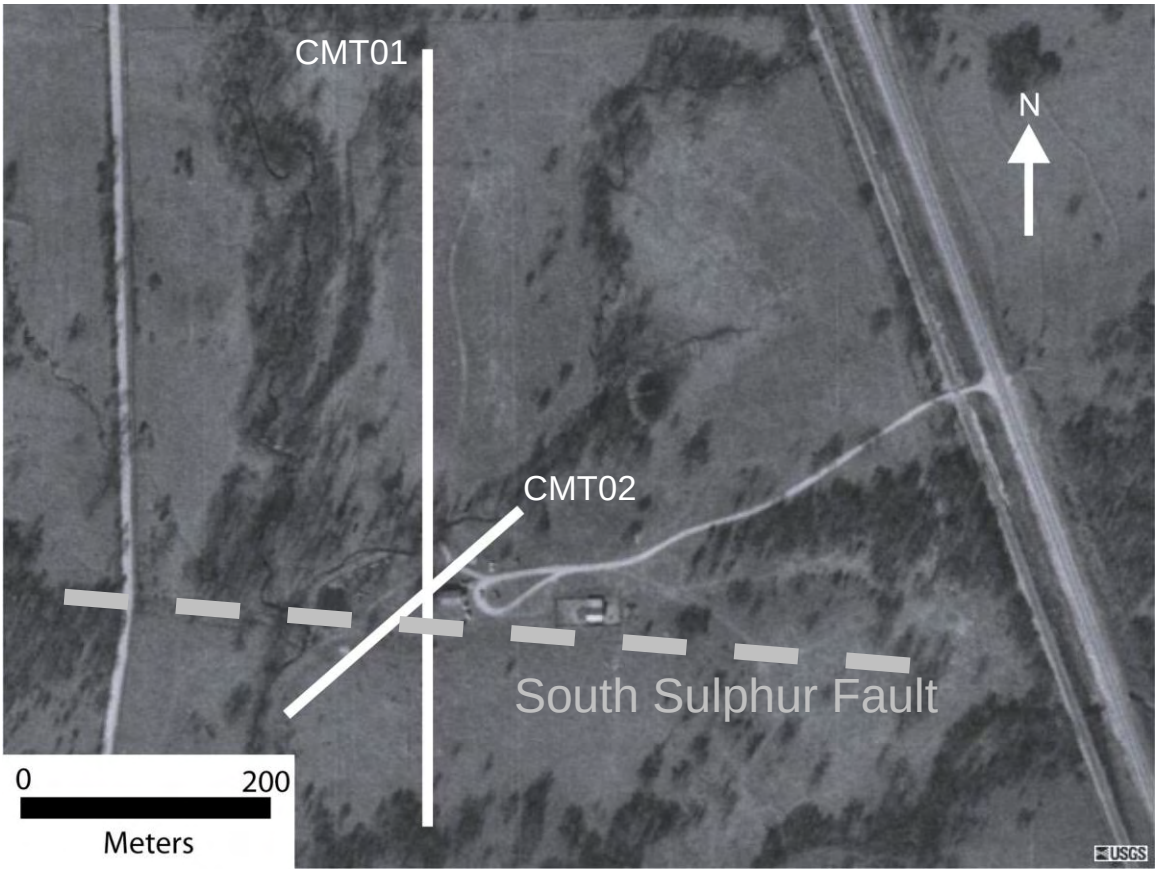

Figure A1.2. Clement Springs site location map showing electrode line locations (from Riley, 2007). Aerial photo courtesy of USGS.

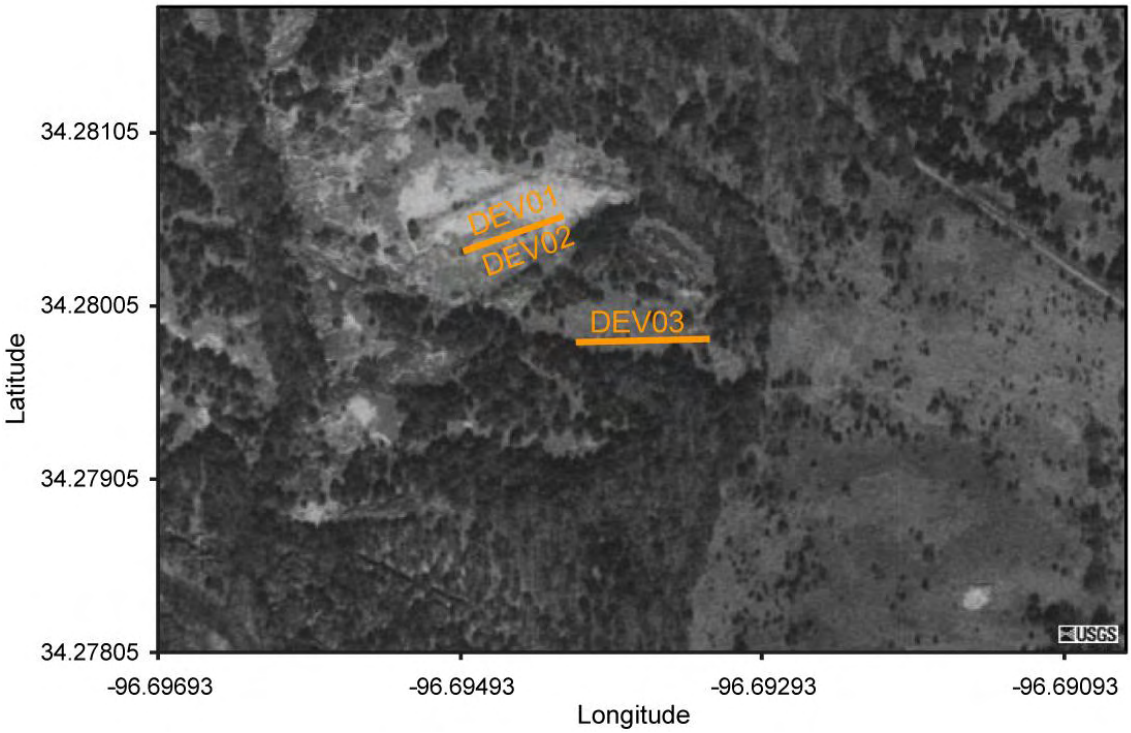

Figure A1.3. Devil's Den site location map showing electrode line locations. Aerial photo courtesy of USGS.

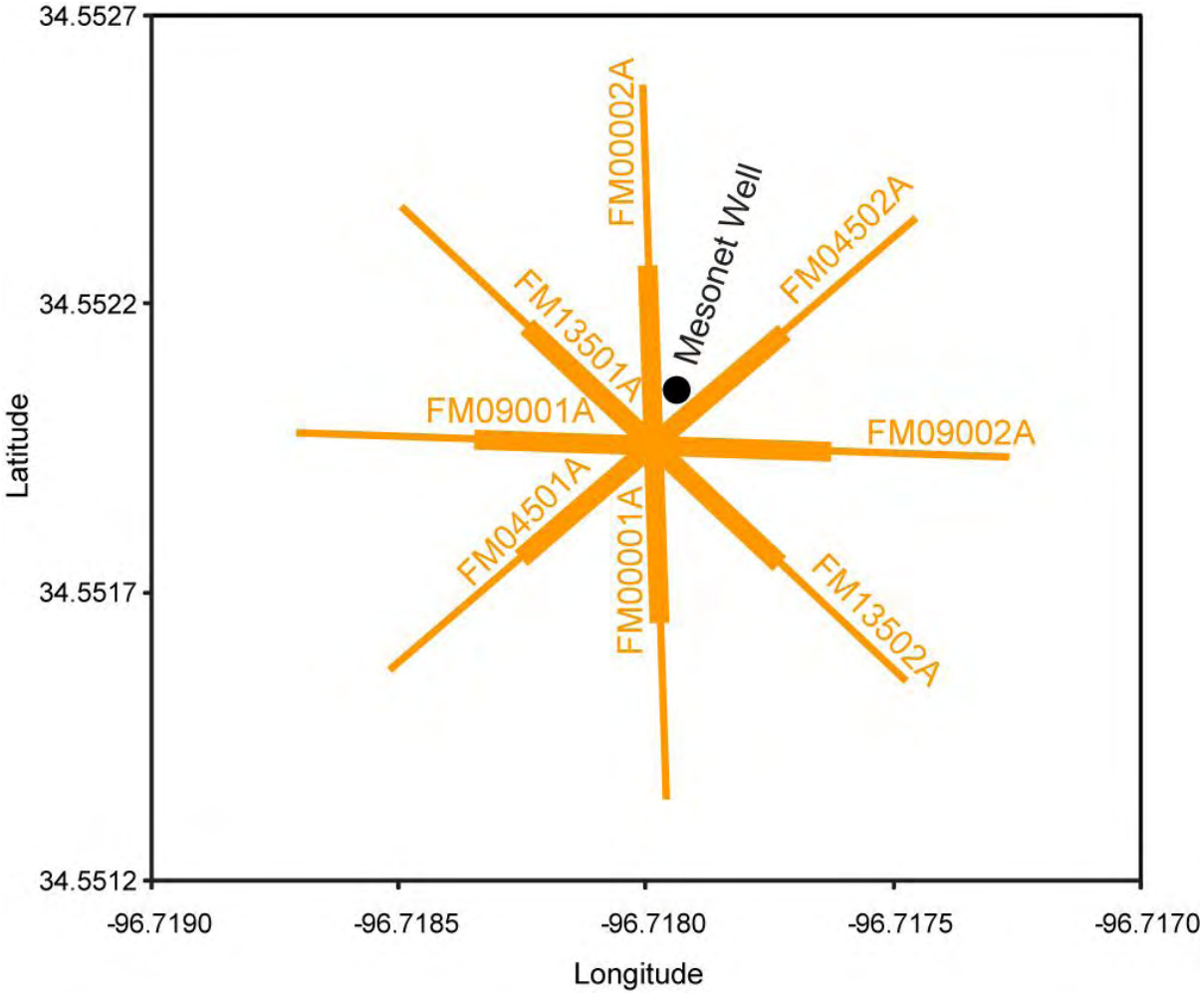

Figure A1.4. Fittstown mesonet site location map showing electrode line locations.

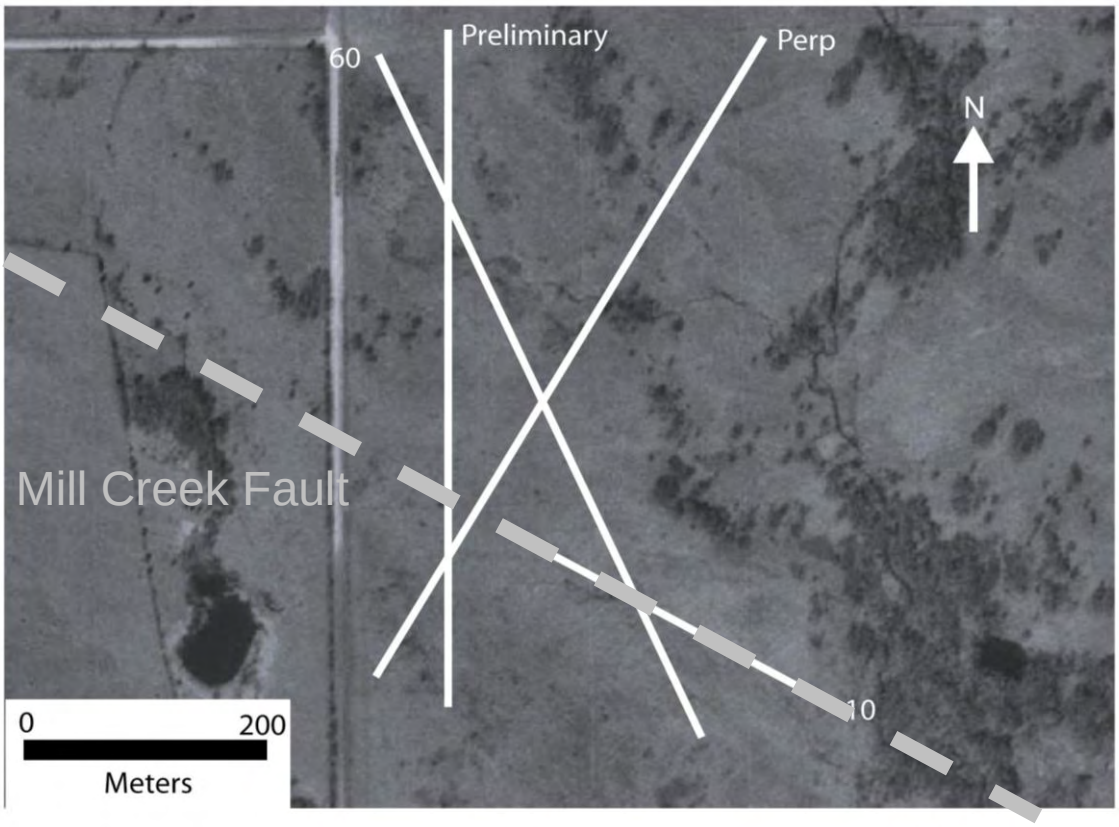

Figure A1.5. Hartman/Mill Creek Fault site location map with electrode line locations (from Riley, 2007). Aerial photo courtesy of USGS.

A)

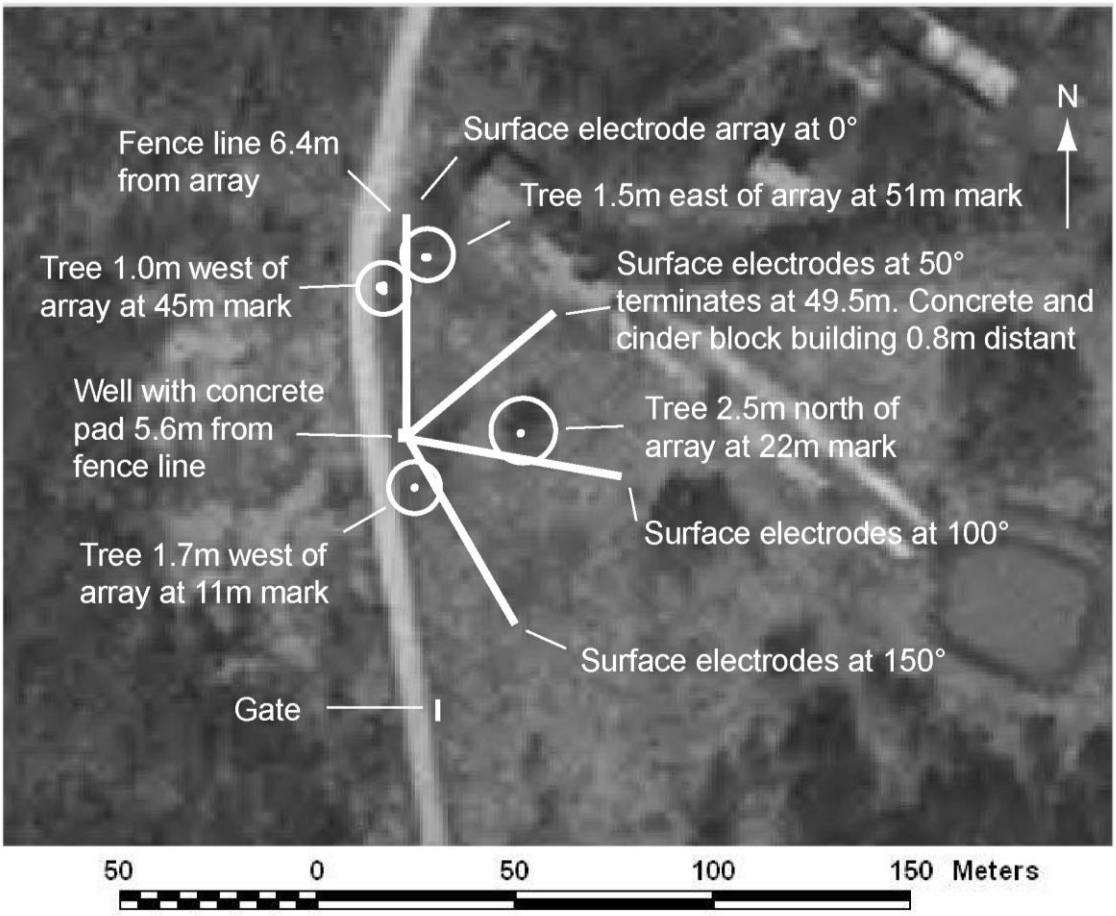

Figure A1.6A. Hatch Well Site with location of surface electrode placement and other line features noted (from Halihan et al, 2004). Aerial photo courtesy of USGS.

B)

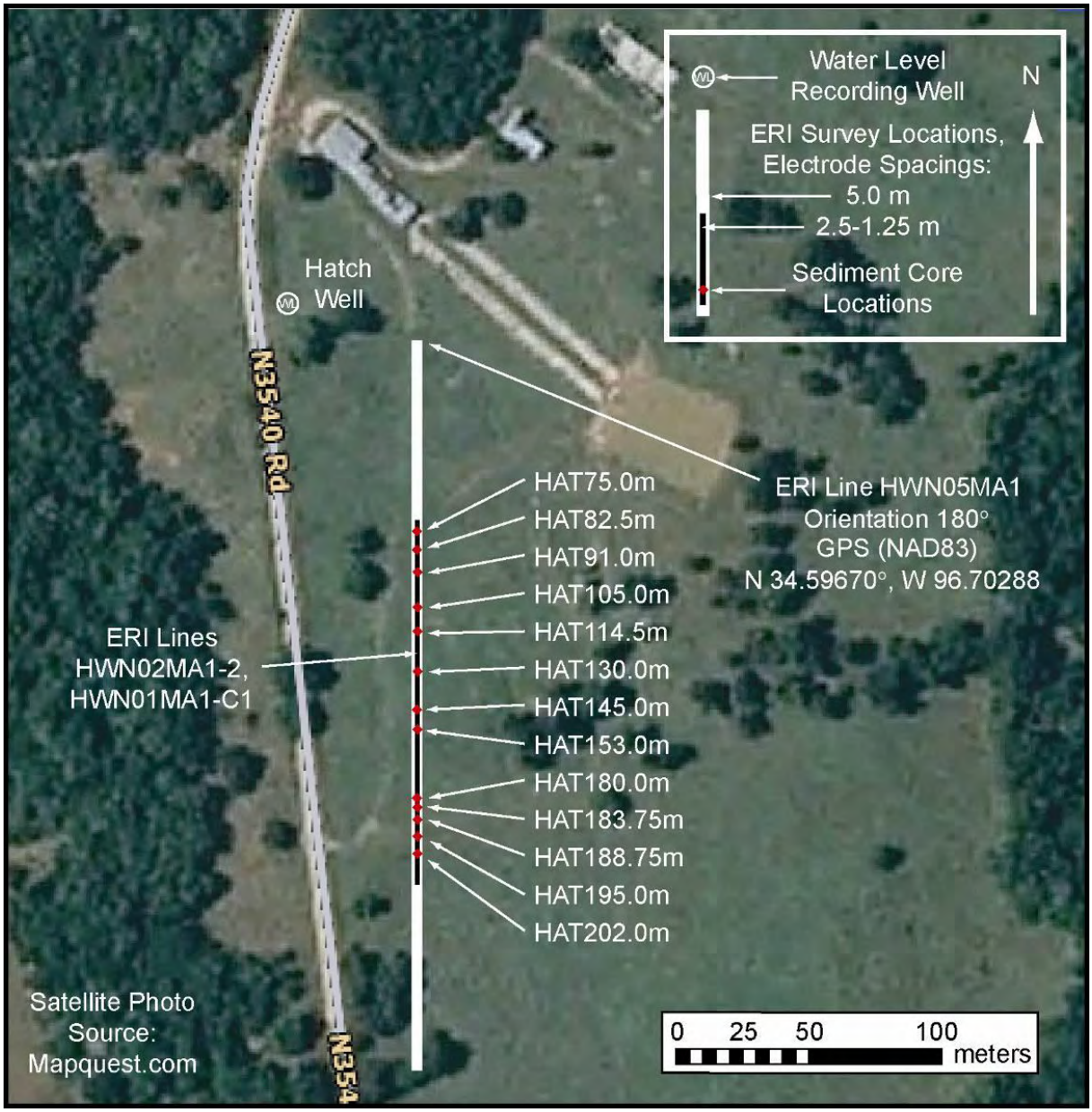

Figure A1.6B. Hatch site map with surface electrical resistivity, direct push, and well locations (from Sample, 2008). Aerial photo courtesy of Mapquest.

Figure A1.7. I-35 Mile Marker 49 site location showing the electrode line location (from Riley, 2007). Aerial photo courtesy of USGS.

A)

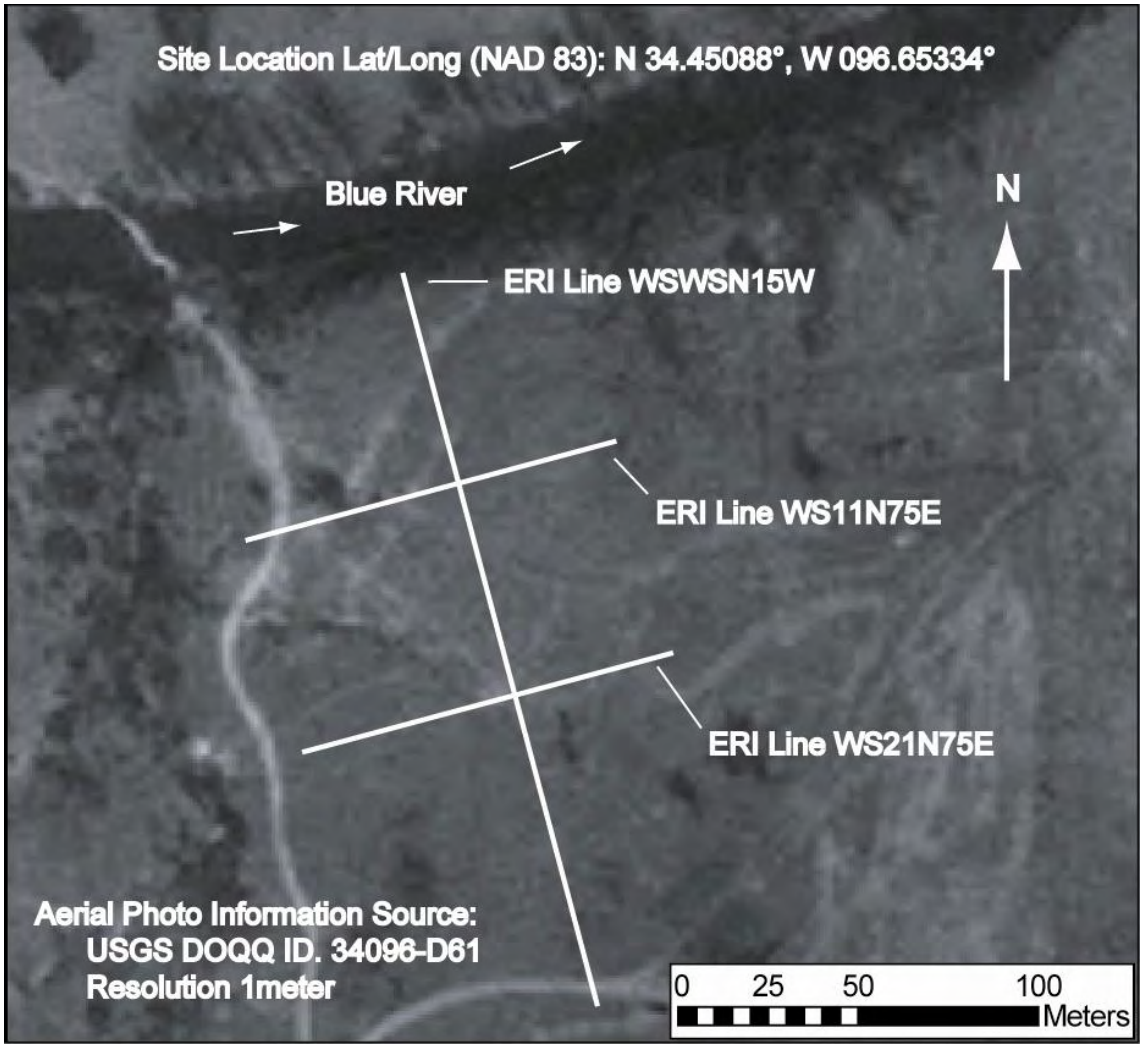

Figure A1.8A. Spears Ranch site map with surface electrical resistivity locations. Aerial photo courtesy of USGS.

B)

Figure A1.8B. Spears Ranch site map with surface electrical resistivity and direct push locations and well locations (from Sample, 2008). Aerial photo courtesy of Mapquest.

Figure A1.9. Unimin Quarry Site with location of surface electrode placement. Aerial photo courtesy of USGS.

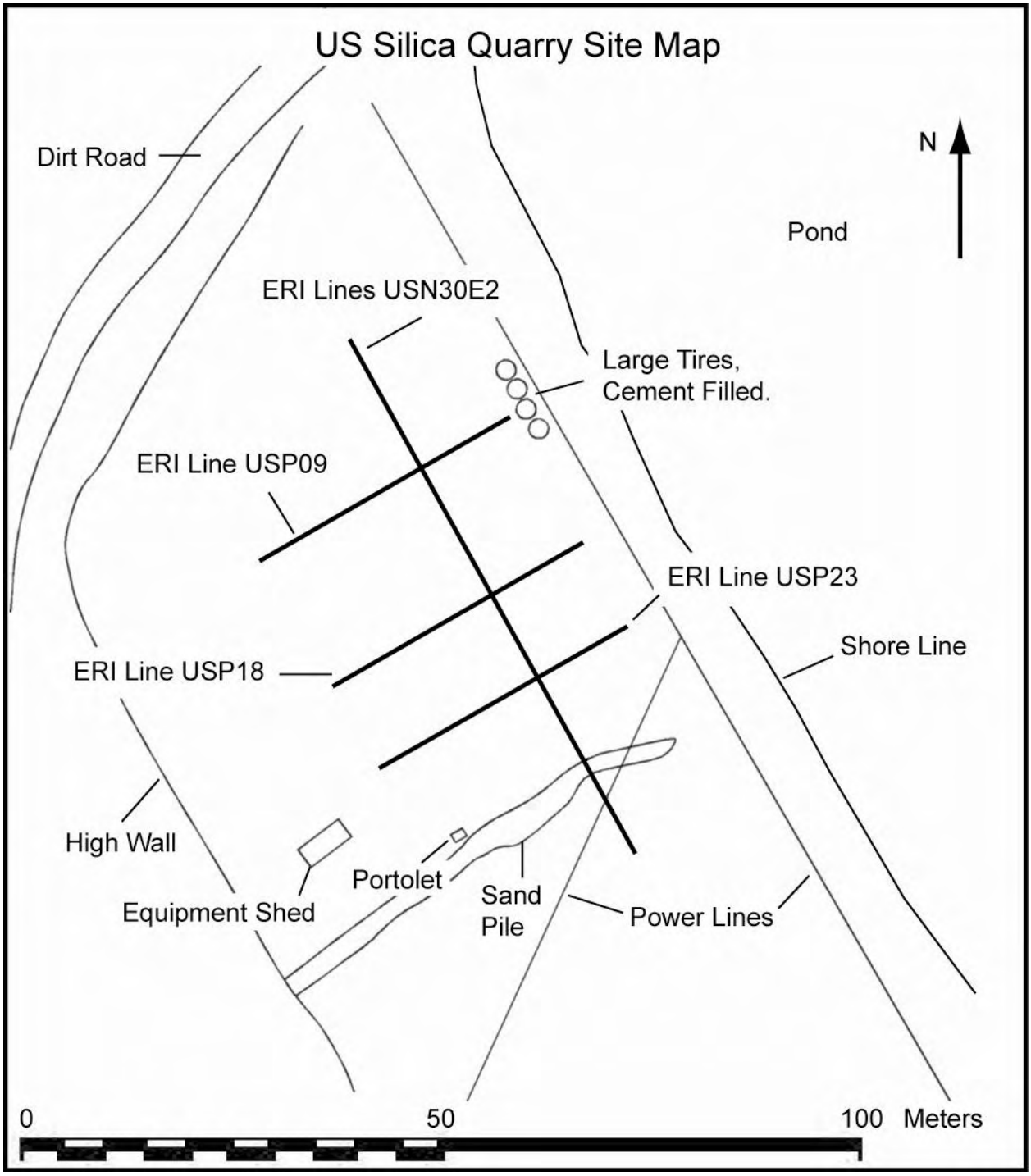

Figure A1.10. U.S. Silica Quarry Site with location of surface electrode placement.

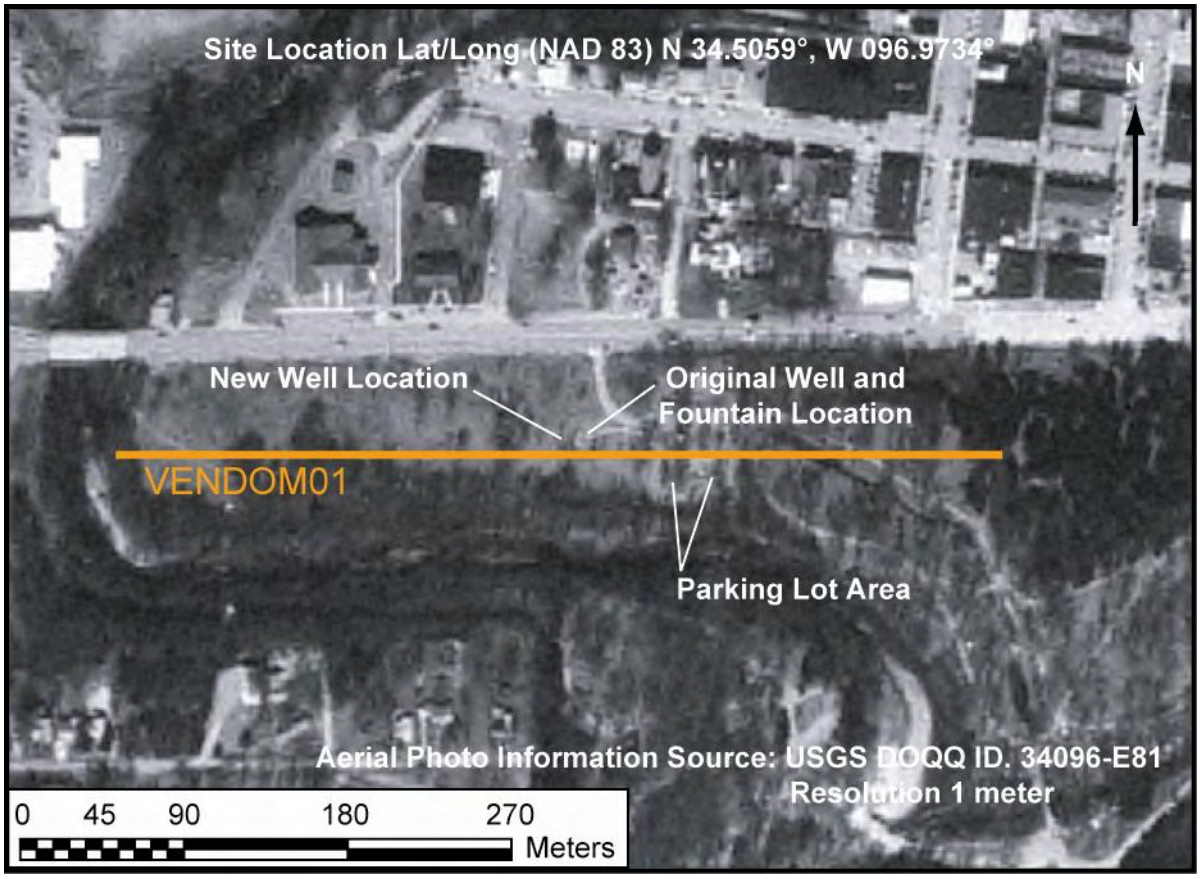

Figure A1.11. Vendome Well Site with location of surface electrode placement and wells. Aerial photo courtesy of USGS.

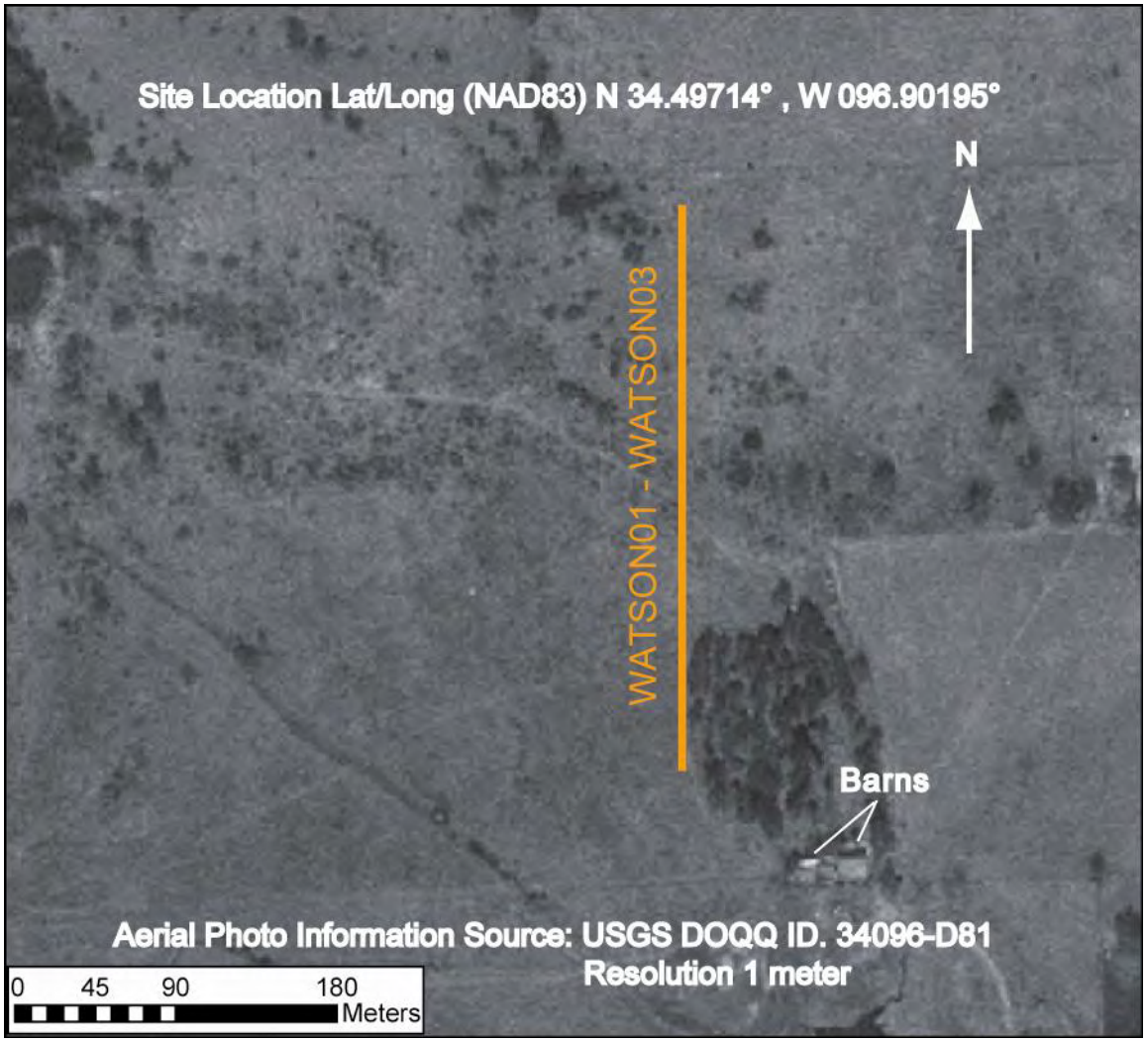

Figure A1.12. Watson/Sulphur Fault Site with location of surface electrode placement. Aerial photo courtesy of USGS.

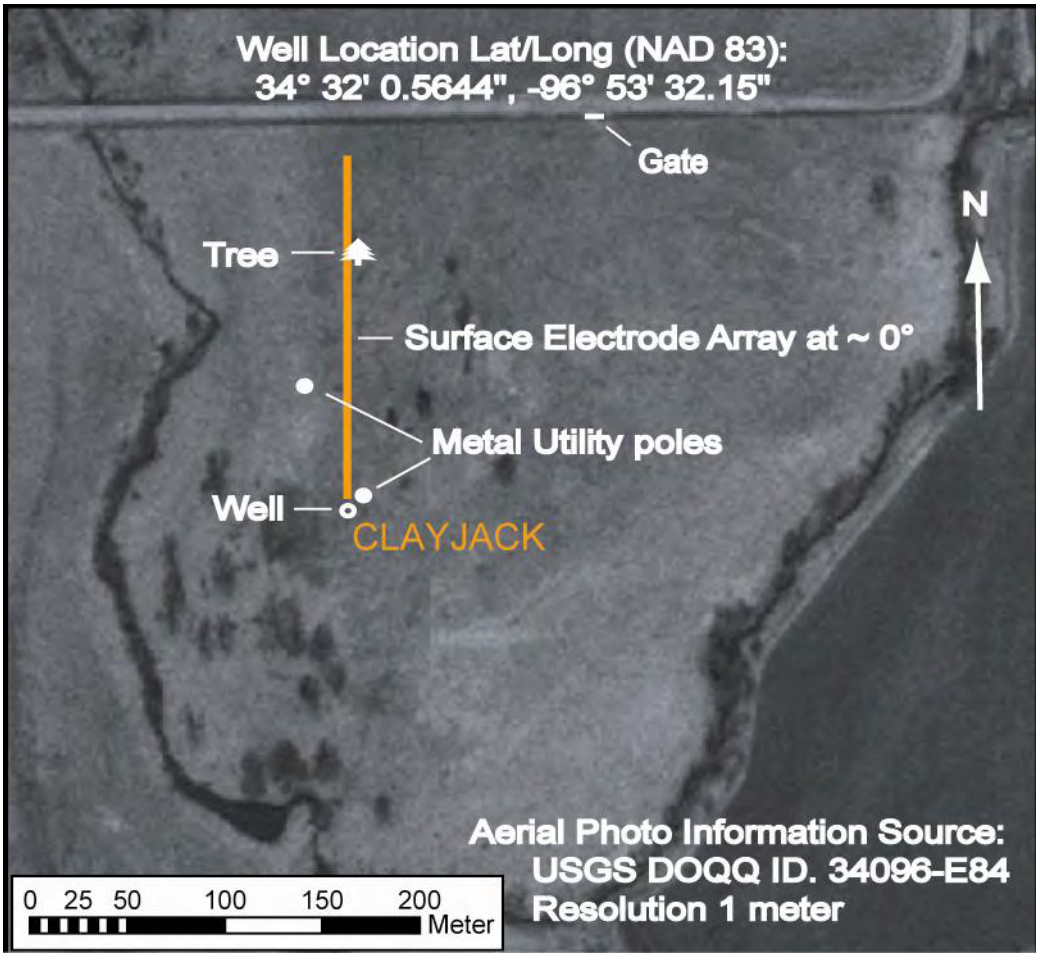

Figure A1.13. Clay Jack Well Site with location of surface electrode placement and well. Aerial photo courtesy of USGS.

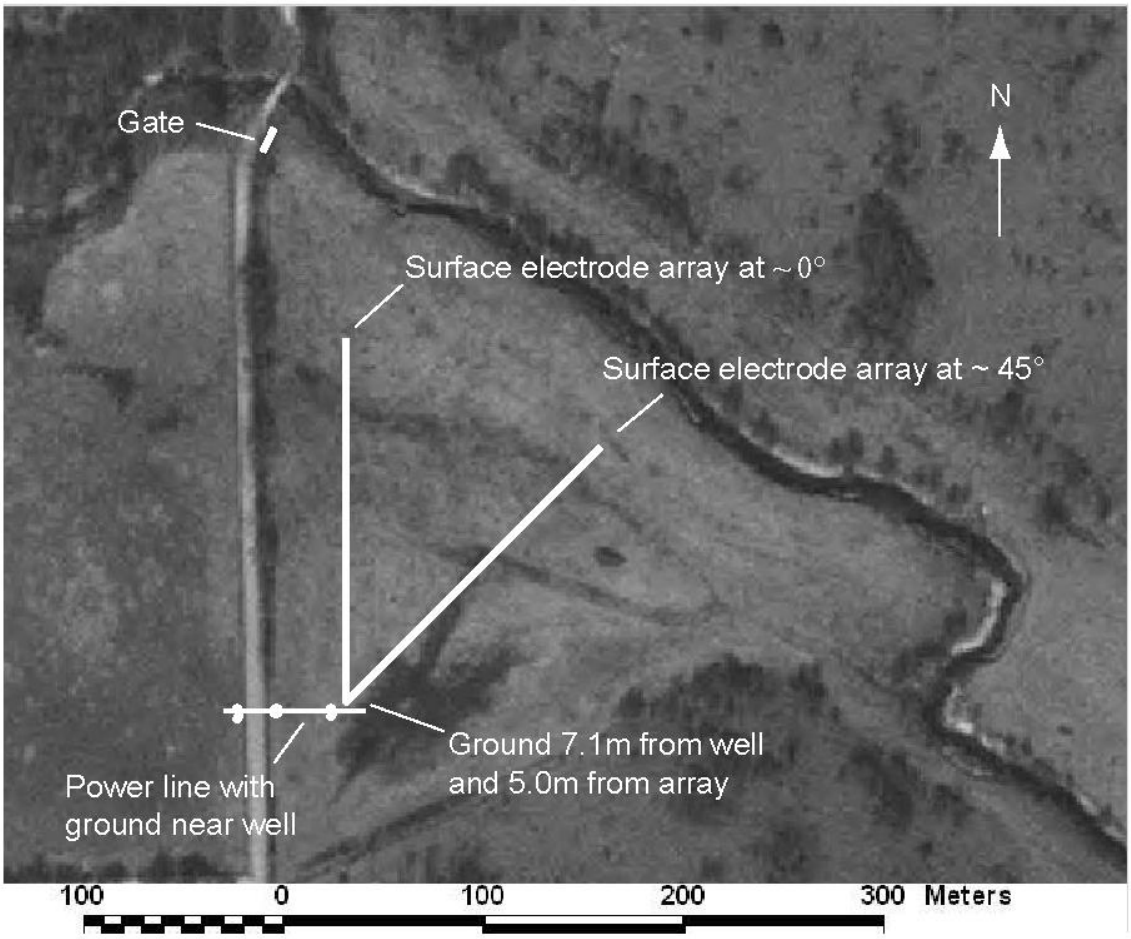

Figure A1.14. Wingard 2 Well Site with location of surface electrode placement and other line features noted (from Halihan et al, 2004). Aerial photo courtesy of USGS.

Appendix 2

ERI Images

SITE: Arbuckle-Simpson Ranch

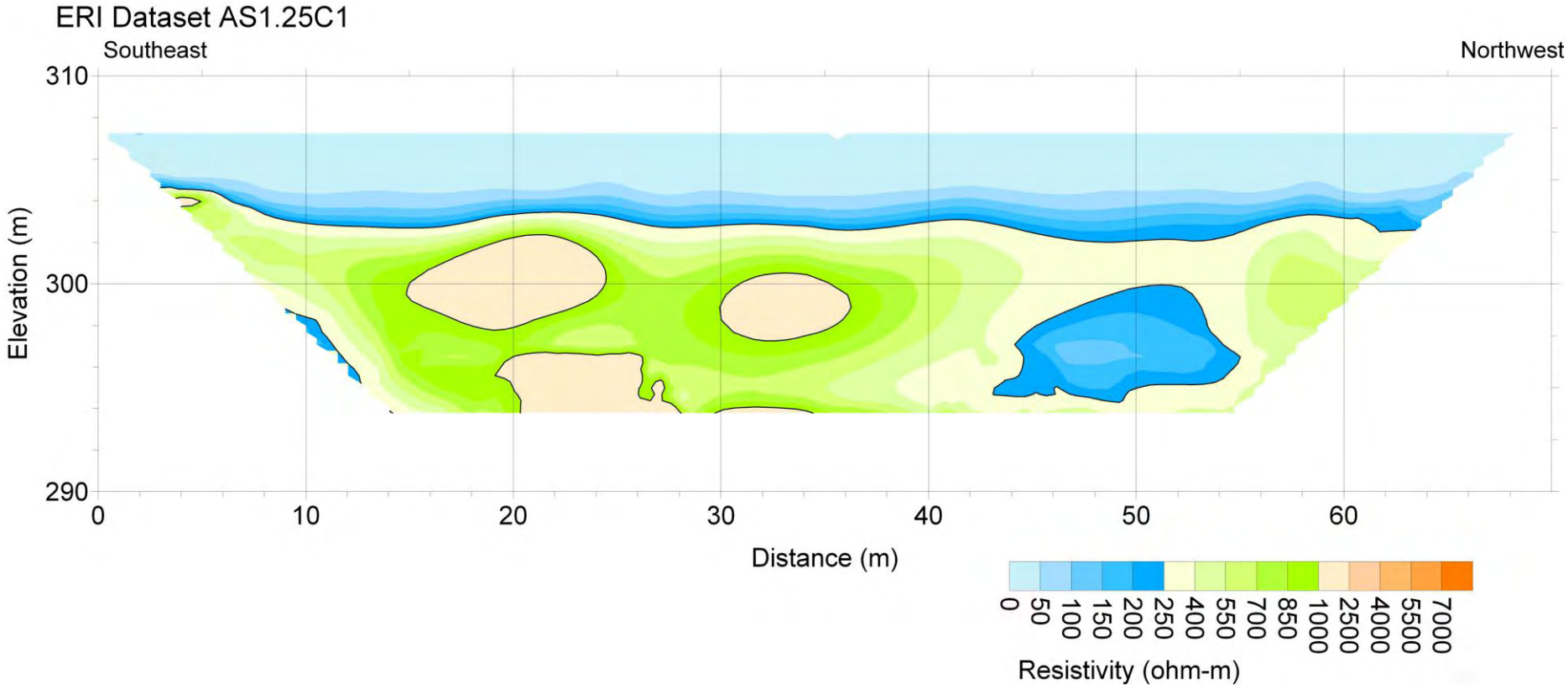

Figure A2.1. ERI Line AS1.25C1.

SITE: Arbuckle-Simpson Ranch

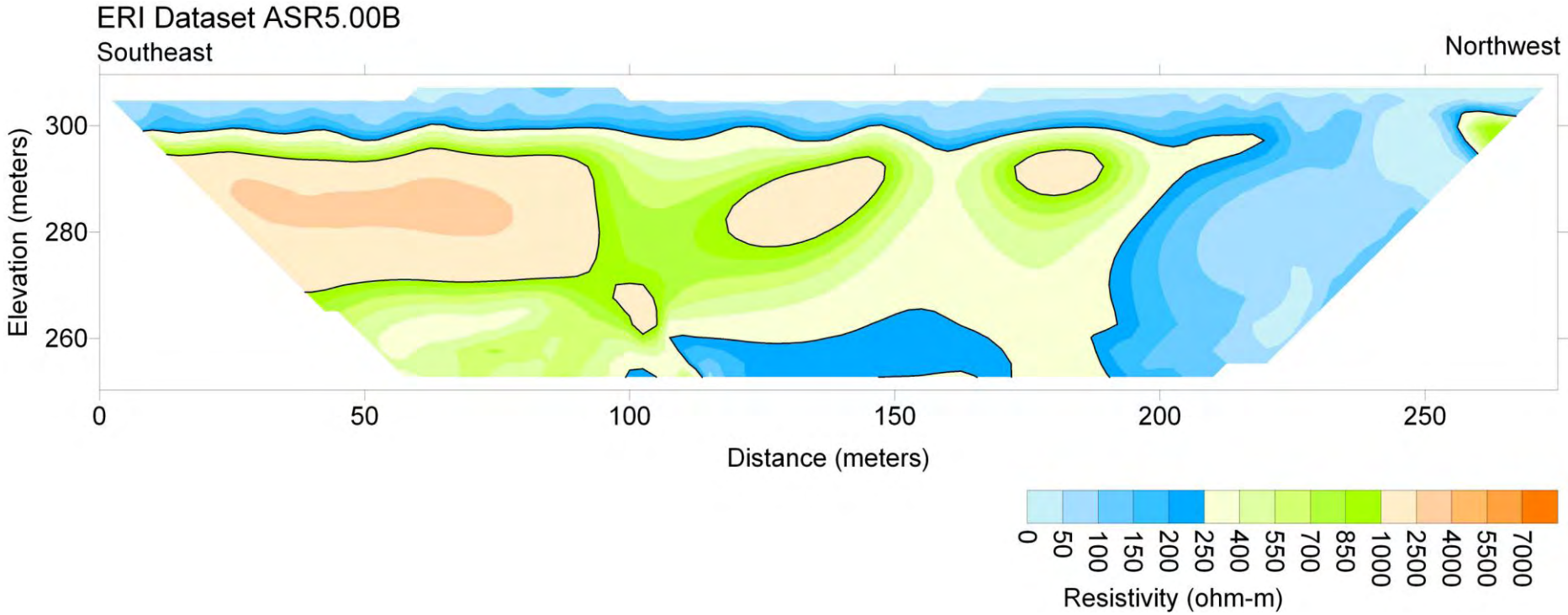

Figure A2.2. ERI Line ASR5.00B.

SITE: Arbuckle-Simpson Ranch

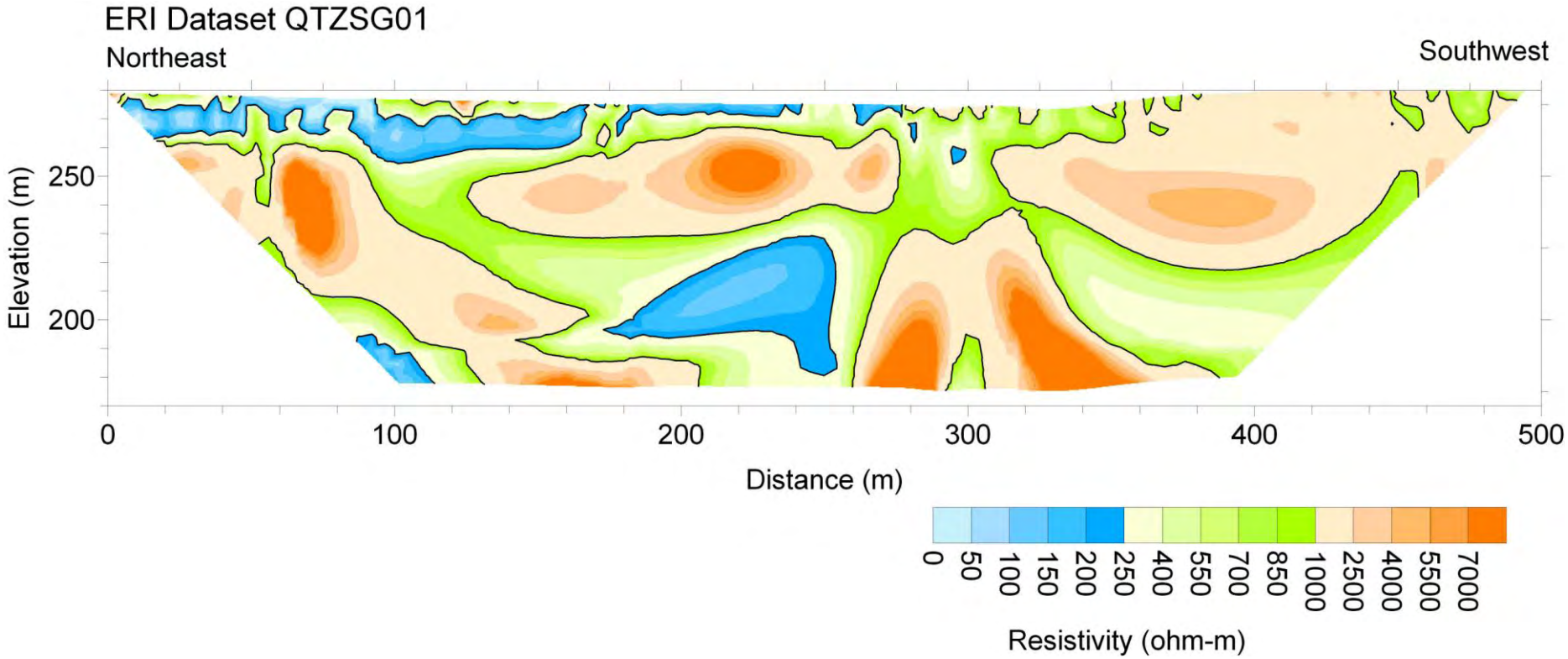

Figure A2.3. ERI Line QTZSG01.

SITE: Arbuckle-Simpson Ranch

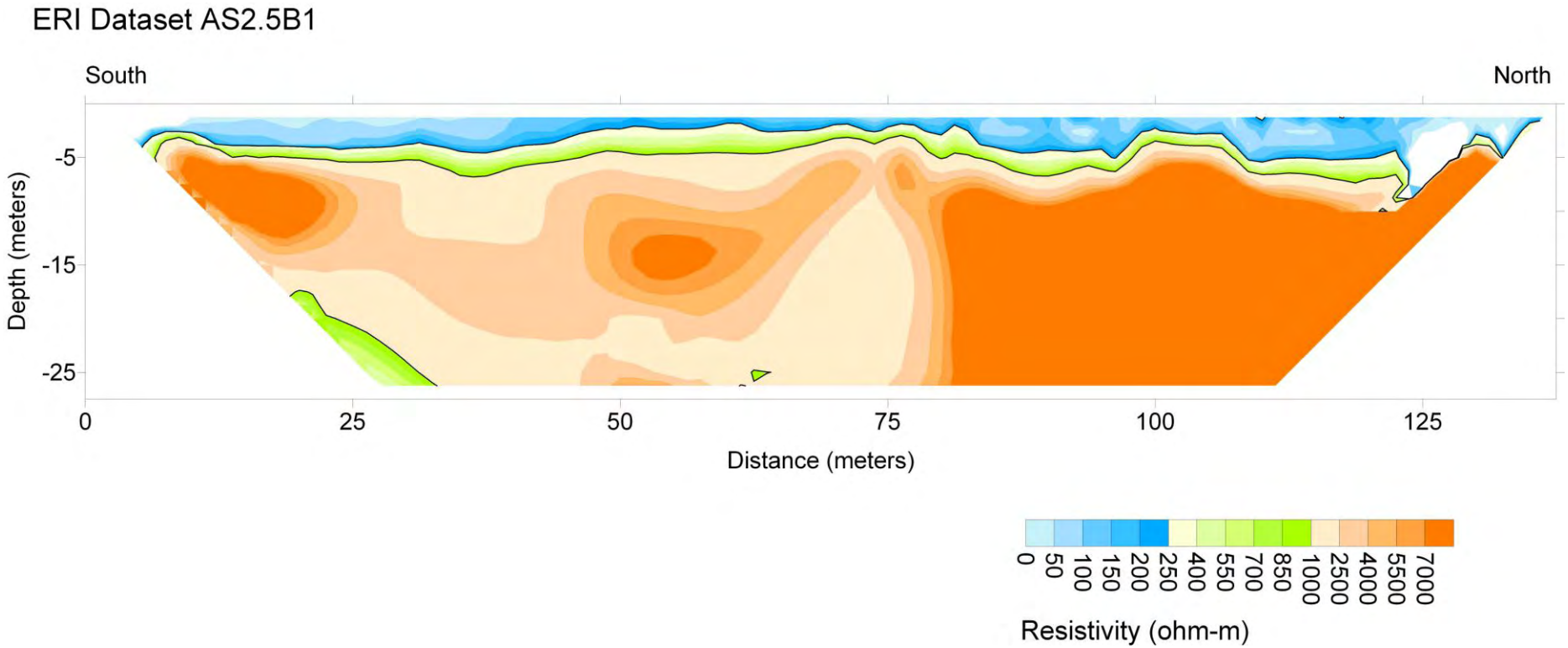

Figure A2.4. ERI Line AS2.5B1.

SITE: Arbuckle-Simpson Ranch

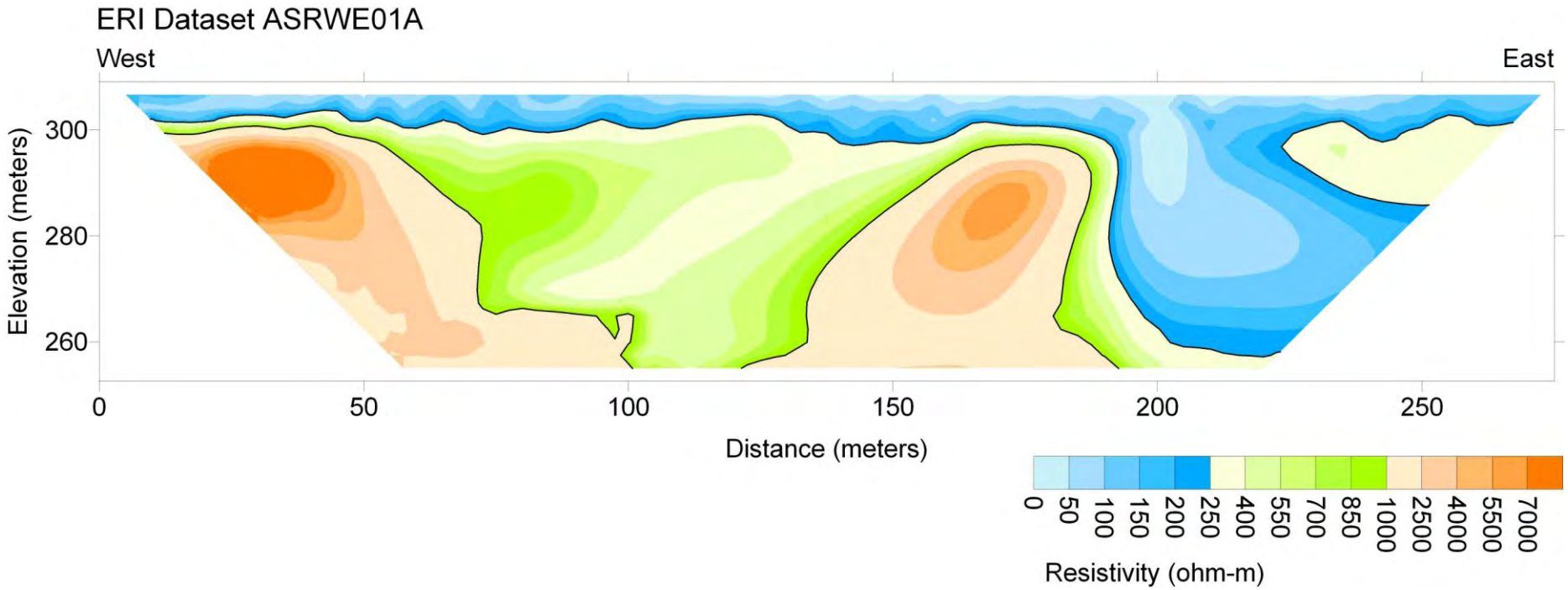

Figure A2.5. ERI Line ASRWE01A.

SITE: Clement Springs

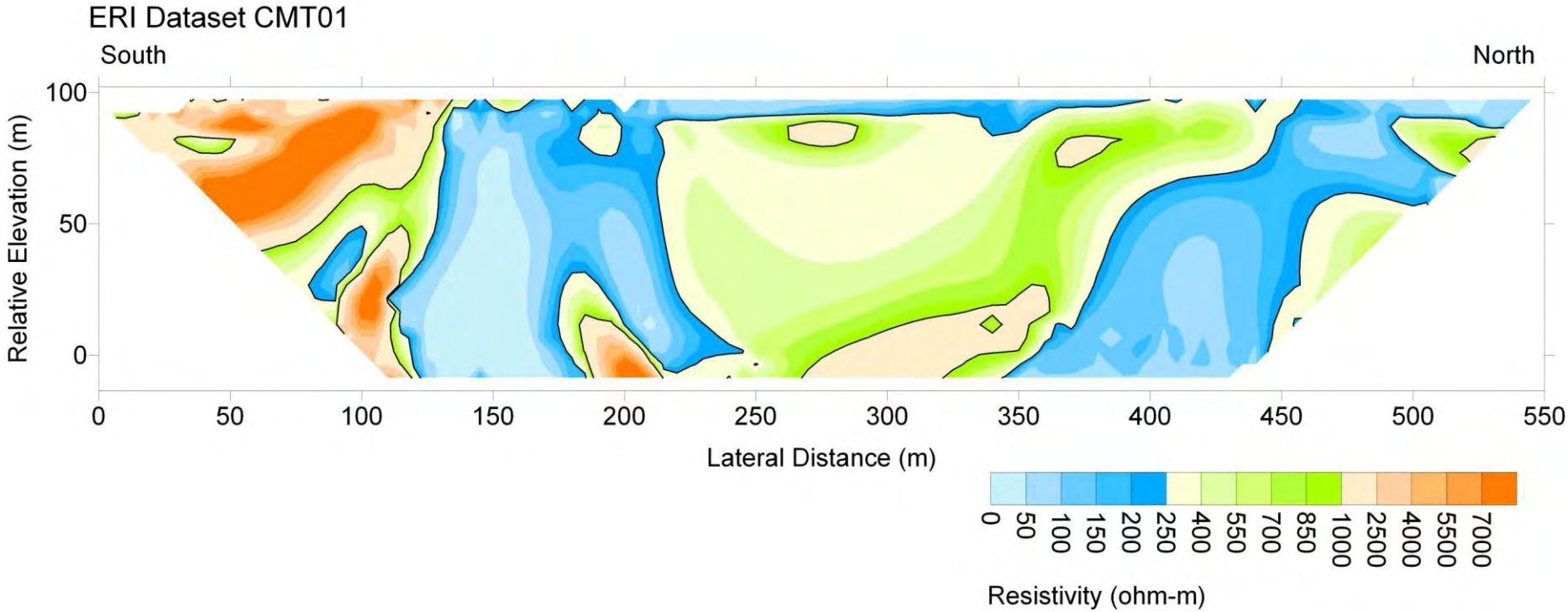

Figure A2.6. ERI Line CMT01.

SITE: Clement Springs

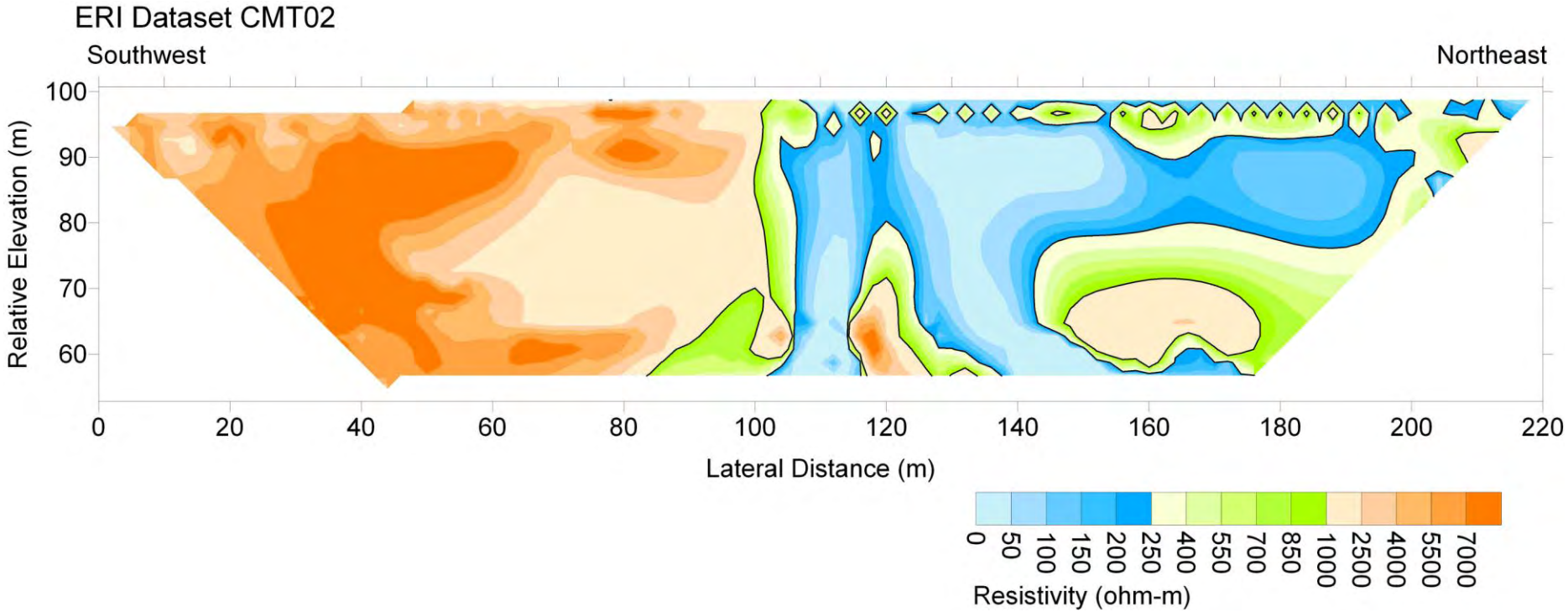

Figure A2.7. ERI Line CMT02.

SITE: Devil's Den

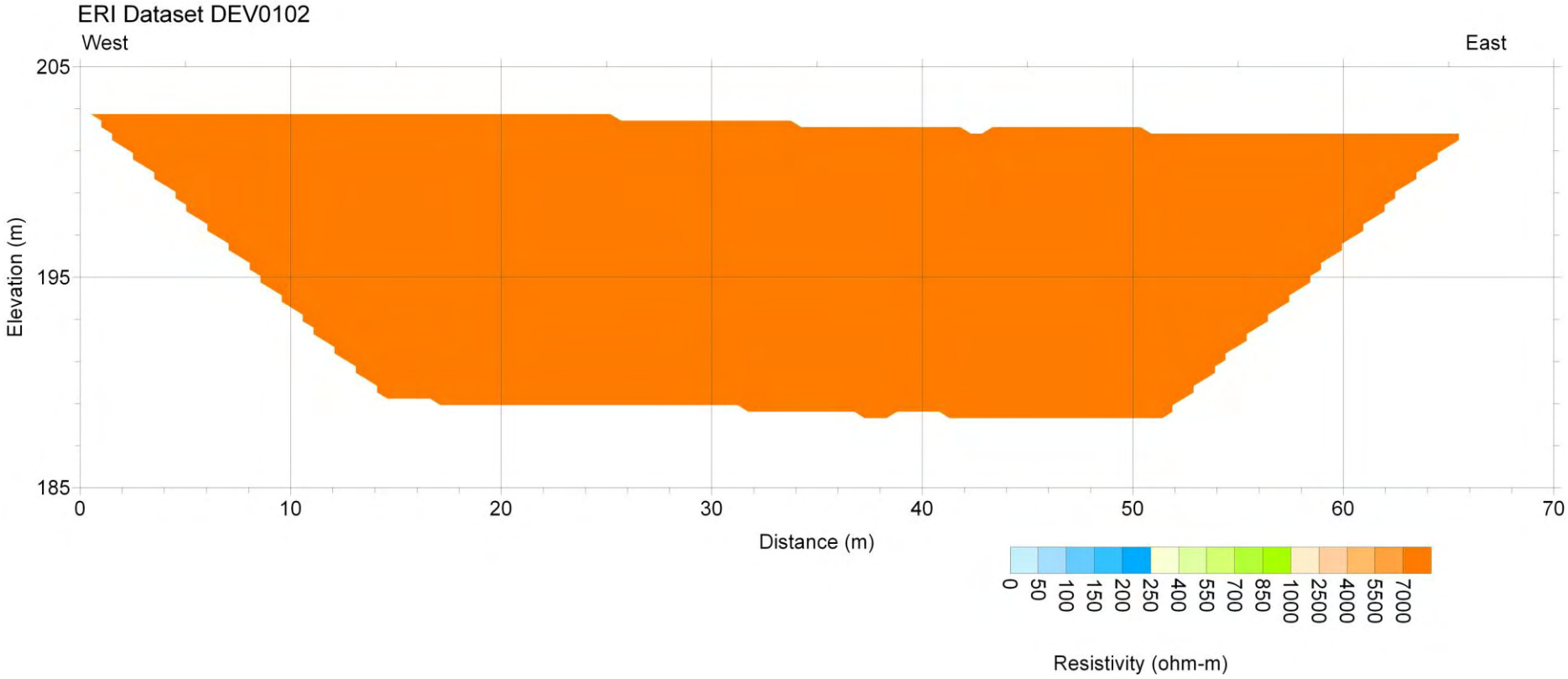

Figure A2.8. ERI Lines DEV01 and DEV02.

SITE: Devil's Den

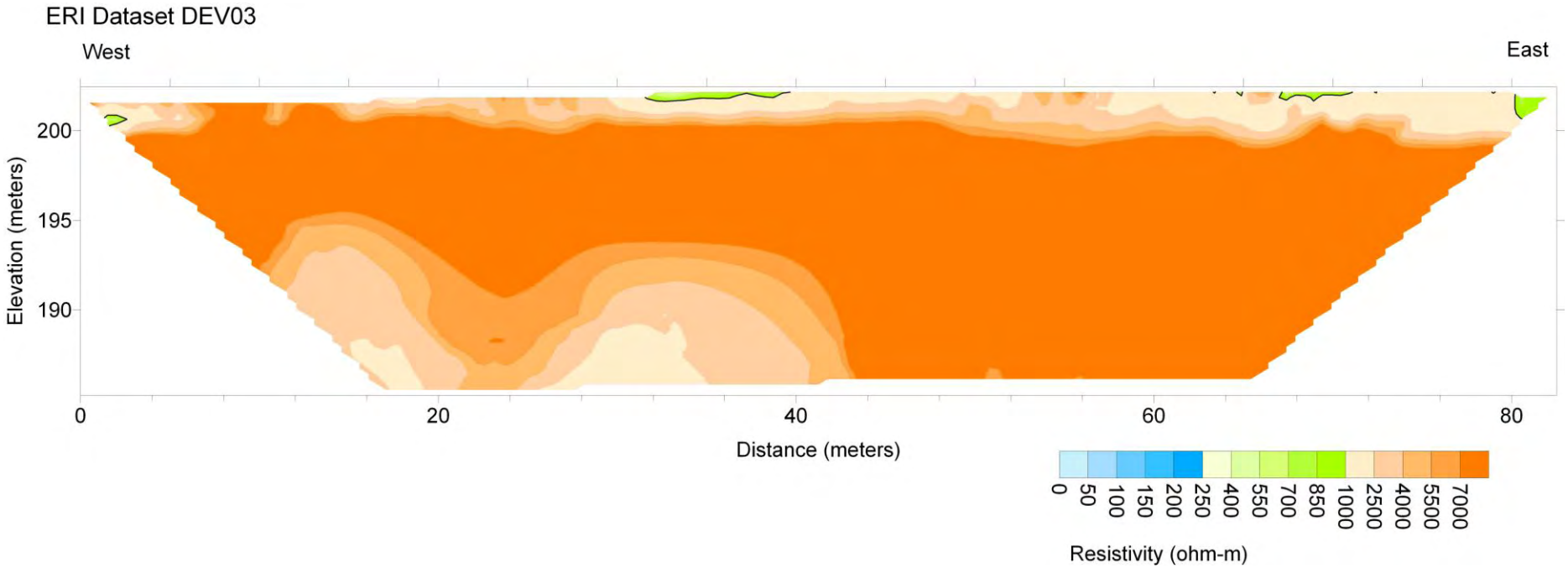

Figure A2.9. ERI Line DEV03.

SITE: Fittstown Mesonet

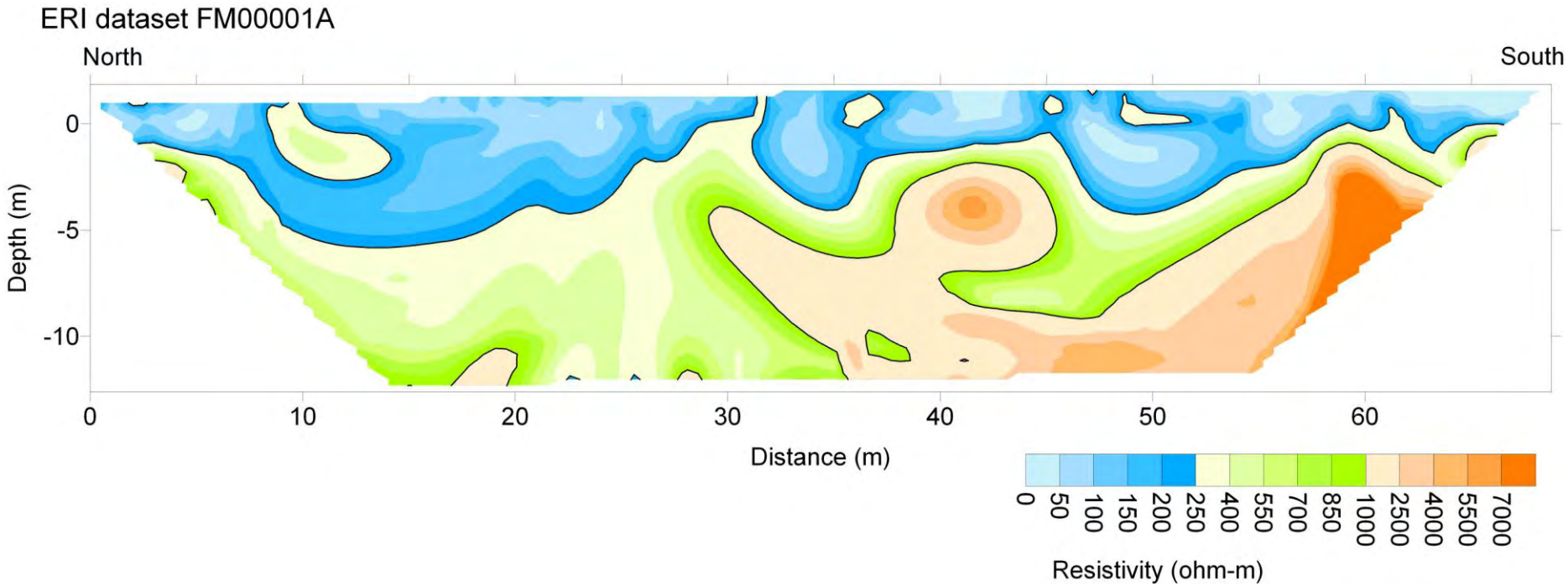

Figure A2.10. ERI Line FM00001A.

SITE: Fittstown Mesonet

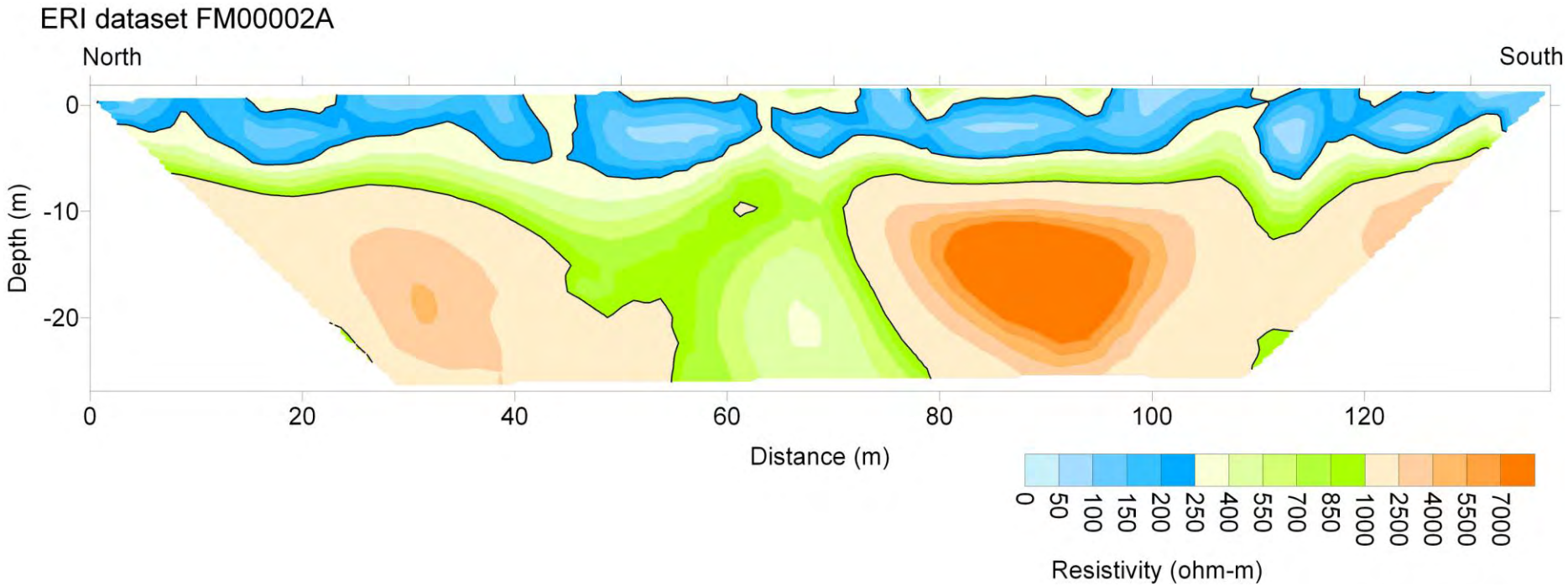

Figure A2.11. ERI Line FM00002A.

SITE: Fittstown Mesonet

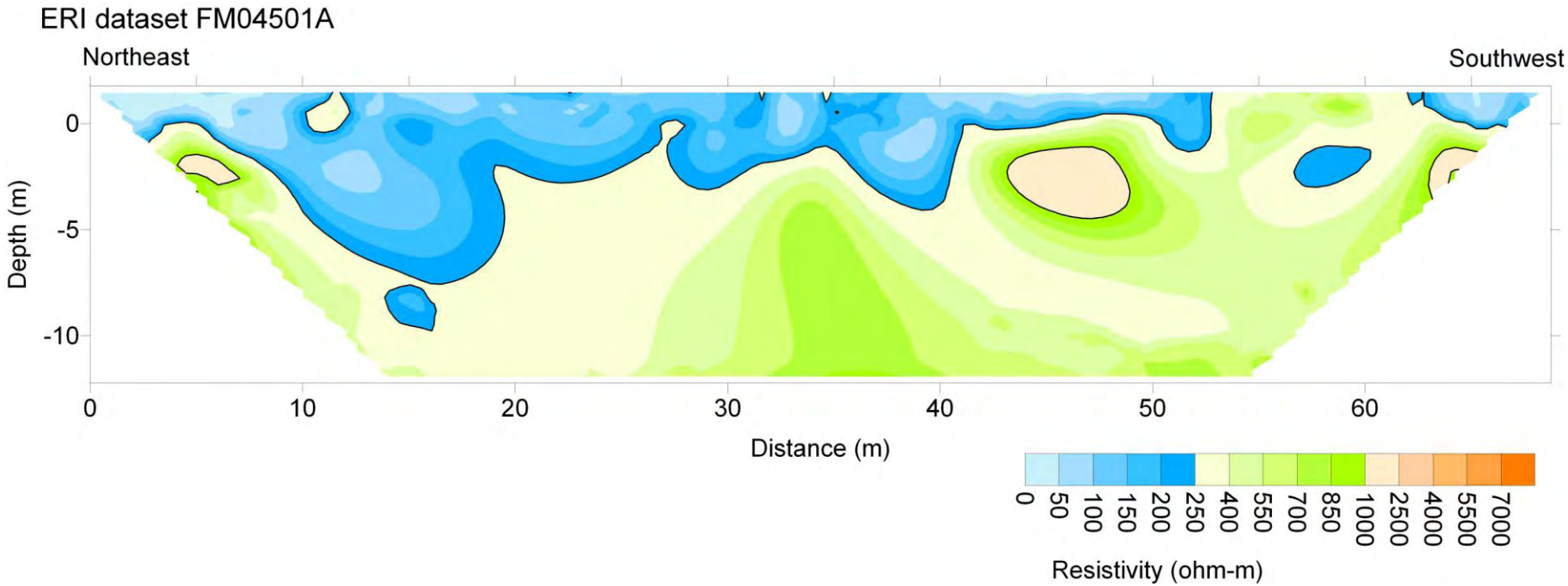

Figure A2.12. ERI Line FM04501A.

SITE: Fittstown Mesonet

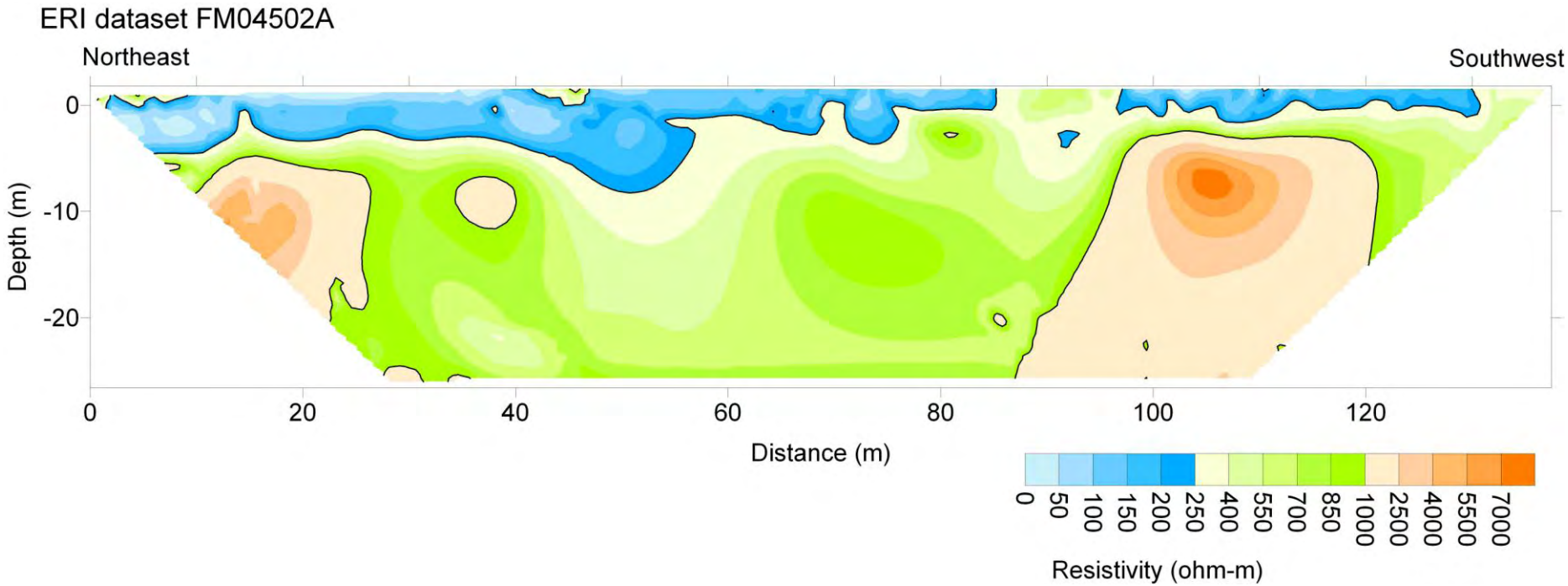

Figure A2.13. ERI Line FM04502A.

SITE: Fittstown Mesonet

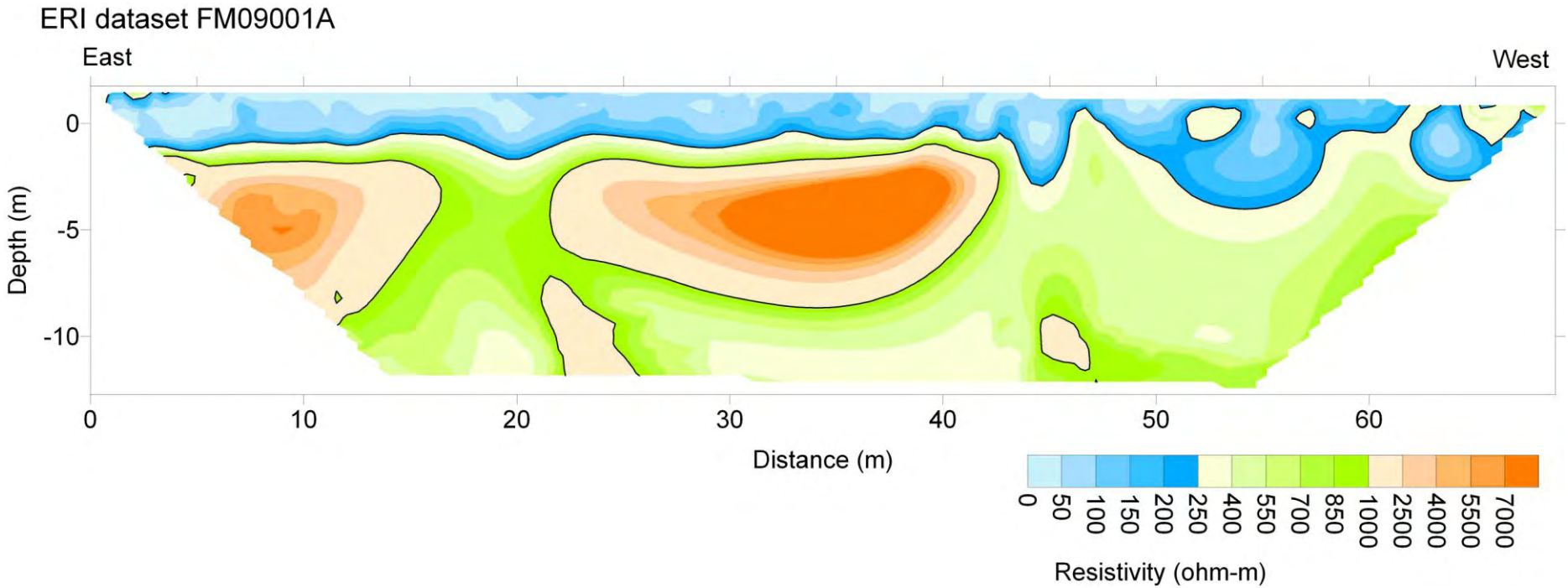

Figure A2.14. ERI Line FM09001A.

SITE: Fittstown Mesonet

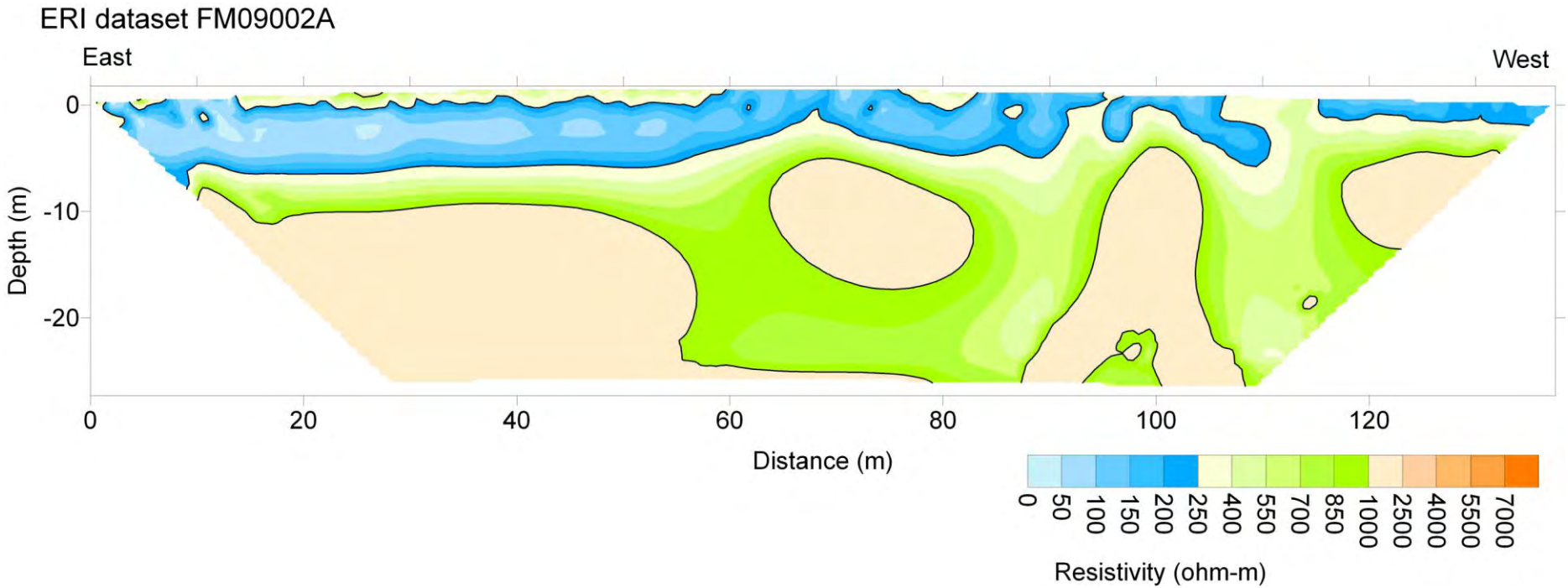

Figure A2.15. ERI Line FM09002A.

SITE: Fittstown Mesonet

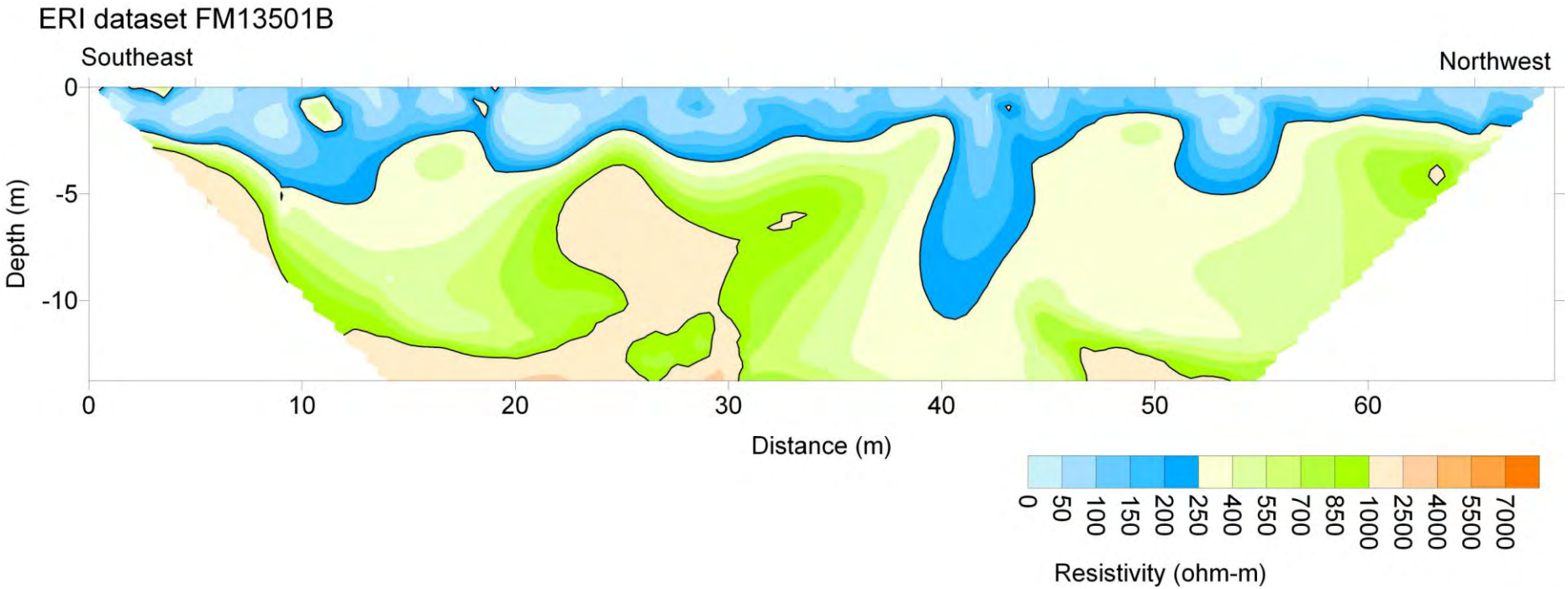

Figure A2.16. ERI Line FM13501B.

SITE: Fittstown Mesonet

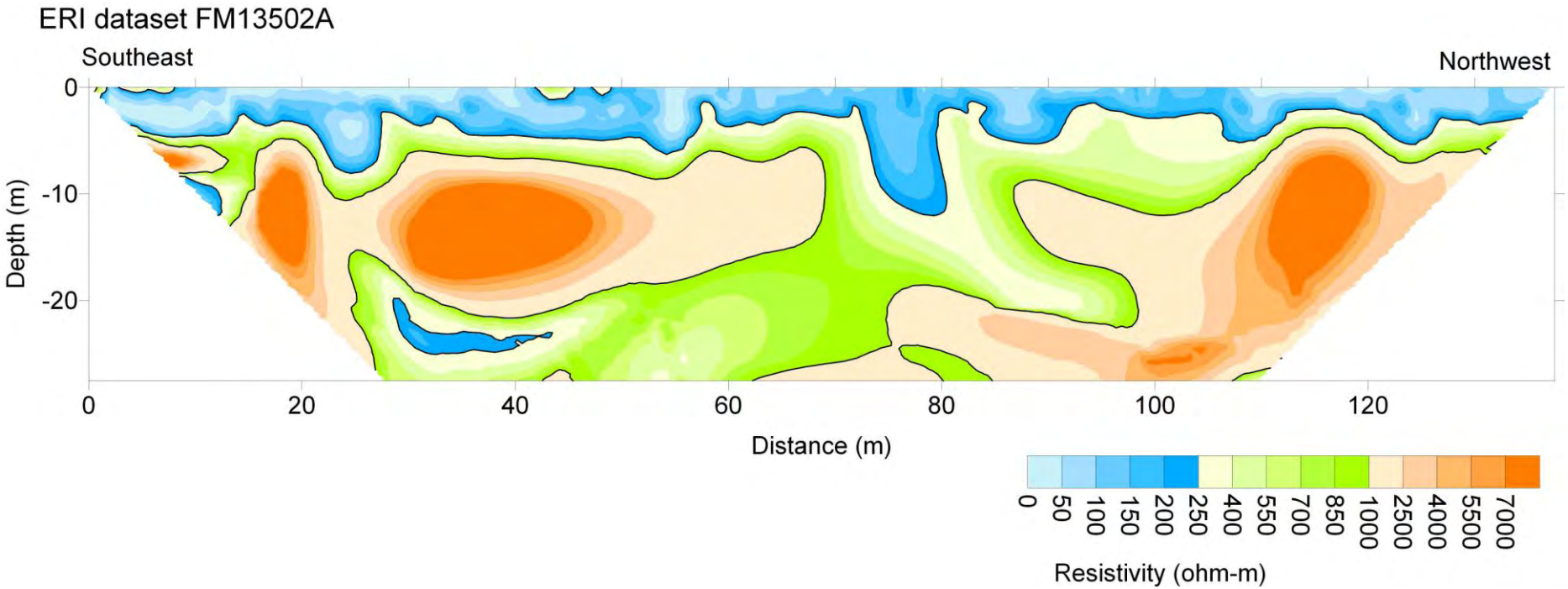

Figure A2.17. ERI Line FM13502A.

SITE: Hartman/Mill Creek Fault

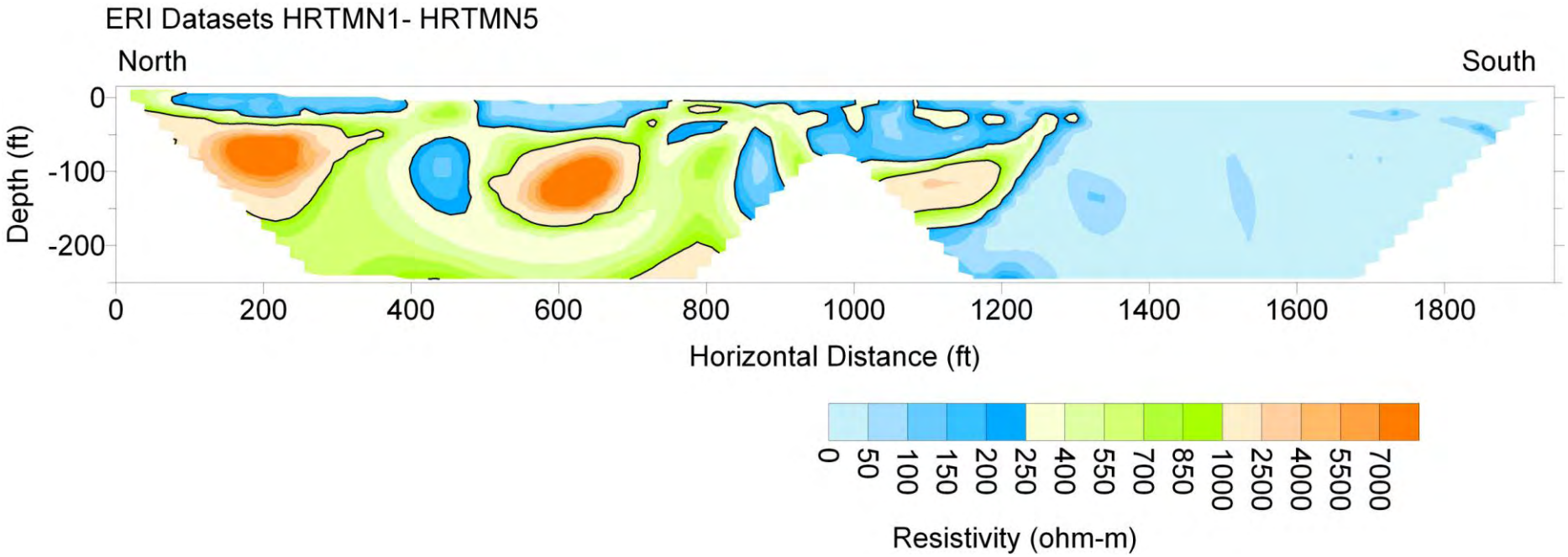

Figure A2.18. ERI Lines HRTMN1-HRTMN5.

SITE: Hartman/Mill Creek Fault

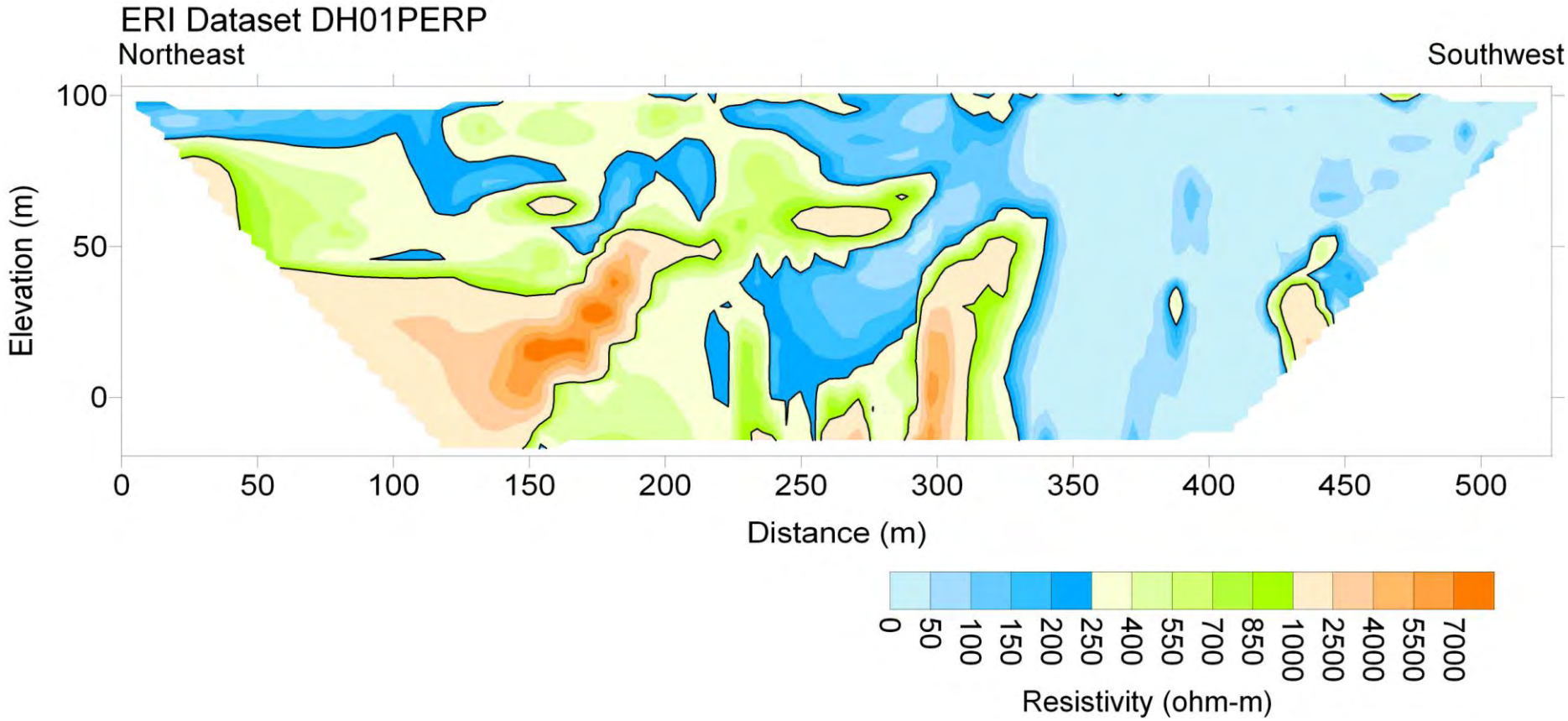

Figure A2.19. ERI Line DH01PERP.

SITE: Hartman/Mill Creek Fault

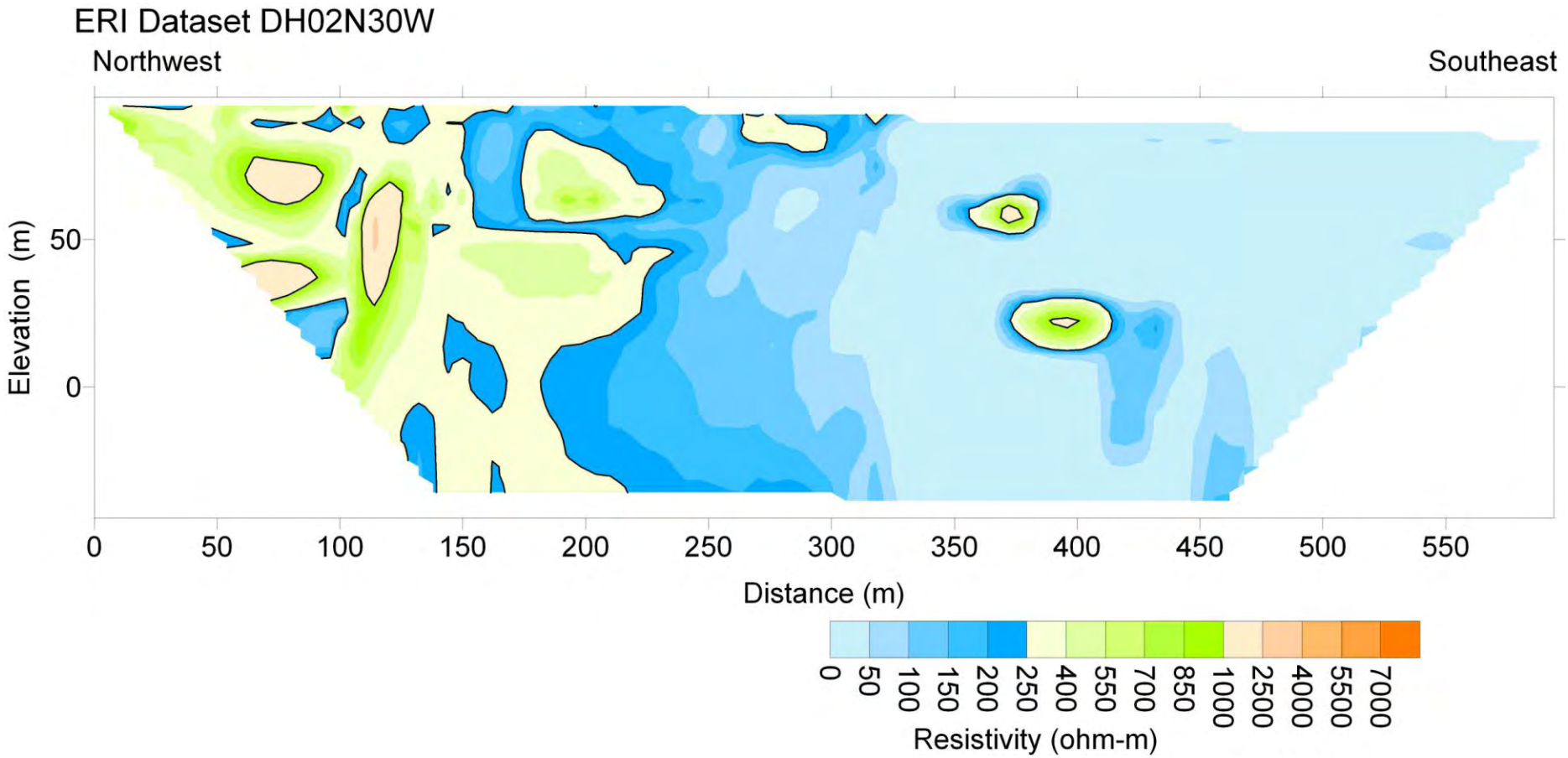

Figure A2.20. ERI Line DH02N30W.

SITE: Hartman/Mill Creek Fault

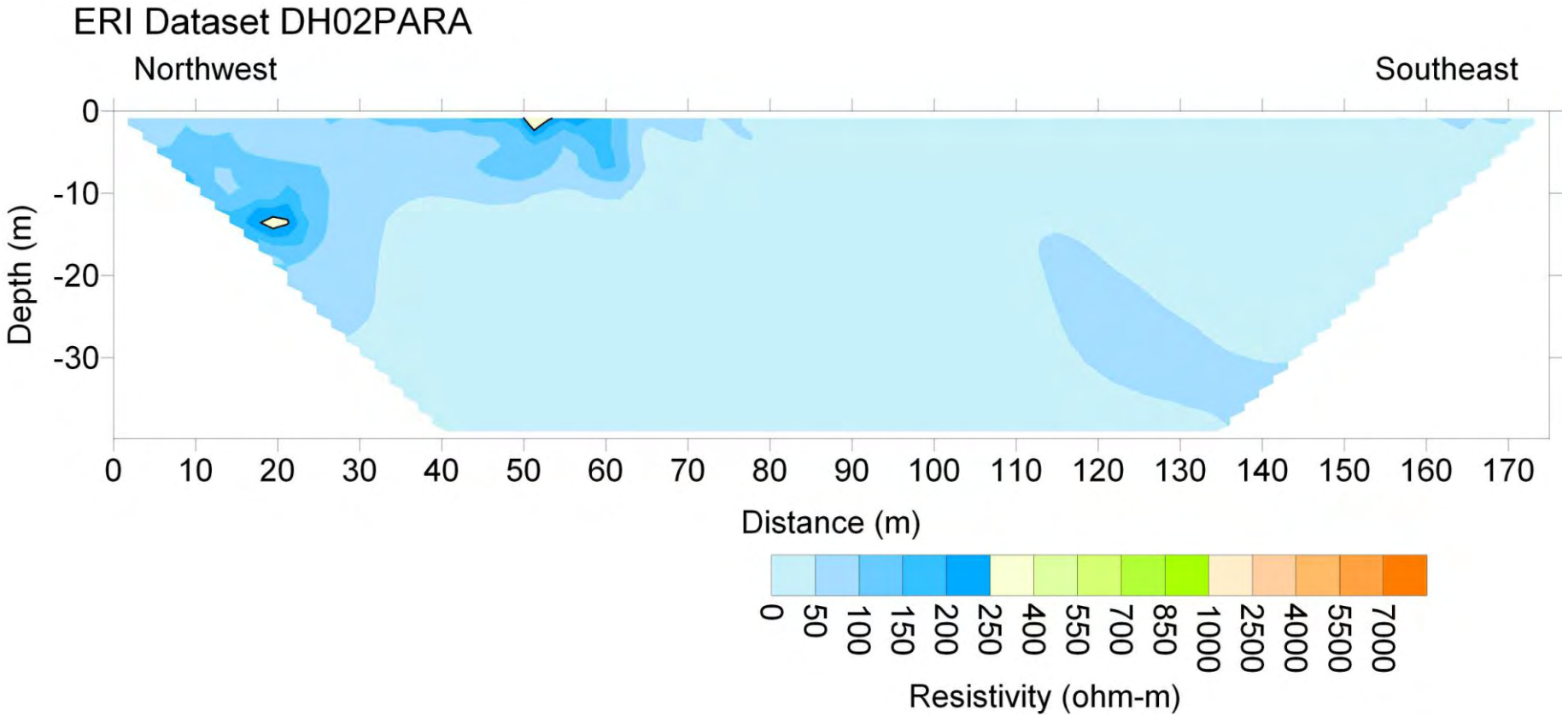

Figure A2.21. ERI Line DH02PARA.

SITE: Hatch Well Site

A)

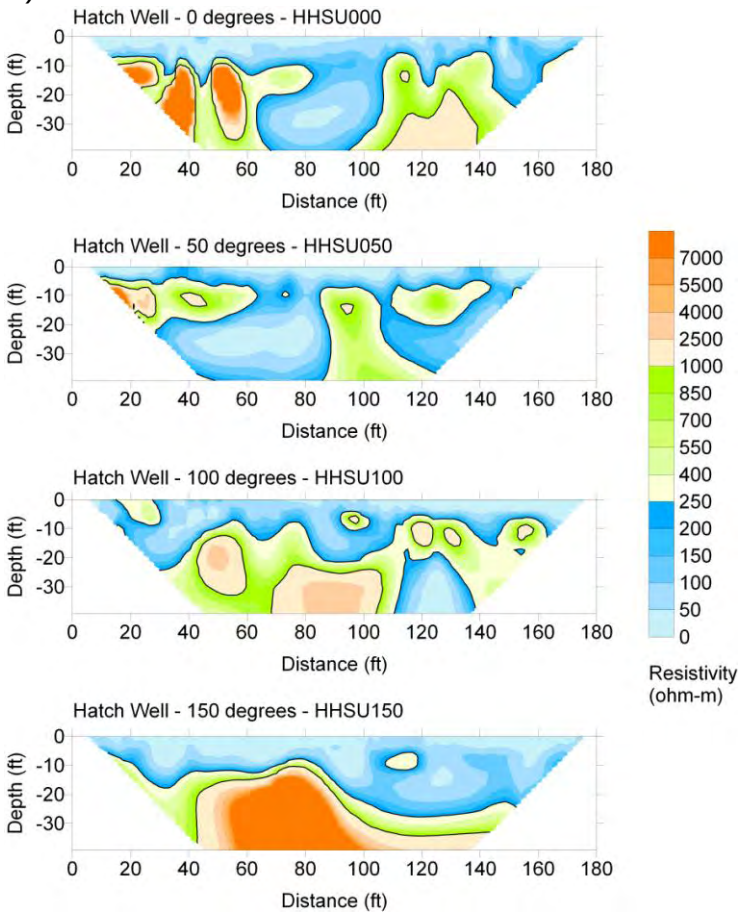

B)

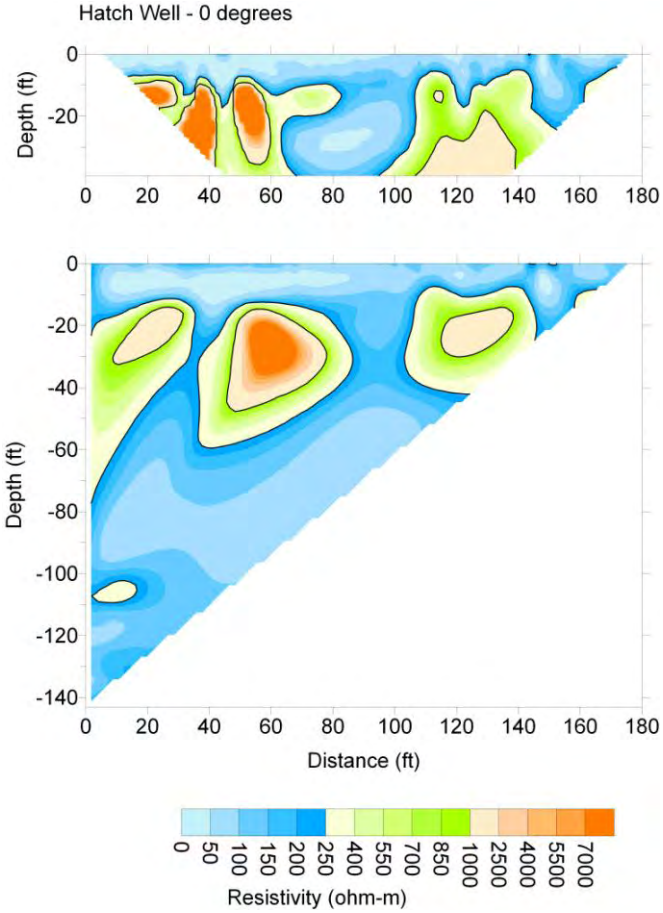

Figure A2.22. A) ERI Lines HHSU000, HHSU050, HHSU100, HHSU150. B)ERI Line HHSU000 + BERI borehole data

SITE: Hatch Well Site

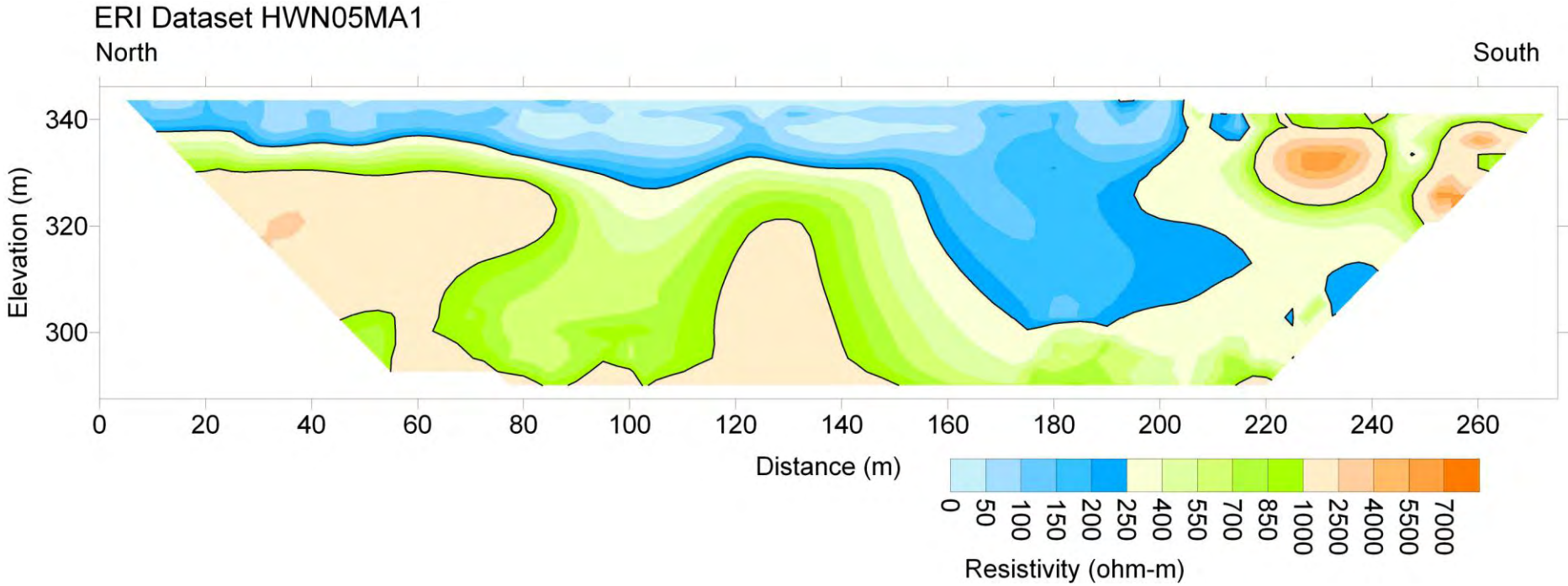

Figure A2.23. ERI Line HWN05MA1. This is the same location as files 31-35 (HWN0* series).

SITE: I-35 Overlook

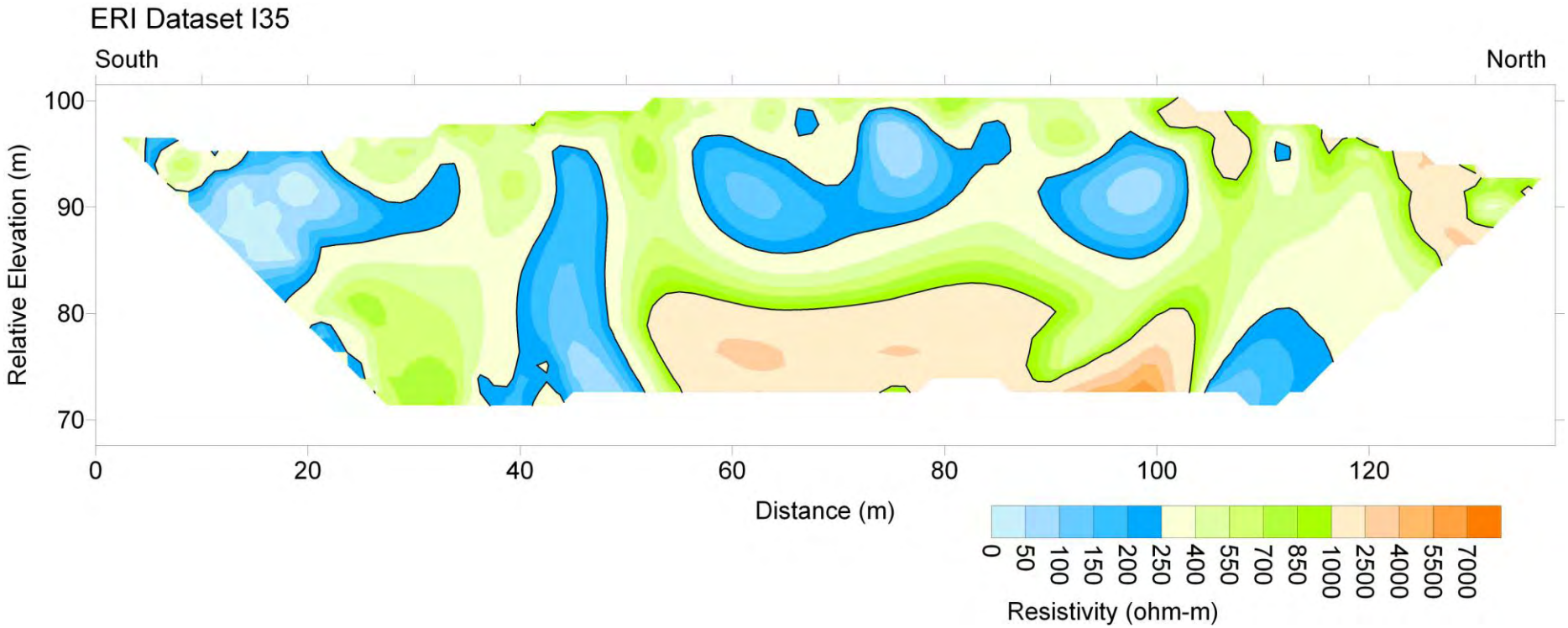

Figure A2.24. ERI Line I35.

SITE: Spears Well Site

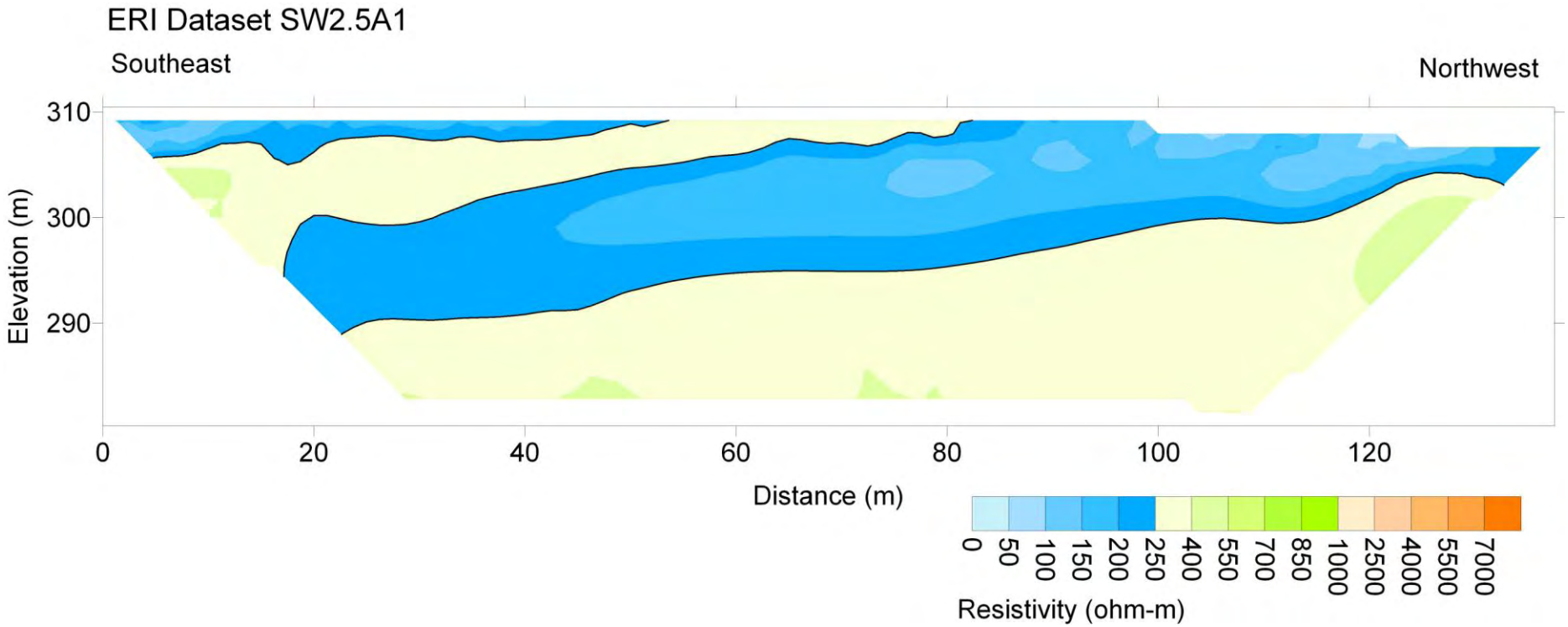

Figure A2.25. ERI Line SW2.5A1. This is the same location as files 38-41 (SW1* series).

SITE: Spears Well Site

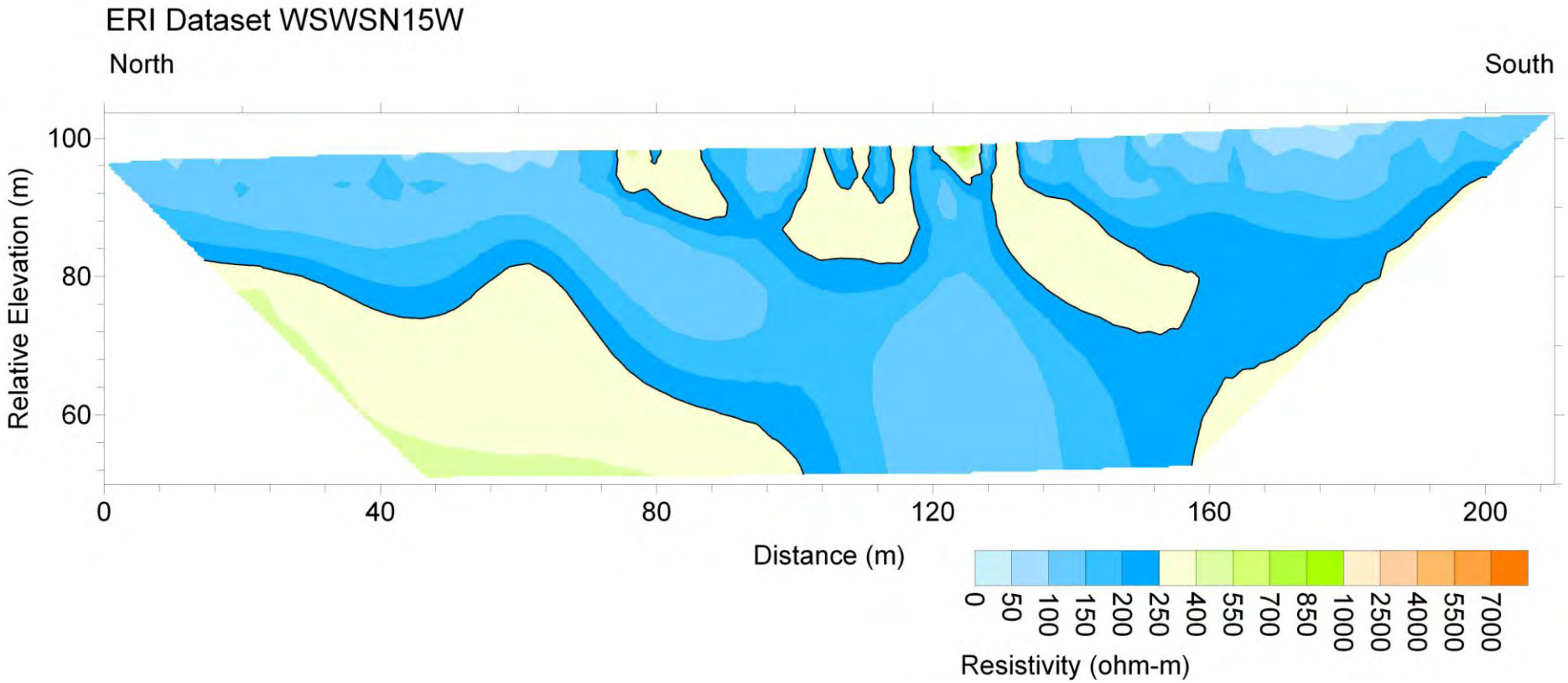

Figure A2.26. ERI Line WSWSN15W.

SITE: Spears Well Site

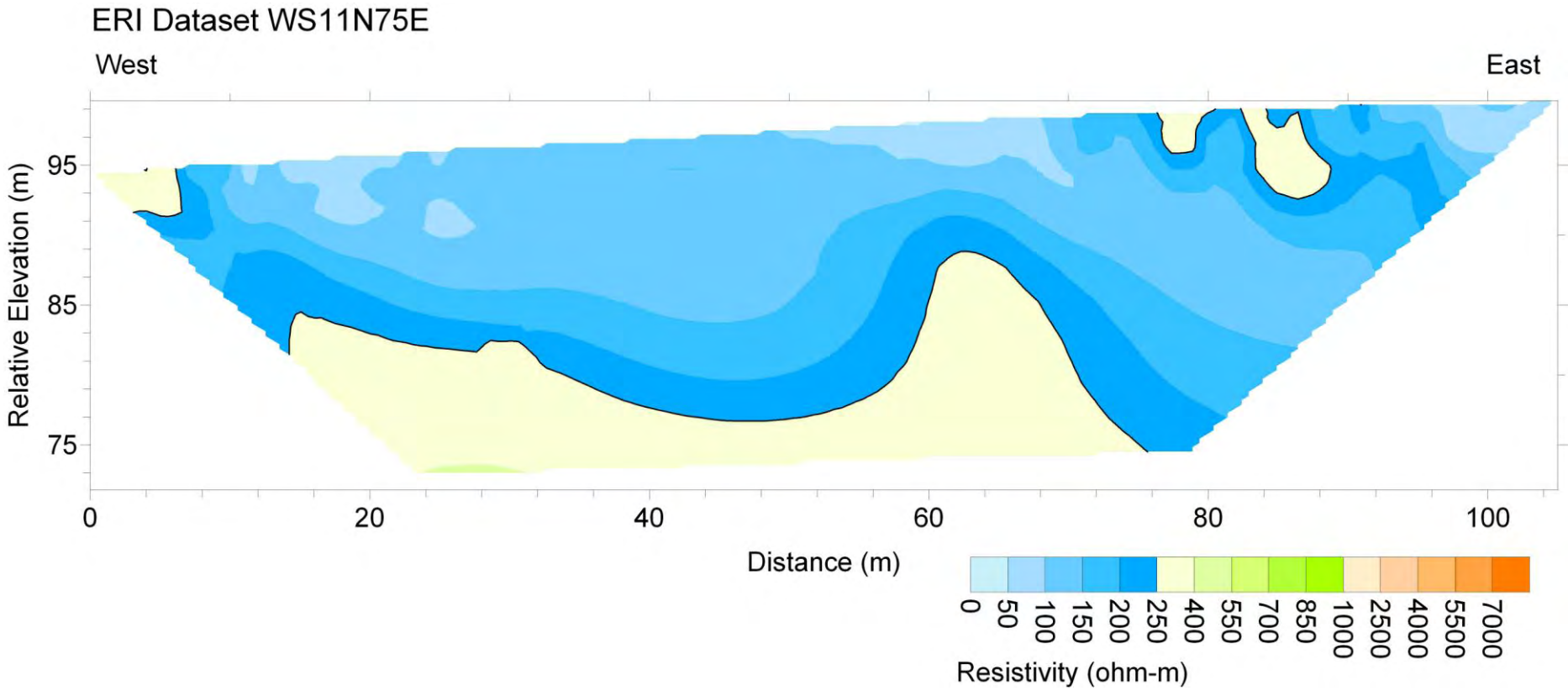

Figure A2.27. ERI Line WS11N75E.

SITE: Spears Well Site

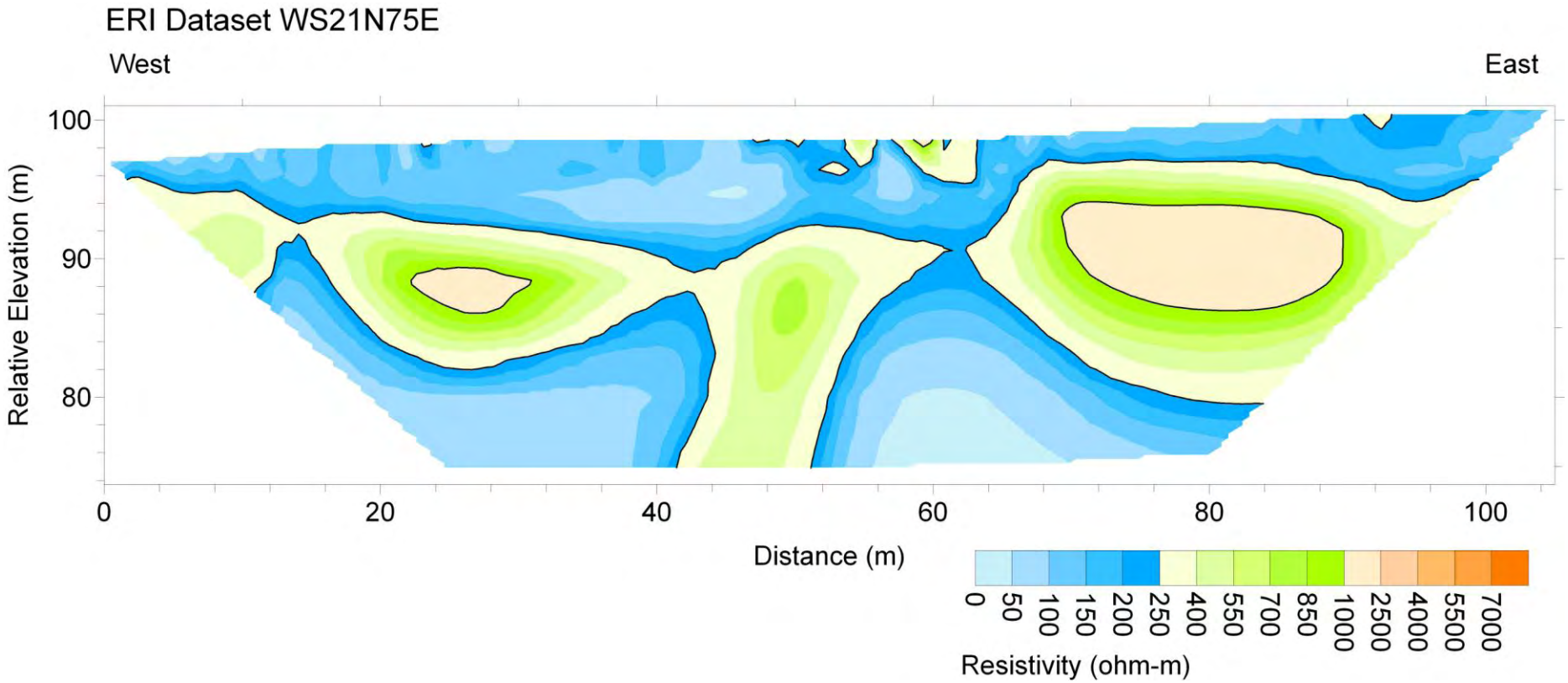

Figure A2.28. ERI Line WS21N75E.

SITE: Unimin Quarry

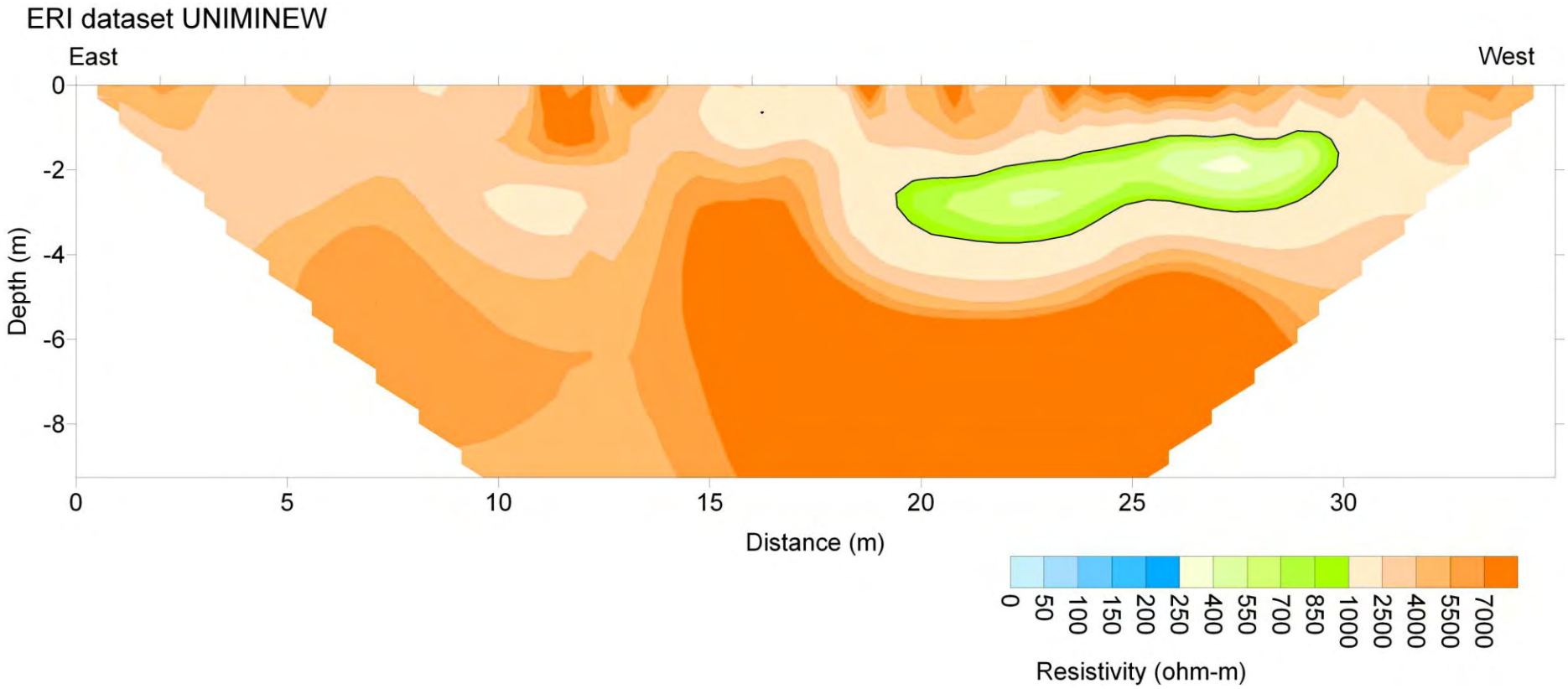

Figure A2.29. ERI Line UNIMINEW.

SITE: Unimin Quarry

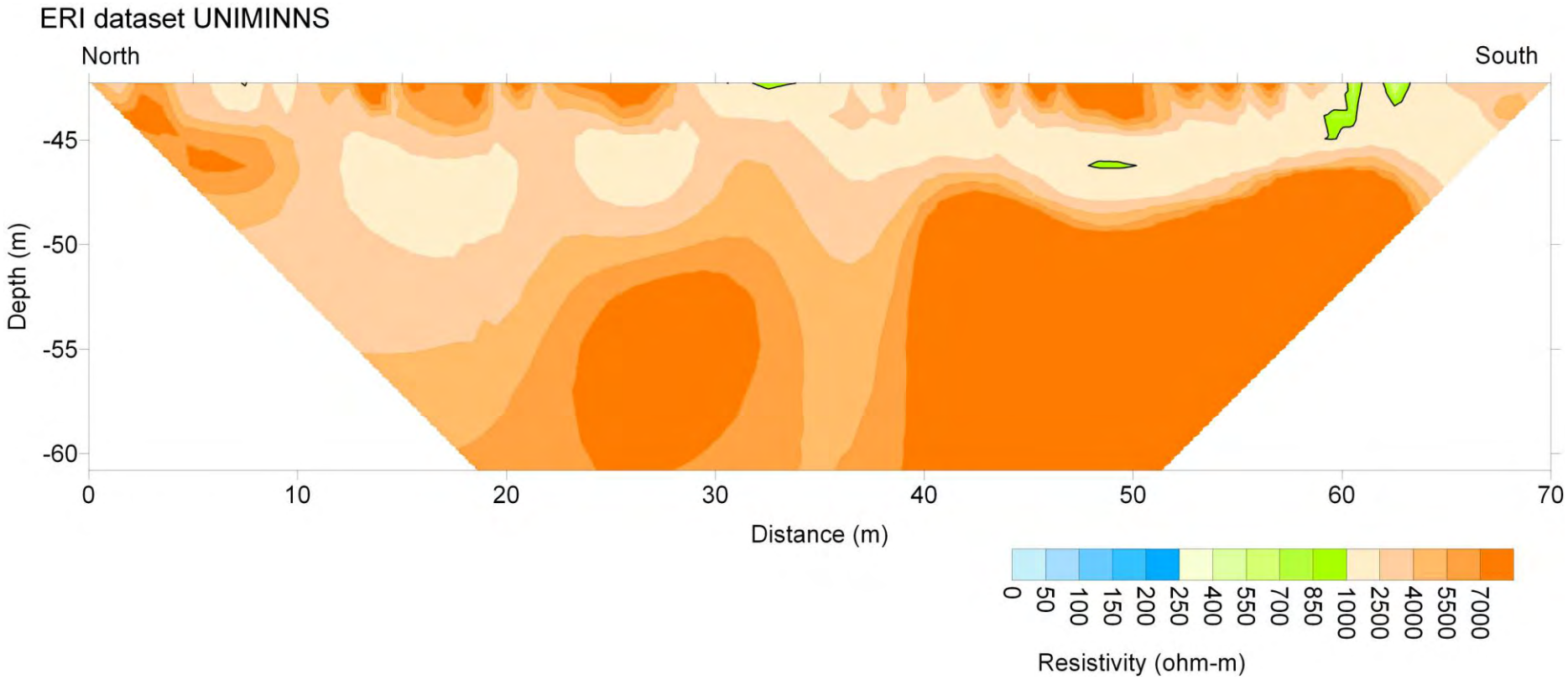

Figure A2.30. ERI Line UNIMINNS.

SITE: US Silica Quarry

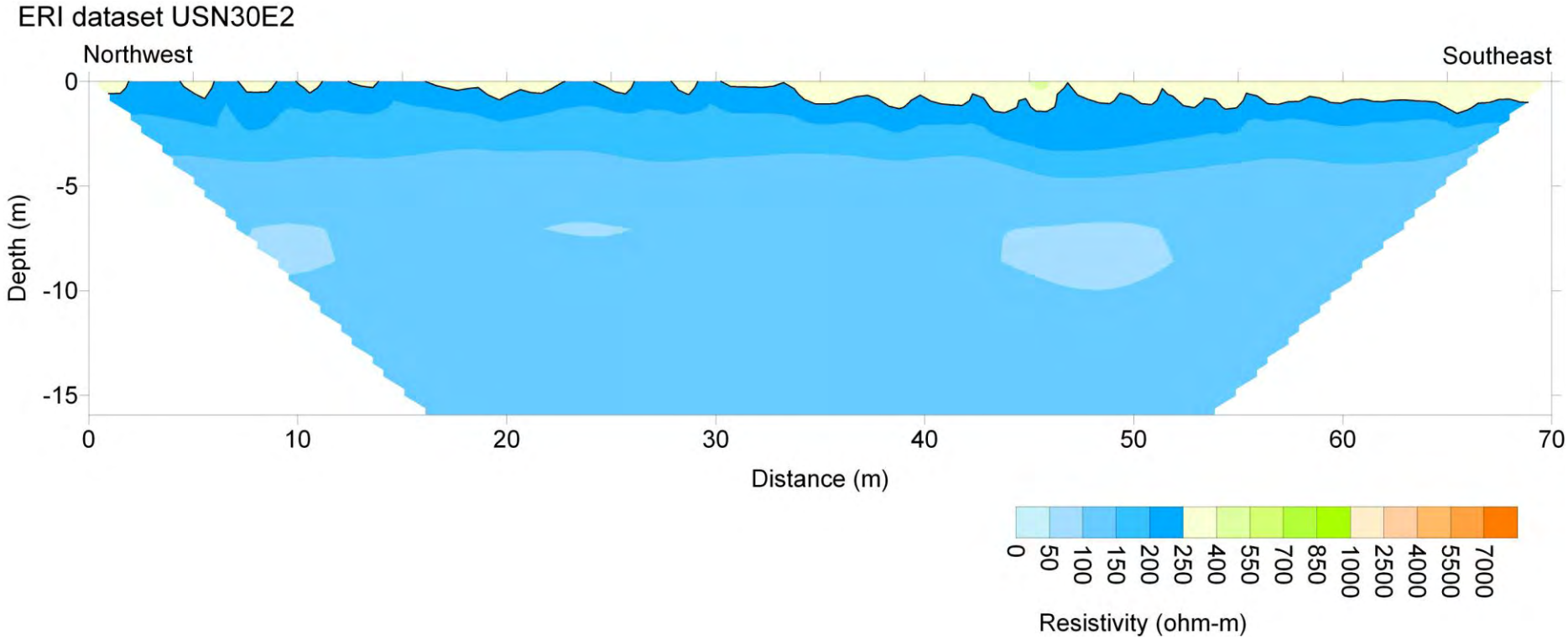

Figure A2.31. ERI Line USN30E2.

SITE: US Silica Quarry

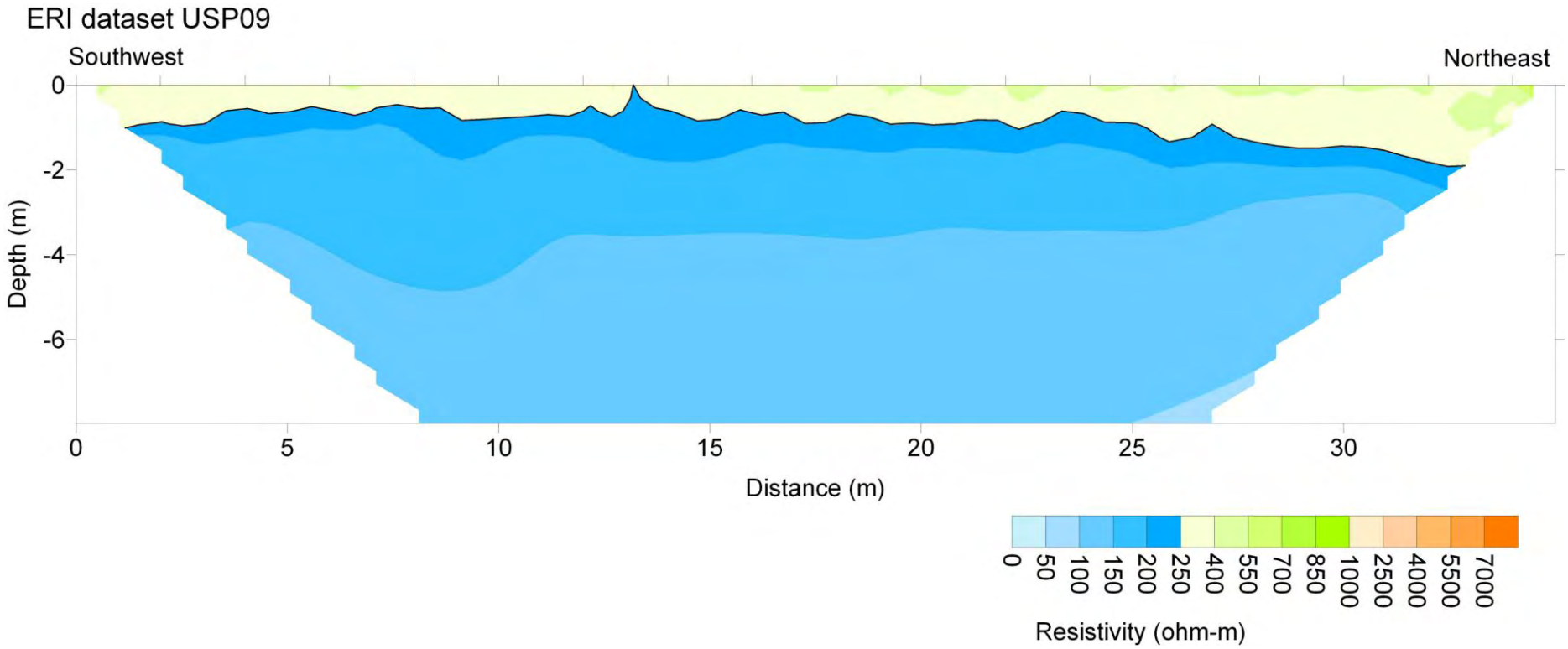

Figure A2.32. ERI Line USP09.

SITE: US Silica Quarry

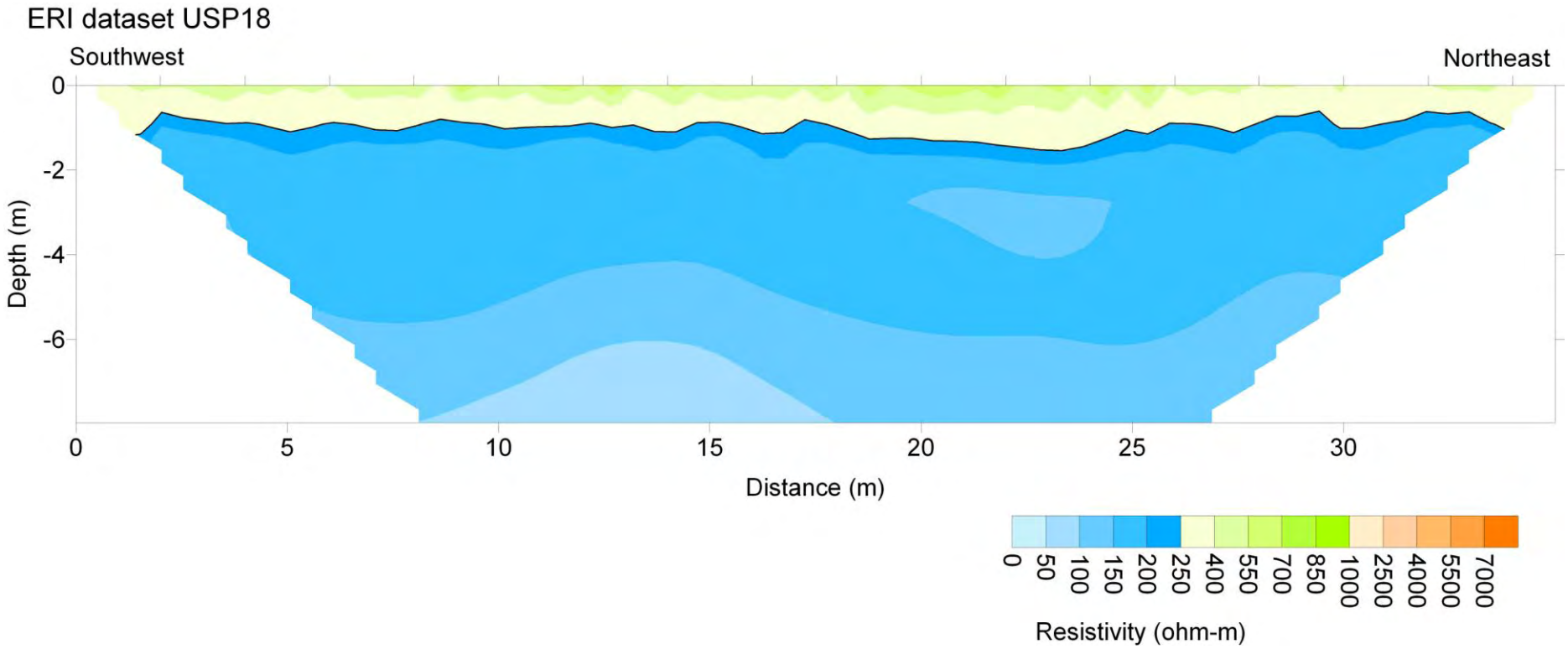

Figure A2.33. ERI Line USP18.

SITE: US Silica Quarry

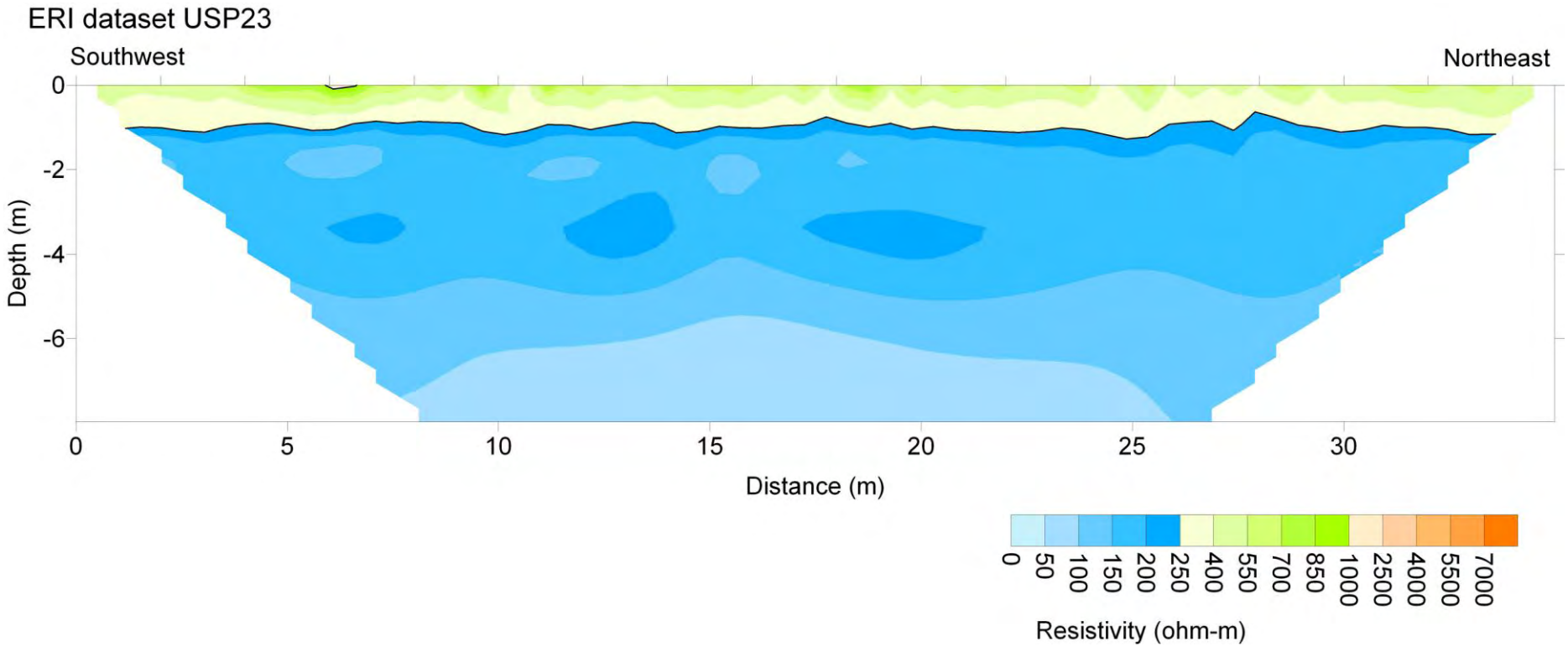

Figure A2.34. ERI Line USP23.

SITE: Vendome Well

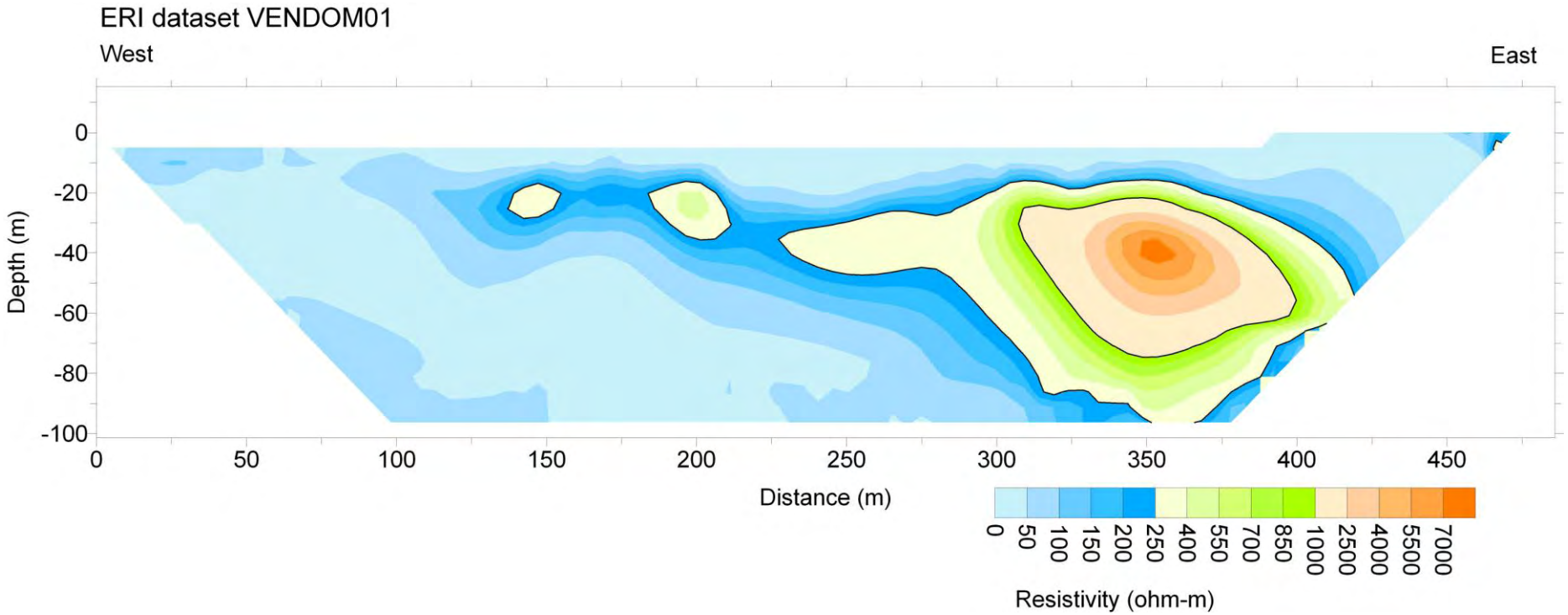

Figure A2.35. ERI Line VENDOM01.

SITE: Watson/Sulphur Fault

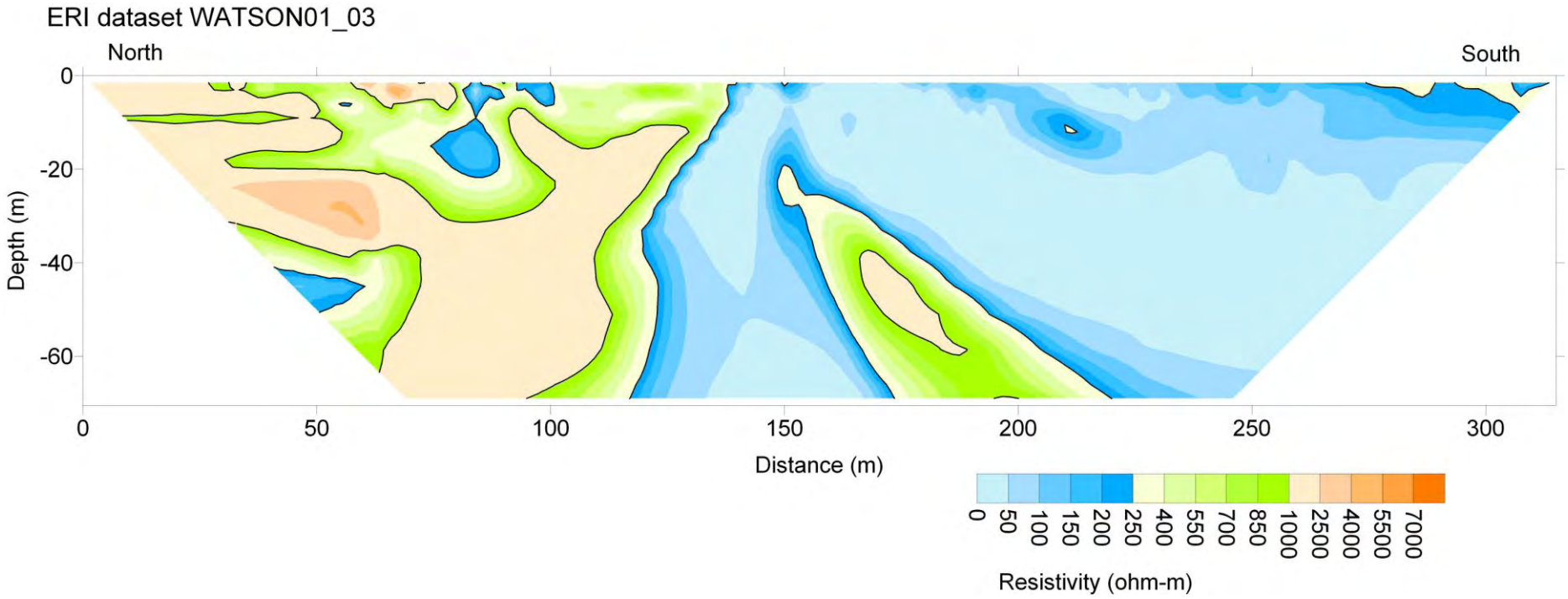

Figure A2.36. ERI Lines WATSON01-03.

SITE: Wingard 2 Well

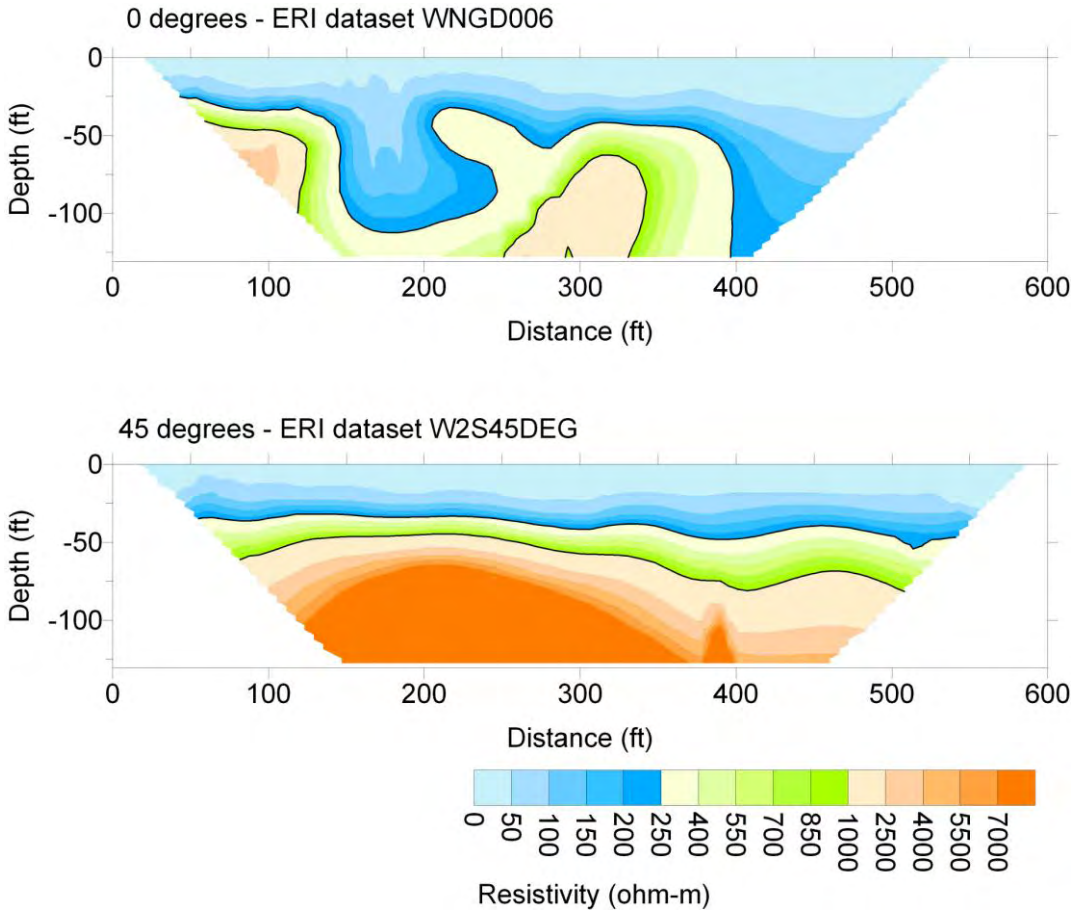

Figure A2.37. ERI Lines W2S45DEG and WNGD006.